Supporting Information for

Topochemical Synthesis of Single-Crystalline Hydrogen-bonded Crosslinked Organic Frameworks and Their Guest-induced Elastic Expansion

Xuanfeng Jiang,[†, ‡, ¶] Xunzhe Cui, [†, ‡] Andrew J. E. Duncan,[†, ‡] Liang Li,[†] Russell P. Hughes,[†] Richard J. Staples,[§] Eugeny V. Alexandrov,[#, ‖] Davide M. Proserpio,[#, ⊥] Yuyang Wu,[&] Chenfeng Ke[†, *]

[†] Department of Chemistry, Dartmouth College, 6128 Burke Laboratory, Hanover, New Hampshire, 03755

[¶] Key Laboratory of Green Preparation and Application for Functional Materials, Ministry of Education, School of Materials Science and Engineering, Hubei University, Wuhan 430062, P.R. China

[§] Department of Chemistry, 578 S. Shaw Lane, Michigan State University, East Lansing, MI 48824

[#] Samara Center for Theoretical Material Science (SCTMS), Samara State Technical University, Molodogvardeyskaya St. 244, Samara 443100, Russia

[‖] Samara Center for Theoretical Material Science (SCTMS), Samara University, Moskovskoe shosse 34, 443086 Samara, Russia

[⊥] Dipartimento di Chimica, Università degli studi di Milano, Via C. Golgi 19, 20133 Milano, Italy.

[&] IMSERC, Department of Chemistry, Northwestern University, 2145 Sheridan Road, Evanston, IL 60208

Email: Chenfeng.ke@dartmouth.edu

Table of Contents

S1. General Information

All reagents and solvents were purchased from commercial companies including Fisher Scientific, Sigma-Aldrich, and VWR and used without further purification. NMR spectra were recorded on either a Bruker AVIII 500 MHz spectrometer or a Bruker AVIII 600 MHz Spectrometer and referenced to residual solvent peaks. The working frequencies are 500 or 600 MHz for ^{1}H and 125 or 150 MHz for ^{13}C. Solid state ^{13}C-cross-polarization at magic-angle spinning (CPMAS) nuclear magnetic resonance measurements were performed on a Varian 400 MHz VNMRS system. Mass spectrometry was performed on Synapt G2-Si, Micromass Q-Tof Ultima mass spectrometers, and liquid chromatography–mass spectrometry (LC-MS) data were collected on a Shimadzu LCMS-8030 mass spectrometer. UV-Vis spectra monitoring experiments were carried out on a Shimadzu UV-1800 UV-Vis spectrometer. Raman measurements were carried out on a Horiba labRAM HR Evolution Raman spectrometer with a laser of 532 nm and a 1800 lines/mm grating. Each spectrum is measured within 10 s acquisition time and 6 accumulations. Elemental analysis was performed by Intertek Pharmaceutical Services (Whitehouse, NJ). Fourier transform infrared (FT-IR) spectra were collected on a Shimadzu IRAffinity-1 FTIR-8000 spectrometer. The sample was ground with IR-grade KBr and tableted as a transparent slice. Powder X-ray Diffraction (PXRD) data were collected on Bruker D8 ADVANCE and Rigaku MiniFlex powder X-ray diffractometers. Single crystal diffraction data were collected on a Bruker D8 Venture APEX II CCD single crystal diffractometer, at the Beijing Synchrotron Radiation Facility (BSRF, 3W1A beamline station), and at the Argonne Advanced Photon Source. Thermogravimetric analysis (TGA) was performed on a TGA Q50 V5.0 Build 164 thermal gravimetric analyzer with samples held in a platinum pan under a nitrogen atmosphere. Data was collected from room temperature to 600-800 °C with a ramp rate of 5 °C/min. Optical microscope white-light images were recorded by an AmScope SM-1TSW2 stereomicroscope. Scanning electron microscopy (SEM) images and energy-dispersive X-ray spectroscopy (EDS) data were acquired on an FEI Scios2 LoVac dual beam field emission gun environmental scanning electron microscope. Transmission electron microscopy (TEM) images were acquired on a Tecnai F20ST FEG-TEM (field emission gun transmission electron microscope) at an electron acceleration voltage of 200 kV. Samples were prepared by drop-casting a sonicated suspension on a Cu grid and air-dried. Supercritical CO_2 activation was performed by a Samdri 795 Critical Point Dryer. The crosslinked crystals were pretreated with ethanol and kept in microporous specimen capsules. Then the capsules were placed in the drying chamber and fulfilled by CO_2. The CO_2 input was maintained for an additional 10 min to purge the chamber. Next, the chamber was sealed, and the temperature was raised to 40 °C (above the CO_2 critical temperature) with inlet pressure of 1300 psi and held overnight to afford the activated crystal samples. Low-pressure gas sorption measurements were performed on a Micrometritics FLEX 3.0 surface area analyzer. Samples were degassed under dynamic vacuum for 12 h at 60 °C prior to each measurement. N_2 sorption isotherms were measured using a liquid nitrogen bath (77 K). CO_2 sorption isotherms were measured using an ice bath (273 K). The dynamic light scattering (DLS) data were acquired on a DynaPro NanoStar dynamic light scattering detector from Wyatt Technology.

S2. Synthesis of monomers, H_COFs and Polymers

Monomer 1. Freshly prepared octa-chloride derivative [1] **S1** (400 mg, 0.41 mmol) and diisopropylethylamine (DIPEA, 450 mg, 3.49 mmol, 8.5 *eq.* to **S1**) were dissolved in dioxane (anhydrous, 6 mL). The reaction turned into a cloudy brown-colored mixture after 10 min stirring at room temperature. Allylamine (467 mg, 8.20 mmol, 20.0 *eq.* to **S1**) was then added to the reaction mixture and stirred to afford a clear yellow solution. The reaction was then degassed, sealed under nitrogen atmosphere and heated to 110 °C with stirring overnight. After cooling to room temperature, water (100 mL) was added to the reaction and bright yellow precipitation was collected by filtration and washed with an excess of water (100 mL) and methanol (20 mL). The desired product was dried under reduced pressure as a yellow powder (405 mg, 0.35 mmol) in 82 % yield.

^{1}H NMR (500 MHz, DMSO-d_6, 373 K): δ = 8.38 (s, 4H), 7.54 (d, J = 8.8 Hz, 8H), 6.87 (d, J = 8.7 Hz, 8H), 6.48 (t, 8H), 5.94-5.86 (m, 8H) 5.17-5.02 (m, 4H + 4H), 3.90 (t, 8H). ^{13}C NMR (150 MHz, DMSO-d_6, 298 K): δ = 166.17-165.98, 164.40, 139.21, 138.72, 137.39, 136.73, 131.38, 118.80, 115.06, 42.89. HR-ESI-MS: calcd for $[M + H]^+$ m/z = 1149.6137, found m/z = 1149.6116.

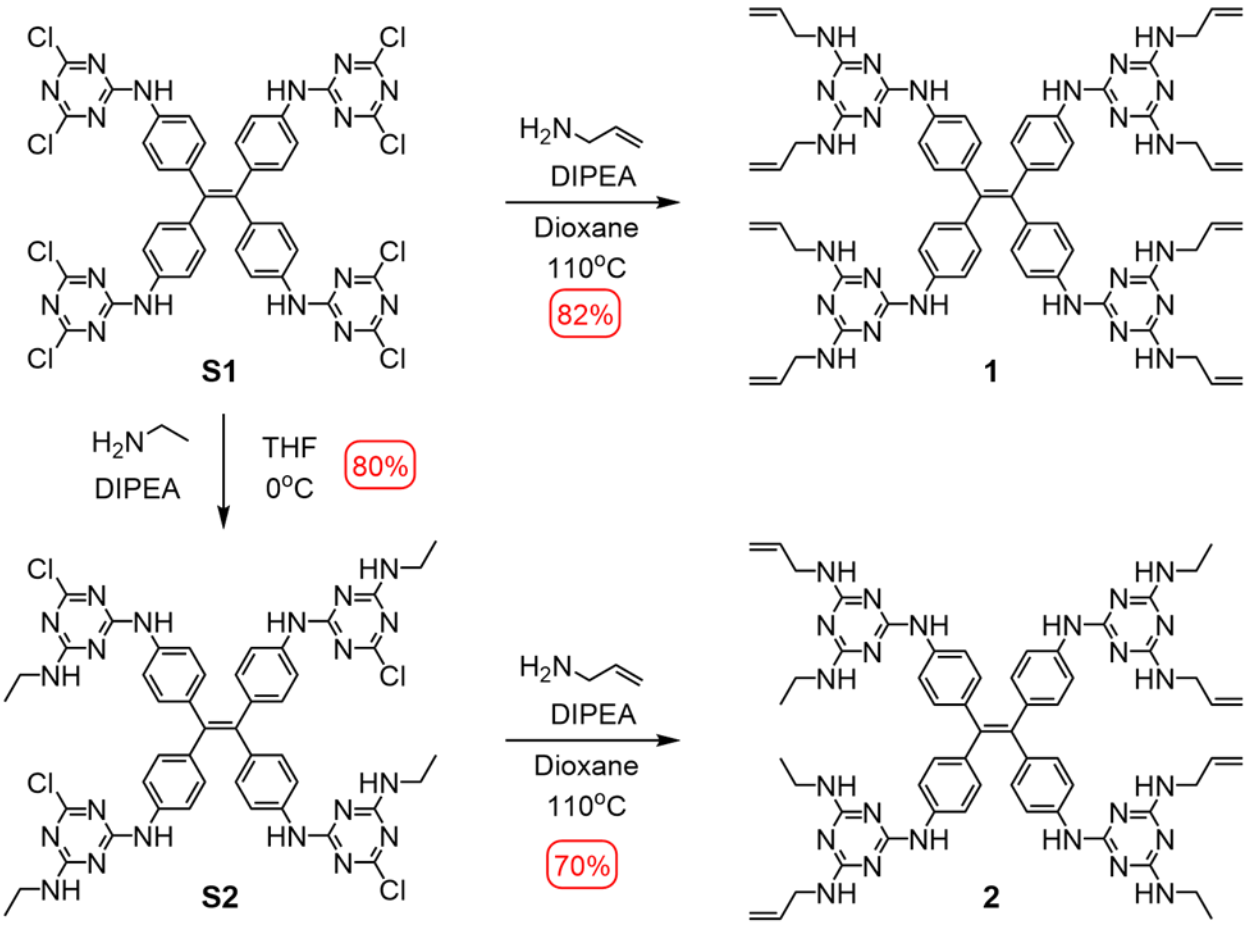

Scheme S1. Synthesis of monomers **1** and **2**.

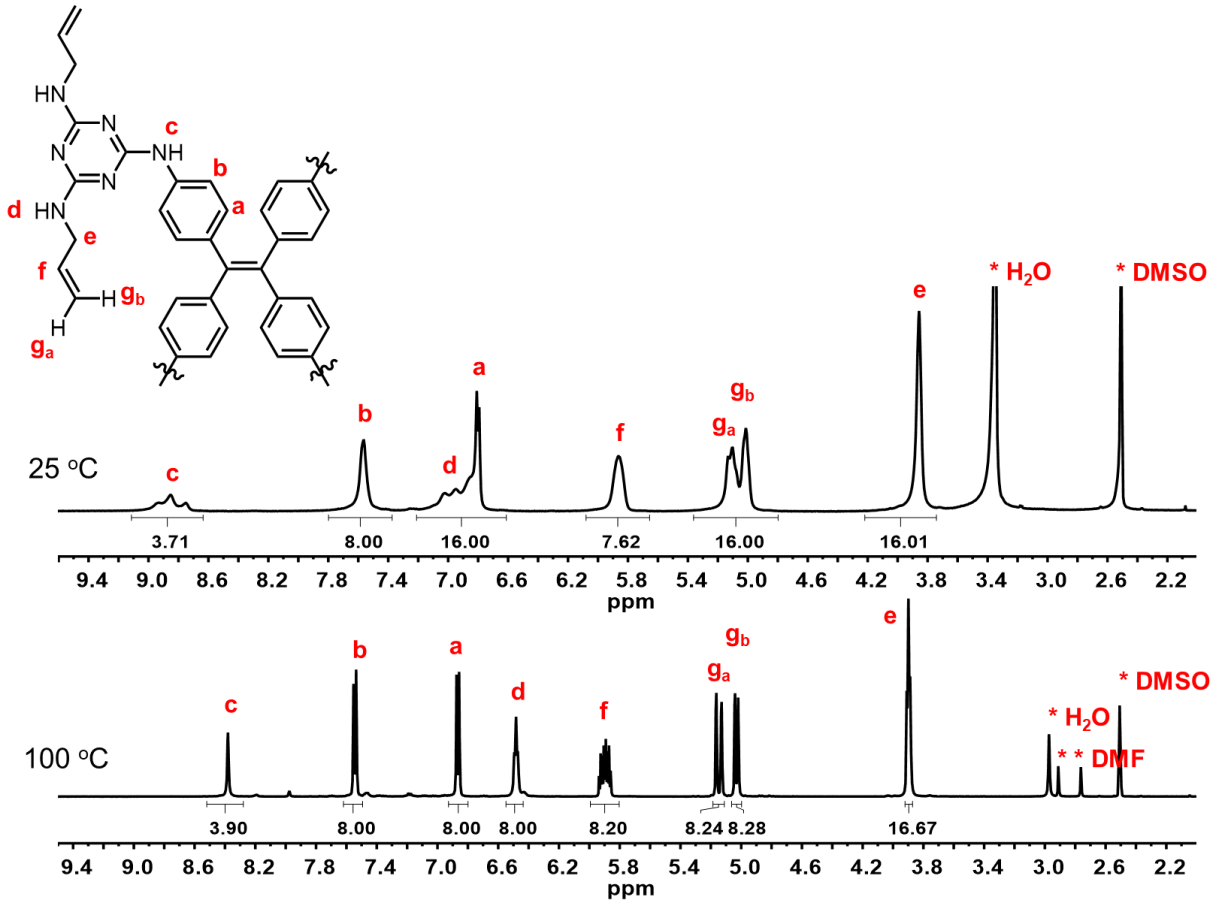

Figure S1. ^{1}H NMR spectra of **1** in DMSO-d_6 (500 MHz) recorded at (a) 298 K, and (b) 373 K

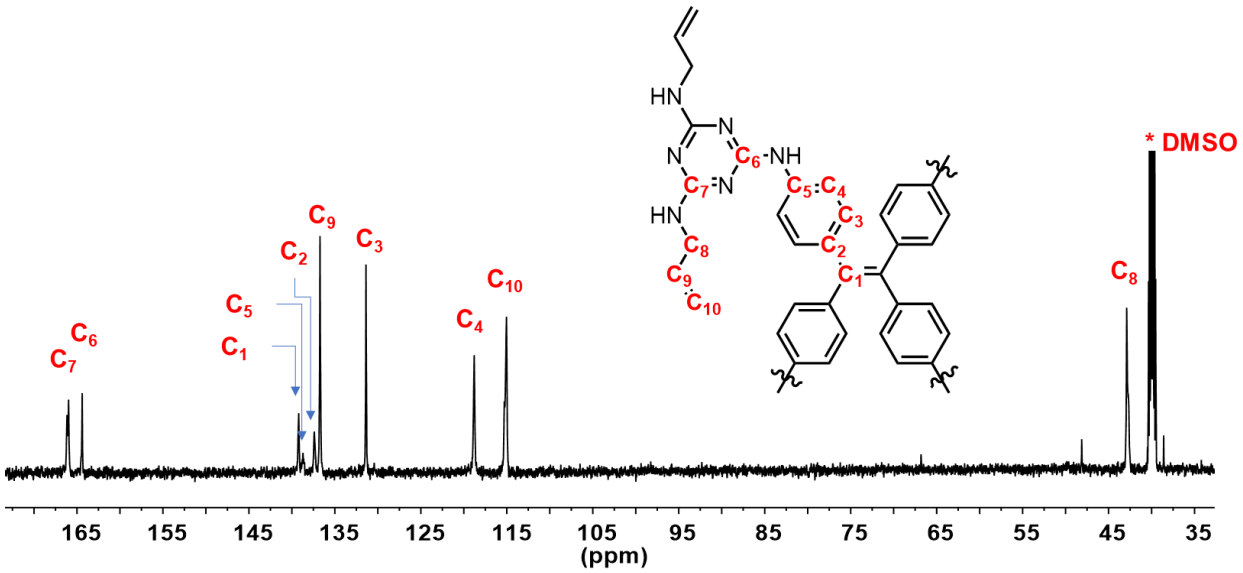

Figure S2. ^{13}C NMR spectrum of **1** in DMSO-d_6 (150 MHz) recorded at 298 K

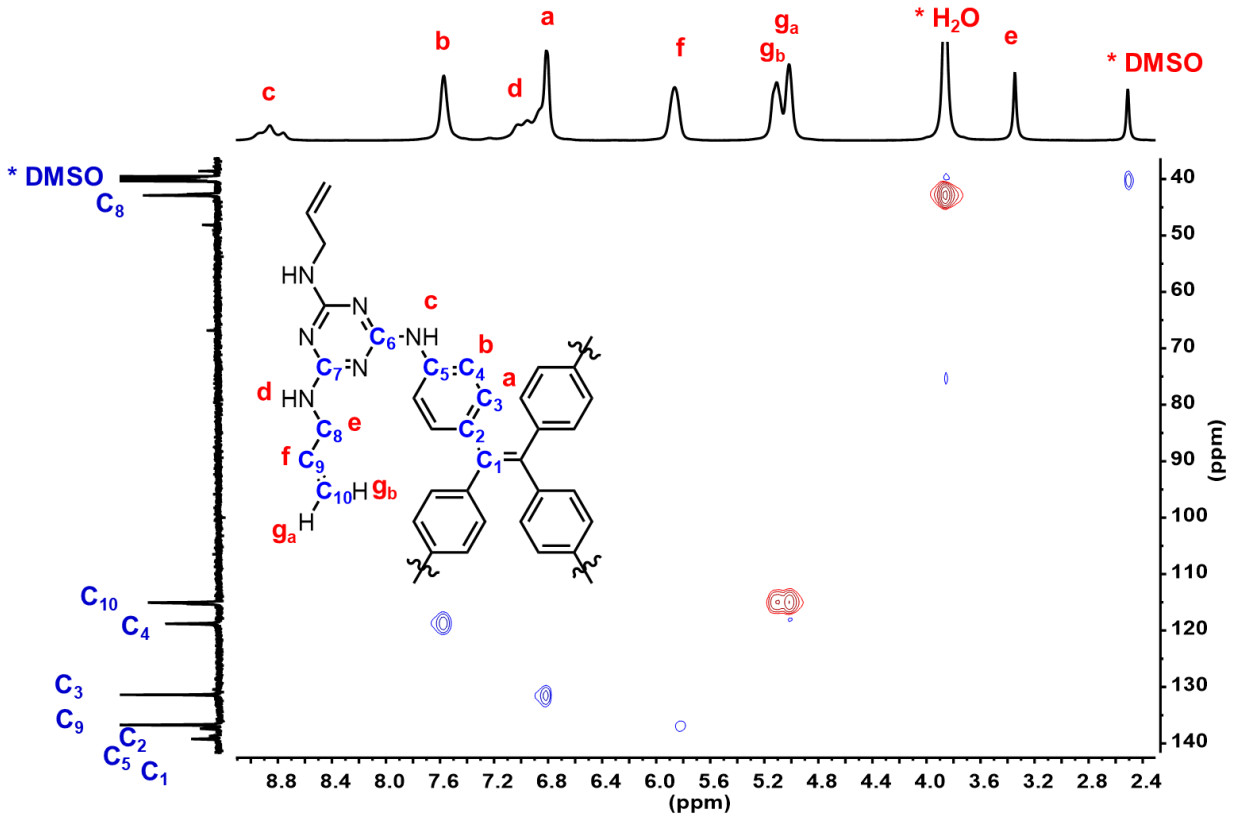

Figure S3. ^{1}H-^{13}C HSQC NMR spectrum (500 MHz, DMSO-d_6) of **1** recorded at 298 K

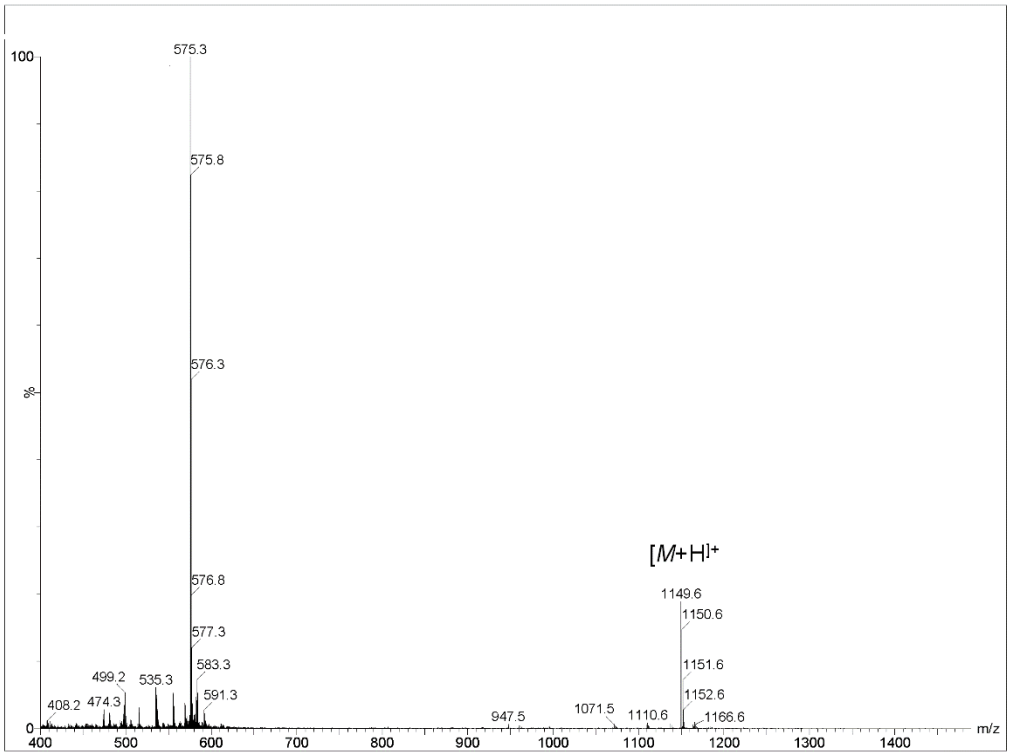

Figure S4. ESI-MS spectrum of **1**

Synthesis of S2. A 2 *M* ethylamine in THF solution (1.0 mL, 2 mmol), DIPEA (1.6 mmol, 314 mg, 0.7 mL), and THF (40 mL) were added to a 250 mL round bottom flask and the reaction was cooled in an ice bath. **S1** (400 mg, 0.5 mmol) was added in small portions over 10 min to the reaction with stirring. The reaction mixture was warmed to room temperature and stirred overnight. Insoluble residues were removed by filtration and the filtrate was condensed under reduced pressure at room temperature. The obtained yellow powder was washed with an excess of CH_2Cl_2, affording a yellow powder (330 mg, 0.34 mmol) in 80% yield. *Caution: the product is not stable upon heating in open-air, it is recommended to be stored under a nitrogen atmosphere at -20 °C.* ^{1}H NMR (500 MHz, DMSO-d_6, 298 K): δ = 10.07-9.92 (m, 4H), 8.15-8.07 (m, 4H), 7.61-7.55 (m, 8H), 6.89 (m, 8H), 3.25 (m, 8H), 1.08 (m, 12H). ^{13}C NMR (150 MHz, DMSO-d_6, 298 K): δ = 168.82, 165.59, 163.98, 139.42, 138.42, 137.70, 131.62, 119.65, 35.61, 14.95. This compound was used directly in the next synthetic step without further purification.

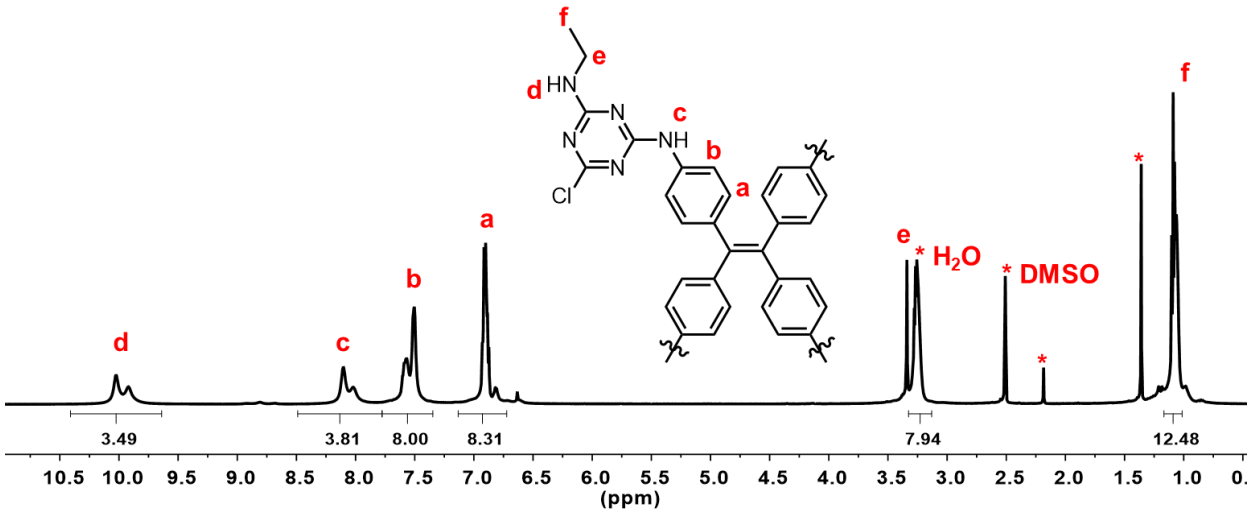

Figure S5. ^{1}H NMR spectrum (500 MHz, DMSO-d_6) of **S2** recorded at 298 K

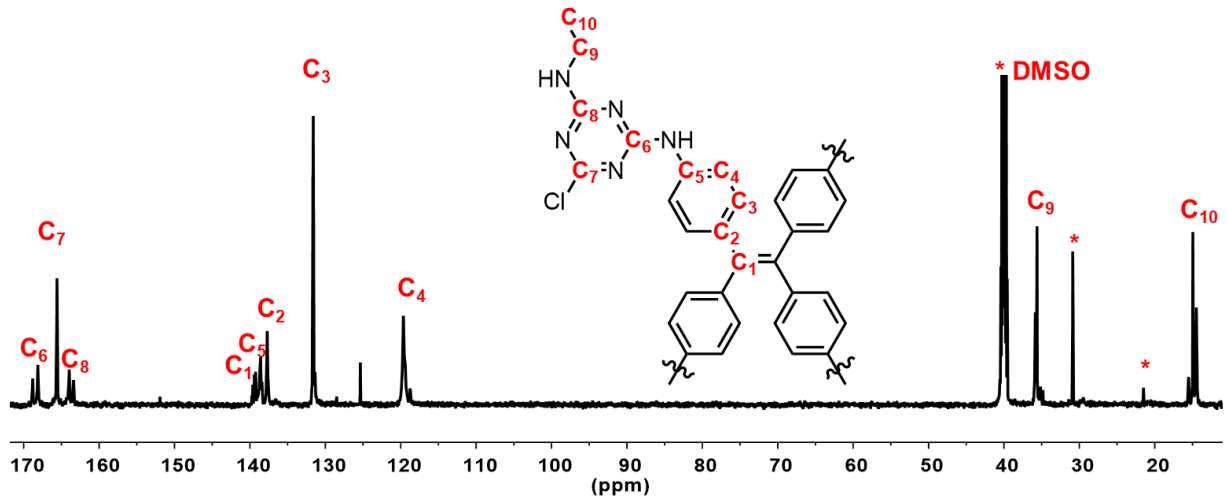

Figure S6. ^{13}C NMR spectrum (150 MHz, DMSO-d_6) of **S2** recorded at 298 K

Monomer 2. Tetrachloride derivative **S2** (300 mg, 0.29 mmol), allylamine (140 mg, 2.45 mmol, 0.2 mL), and DIPEA (160 mg, 1.12 mmol, 0.3 mL) were dissolved in dioxane (anhydrous, 8 mL). The reaction was degassed, sealed under a nitrogen atmosphere, and heated to 110 °C with stirring overnight. After cooling to room temperature, water (30 mL) was added to the reaction and the generated precipitate was collected by filtration and washed with an excess of water to afford the desired product as yellow powder (250 mg, 0.23 mmol) in 70 % yield.

^{1}H NMR (500 MHz, DMSO-d_6, 373 K): δ = 8.34 (s, 4H), 7.55 (d, J = 8.3 Hz, 8H), 6.87 (d, J = 8.5 Hz, 8H), 6.43 (t, J = 5.8 Hz, 4H), 6.31 (t, J = 5.7 Hz, 4H), 5.94-5.86 (m, 4H), 5.17-5.02 (m, 4H + 4H), 3.90 (m, 8H), 3.32 – 3.27 (m, 8H), 1.11 (t, J = 7.1 Hz, 12H). ^{13}C NMR (150 MHz, DMSO-d_6, 298 K): δ = 166.02, 165.86, 164.42, 139.31, 138.63, 137.34, 136.81, 131.39, 118.75, 114.99, 42.88, 35.18, 15.49. HR-ESI-MS: calcd for $[M + H]^+$ m/z = 1101.6137, found m/z = 1101.6129.

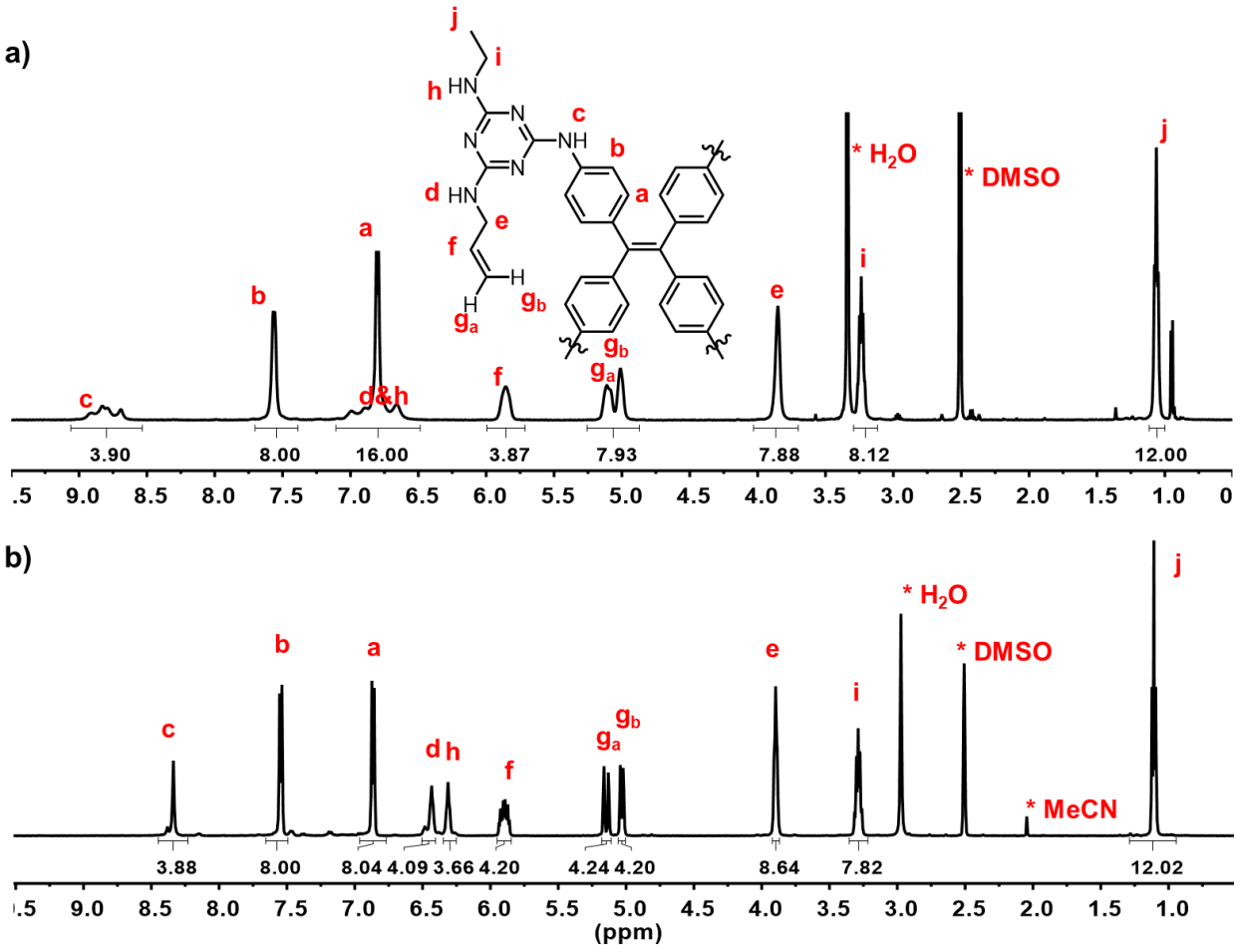

Figure S7. ^{1}H NMR spectra (500 MHz, DMSO-d_6) of **2** recorded at (a) 298 K, and (b) 373 K

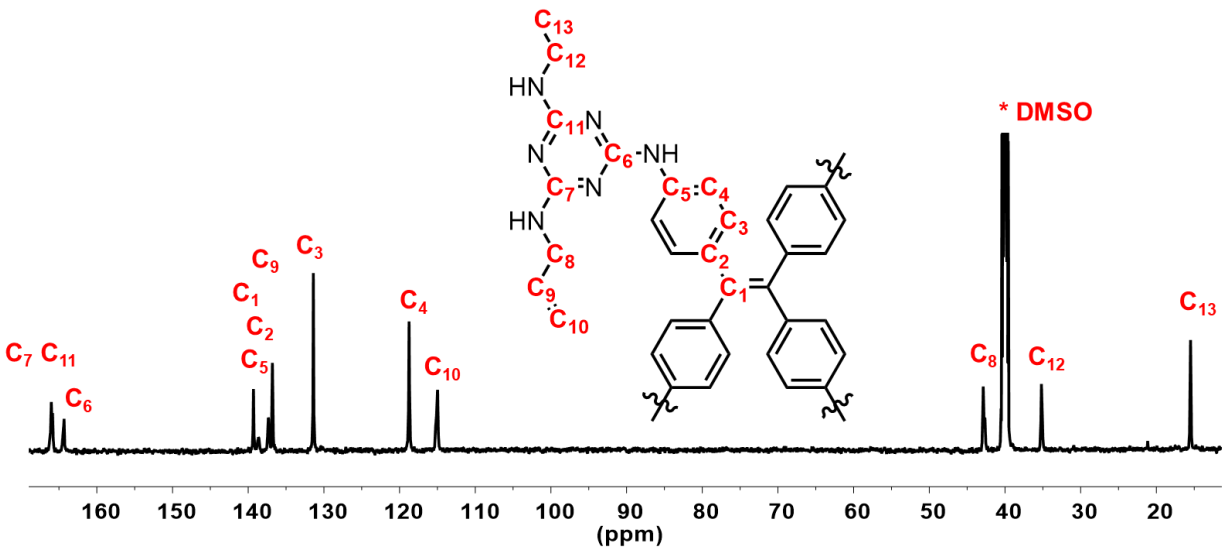

Figure S8. ^{13}C NMR spectrum (150 MHz, DMSO-d_6) of **2** recorded at 298 K

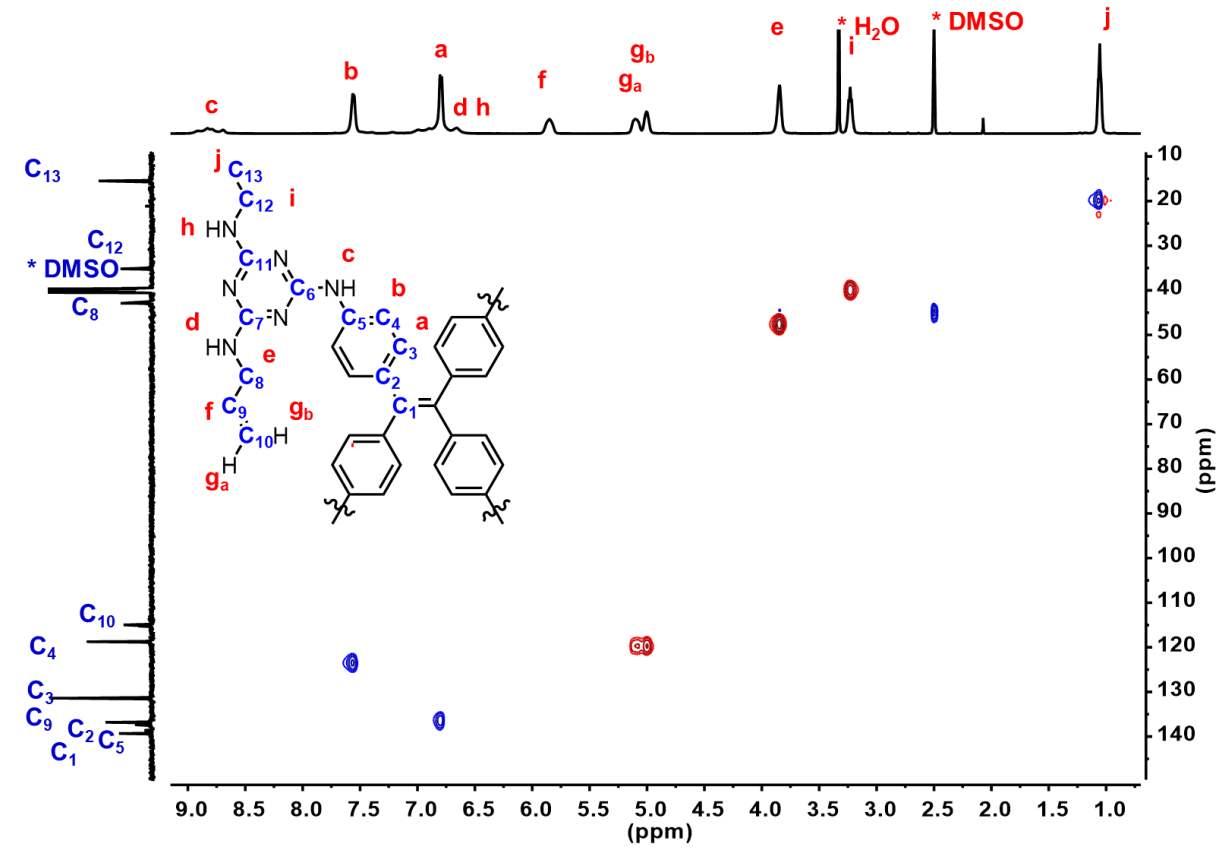

Figure S9. ^{1}H-^{13}C HSQC NMR spectrum (500 MHz, DMSO-d_6) of **2** recorded at 298 K

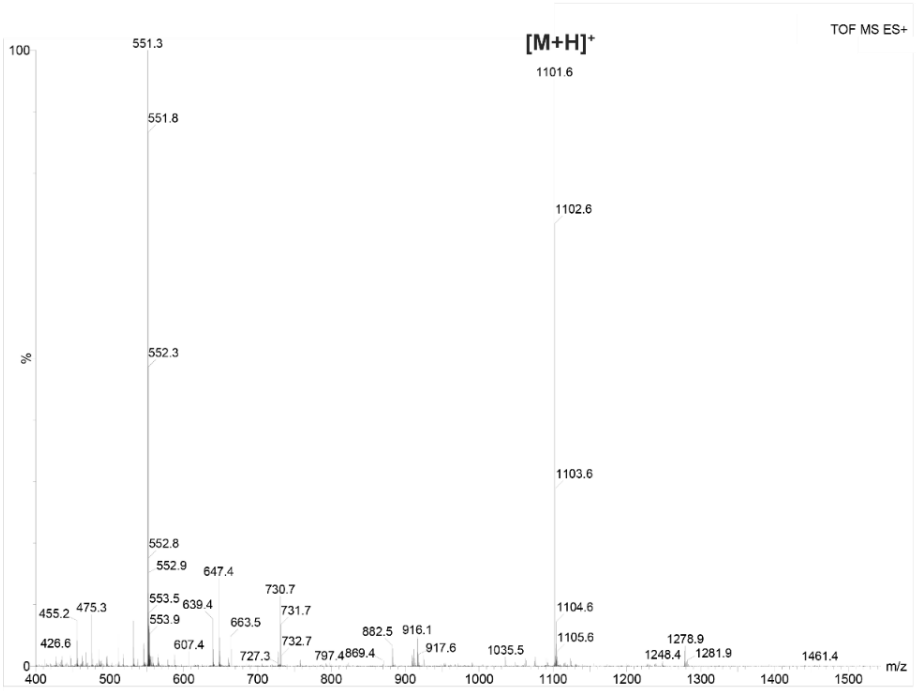

Figure S10. ESI-MS spectrum of **2**

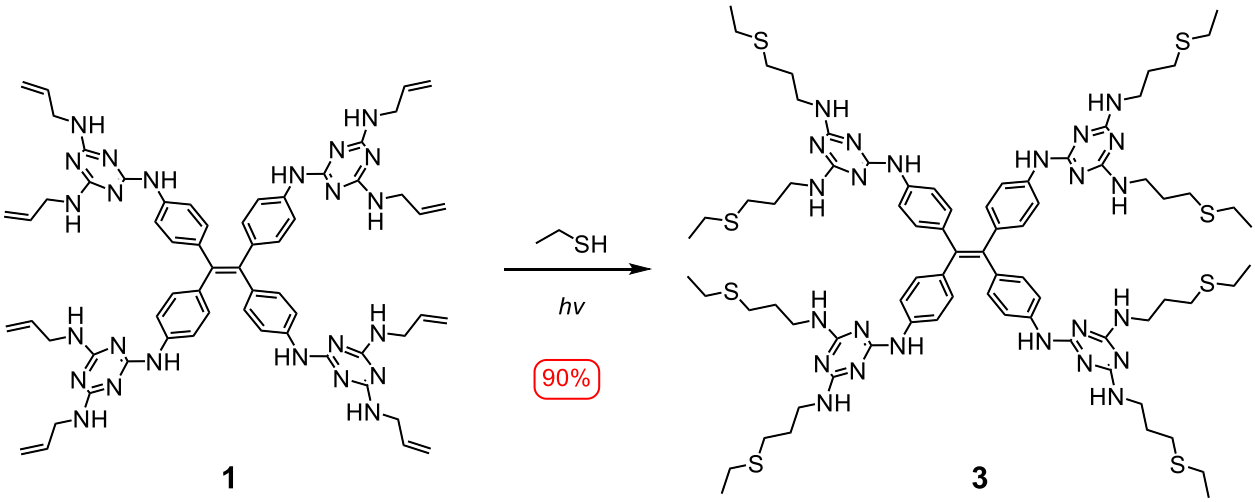

3. Monomer **1** (200 mg, 0.22 mmol), photo-initiator 2,2-dimethoxy-2,2'-phenylacetophenone (26 mg, 0.1 mmol) and ethanethiol (ET, 1 mL, 13.9 mmol) were dissolved in DMSO (anhydrous, 1 mL). The reaction was degassed, sealed under a nitrogen atmosphere and stirred for 3 d under UV irradiation (medium-pressure 175-watt Hg lamp). The orange-colored reaction turned into light yellow color gradually. The residual ethanethiol and DMSO were removed under reduced pressure to afford a yellow oil. This crude product was re-dissolved in CH_2Cl_2 (0.5 mL) and precipitated by ether (50 mL). The generated yellow precipitate was collected by filtration and washed with an excess of ether to afford the desired product as yellow powder. The solid product was purified by flash column chromatography (neutral Al_2O_3,

CH_2Cl_2/MeOH = 3:1 v/v), affording a bright yellow powder (240 mg, 0.15 mmol) in 90 % yield. ^{1}H NMR (500 MHz, DMSO-d_6, 298 K): δ = 8.83 (m, 4H), 7.57 (m, 8H), 7.02-6.82 (m, 8H + 8H), 3.29 (m, 16H, overlapped with H_2O peak), 2.43 (m, 32H, overlapped with DMSO solvent residual peak), 1.76 (m, 16H), 1.19 (m, 24H). ^{13}C NMR (150 MHz, DMSO-d_6, 298 K): δ = 165.55, 163.78, 138.82, 138.14, 136.86, 130.94, 118.26, 119.13, 39.40 (overlapped with DMSO solvent residual peak), 29.37, 28.28, 24.96, 14.70. HR-ESI-MS: calcd for $[M + H]^+$ *m/z* = 1645.7659, found *m/z* = 1645.7666; calcd for $[M + 2H]^{2+}$ *m/z* = 824.2265, found *m/z* = 824.3859.

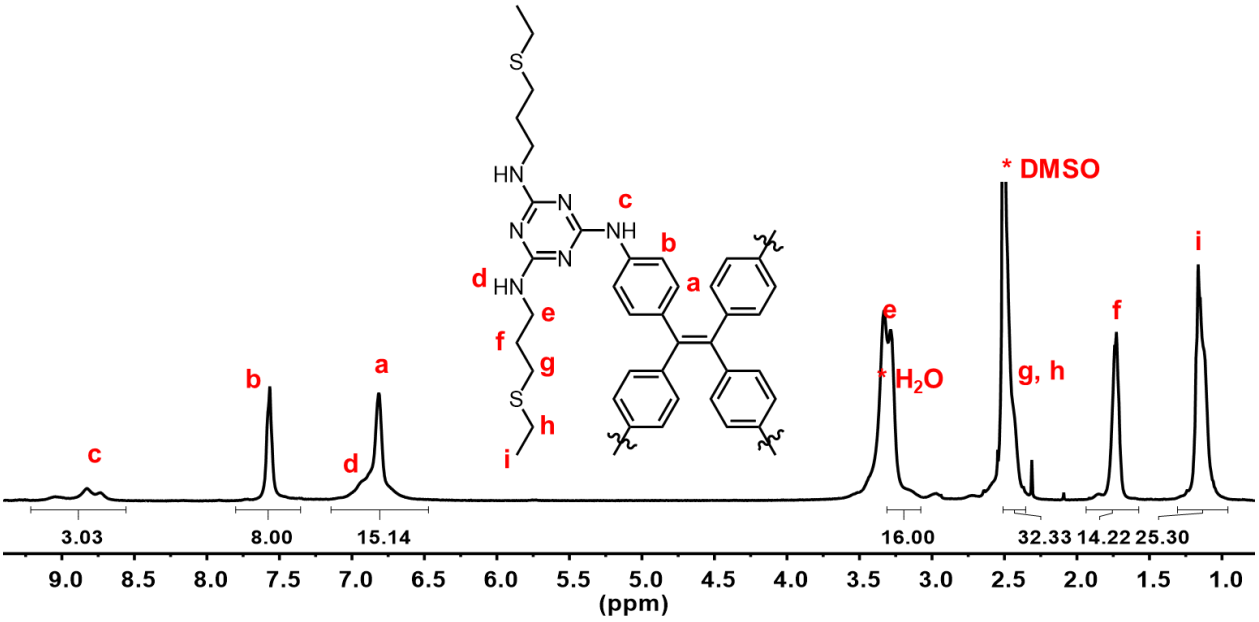

Figure S11. ^{1}H NMR spectrum (500 MHz, DMSO-d_6) of **3** recorded at 298 K

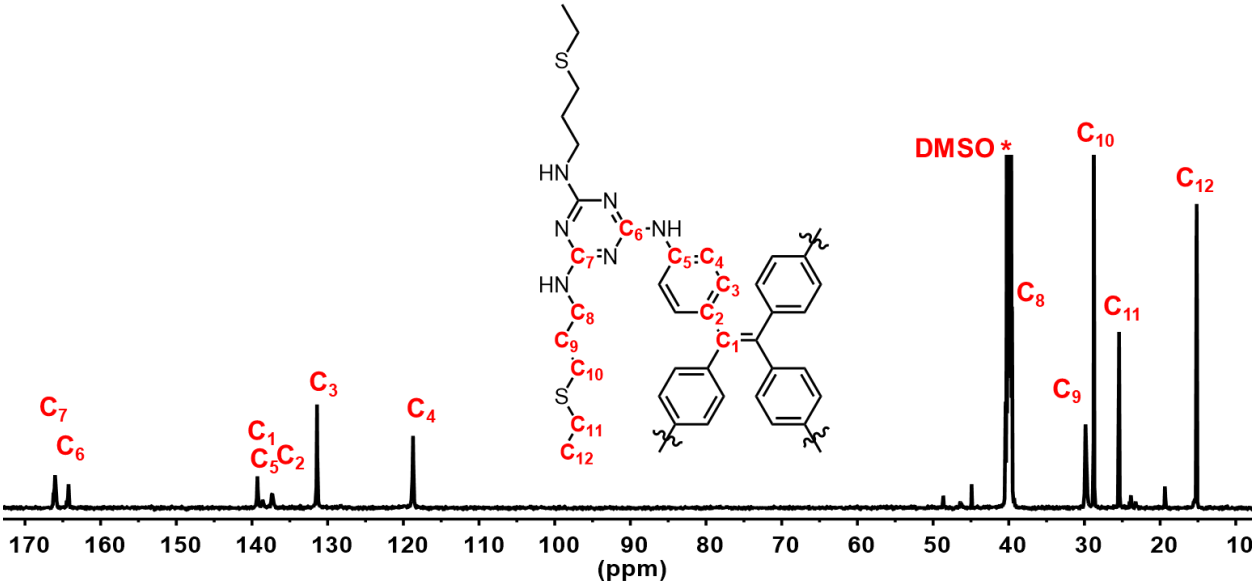

Figure S12. ^{13}C NMR spectrum (150 MHz, DMSO-d_6) of **3** recorded at 298 K

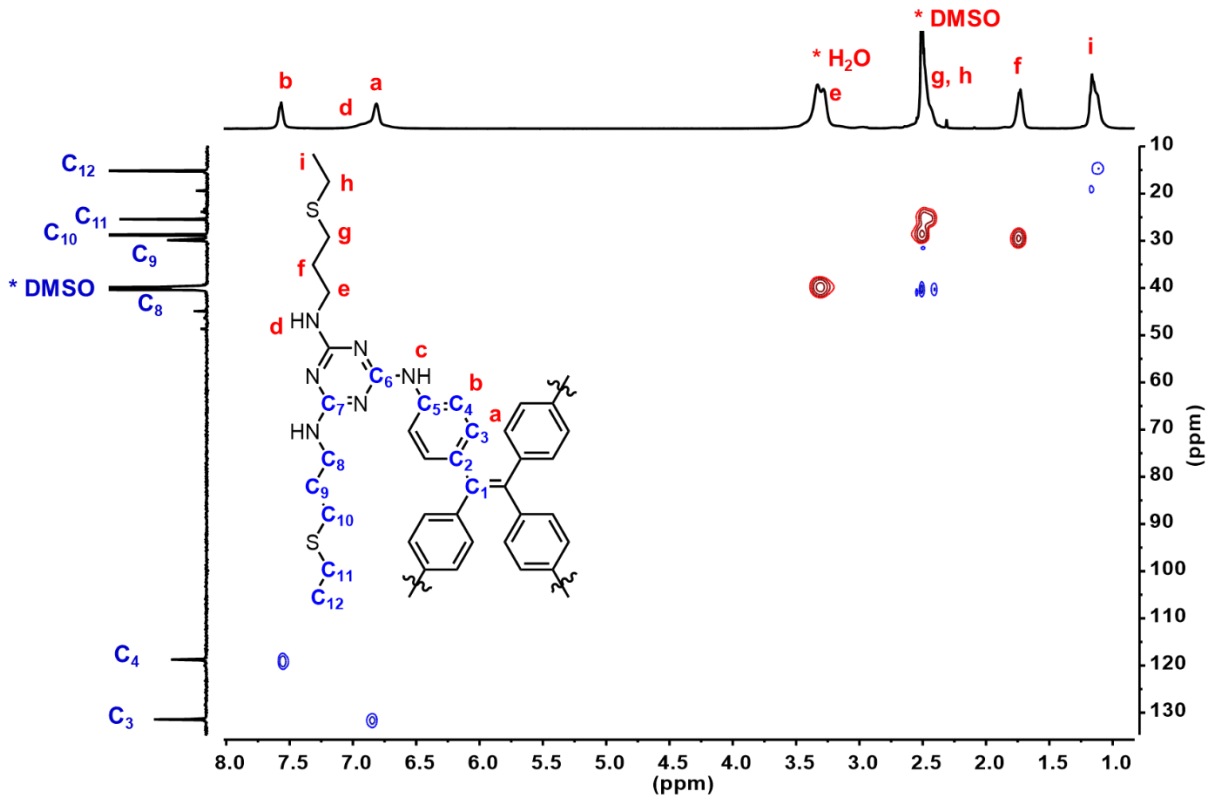

Figure S13. ^{1}H-^{13}C HSQC NMR spectrum (298 K, 500 MHz, DMSO-d_6) of **3**

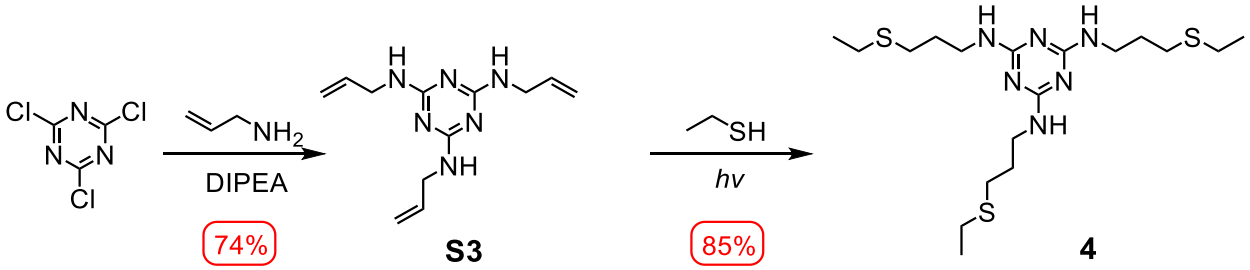

S3.[2] In a 48 mL heavy-wall pressure vessel, allylamine (1.8 g, 31.6 mmol) and DIPEA (2.1 g, 16.3 mmol) were dissolved in dioxane (10 mL) at 0 ºC. Cyanuric chloride (1.0 g, 5.43 mmol) was then added to the mixture in small portions. The reaction mixture was stirred at room temperature for 3 h in the sealed pressure vessel. The temperature was increased to 110 ºC and kept stirring for 12 h. After cooling to room temperature, the solvent was removed under reduced pressure and the residue was washed by ethanol/water (v/v = 1:1) to afford **S3** (1.0 g, 4.07 mmol, 74 %) as a white powder. ^{1}H NMR (500 MHz, DMSO-d_6, 298 K): δ = 6.68 (m, 3 H), 5.84 (m, 3 H), 5.22(m, 3H), 3.82 (t, J = 5.35 Hz, 6H). ^{13}C NMR (150 MHz, DMSO-d_6, 298 K): δ = 165.68, 136.54, 114.55, 42.39.

4. Compound **S3** (246 mg, 1 mmol), 2,2-dimethoxy-2,2'-phenylacetophenone (30 mg, 8.18 mmol) and ethanethiol (0.5 mL, 6.95 mmol) were dissolved in DMSO (anhydrous, 1 mL). The reaction was degassed, sealed under a nitrogen atmosphere, and stirred for 3 d under UV irradiation (medium-pressure 175-watt Hg lamp). The residual ethanethiol and DMSO were removed under reduced pressure to afford a yellow

oil. This crude product was dissolved in acetone (1 mL) before water (50 mL) was added. The generated yellow precipitate was collected by centrifugation, washed with an excess of water, and freeze-dried. The crude product was further purified by flash column chromatography (neutral Al_2O_3: CH_2Cl_2/MeOH = 4:1 v/v), affording a bright yellow oil (367 mg) in 85 % yield. ^{1}H NMR (500 MHz, DMSO-d_6, 298 K): δ = 6.52 (m, 4H), 3.27 (m, 6H), 2.29 (m, 12H), 1.73 (m, 6H), 1.17 (m, 9H). ^{13}C NMR (150 MHz, DMSO-d_6, 298 K): δ =166.13, 39.99, 29.87, 28.78, 25.40, 15.19. HR-ESI-MS: calcd for $[M + H]^+$ m/z = 433.2242, found m/z = 433.2237.

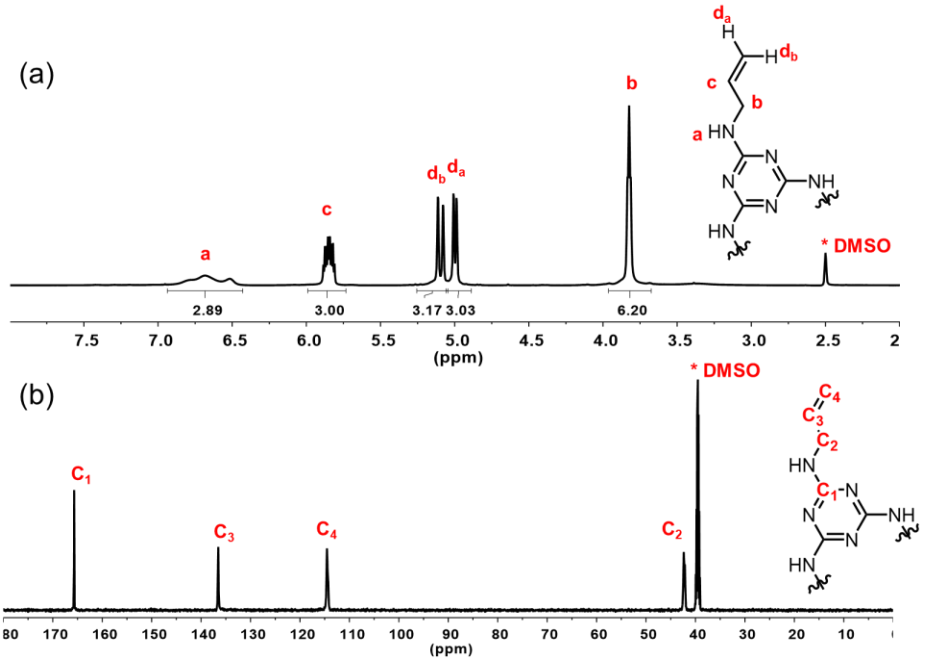

Figure S14. ^{1}H and ^{13}C NMR spectra (DMSO-d_6) of **S3** at 298 K

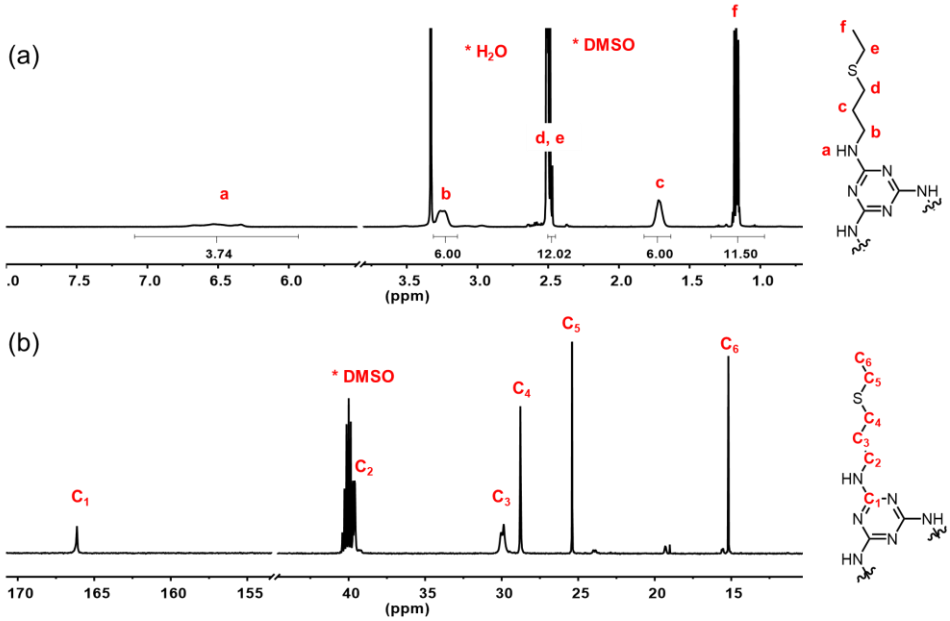

Figure S15. ^{1}H and ^{13}C NMR spectra (DMSO-d_6) of **4** at 298 K

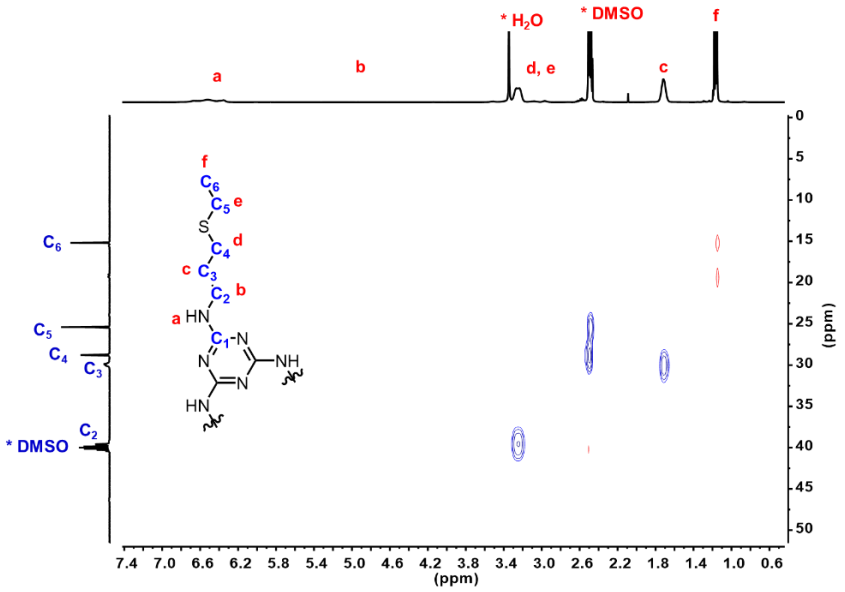

Figure S16. ^{1}H-^{13}C HSQC NMR spectrum (298 K, 500 MHz, DMSO-d_6) of **4**

S3. Single-crystal to single-crystal transformations

Crystallization of 1 and 2. High-quality crystal samples of **1** and **2** were prepared by allowing MeCN (8 mL) to slowly diffuse into a DMF solution (0.5 mL) of **1** or **2** (13 mg, 11.0 μmol) at room temperature for 2 weeks (yield ~80%).

General methods to synthesize single-crystalline H_COFs-2–4. *Method 1*. The mother solution of **1**$_{crystal}$ (~ 10 mg per vial) was removed carefully before MeCN (3 mL) was added to wash the surface of crystal samples. The resulted cloudy solution was removed. This process was repeated for another two times to clean the surface of the crystals. Then, neat alkyldithiol (~20 mmol, 2 mL) was added to the vial and the glass vial was kept in dark for 72 h to allow extensive diffusion of the crosslinker. The glass vial was irradiated under the UV light (medium-pressure 175-watt Hg lamp) for 72 h to allow photo-crosslinking. The unreacted alkyldithiol was decanted and further washed by an excess of EtOH. The crystal samples were collected and soaked in an excess of DMSO at 60 °C overnight to remove unreacted monomer **1**. After hot DMSO washing, MeOH was employed to perform solvent exchange at 60 °C for another 12 h. The crystal samples were vacuum dried and activated using supercritical CO_2. *We noticed that, during the crosslinker diffusion process, some crosslinkers already react with the alkene groups of the monomer, which led to a lower crosslinking degree compared with method 2*.

Method 2. The mother solution of **1**$_{crystal}$ was removed and MeCN (3 mL) was added to wash the surface of the crystals. The resulted cloudy solution was removed, and this washing process was repeated for another two times. Fresh MeCN (2 mL) was added to the crystal samples before alkyldithiol (~2 mmol, 200 μL) was added. The sample was kept in the dark for 24 h to allow an extensive dithiol diffusion into **1**$_{crystal}$. Another two portions of alkyldithiol (~2 mmol, 200 μL) were introduced subsequently after 24 and 48 h, respectively. The glass vial was irradiated under the UV light (medium-pressure 175-watt Hg lamp) for 72 h with forced air cooling. The crystal samples were collected and washed by an excess of MeCN to remove the unreacted alkyldithiol for single crystal X-ray analysis. These crystals were then soaked in fresh DMSO

at 50 °C overnight and this washing process is repeated three times. After DMSO washing, MeOH was employed to perform solvent exchange at 50 °C for another 12 h for three times. The crystal samples were vacuum dried and activated using supercritical CO_2.

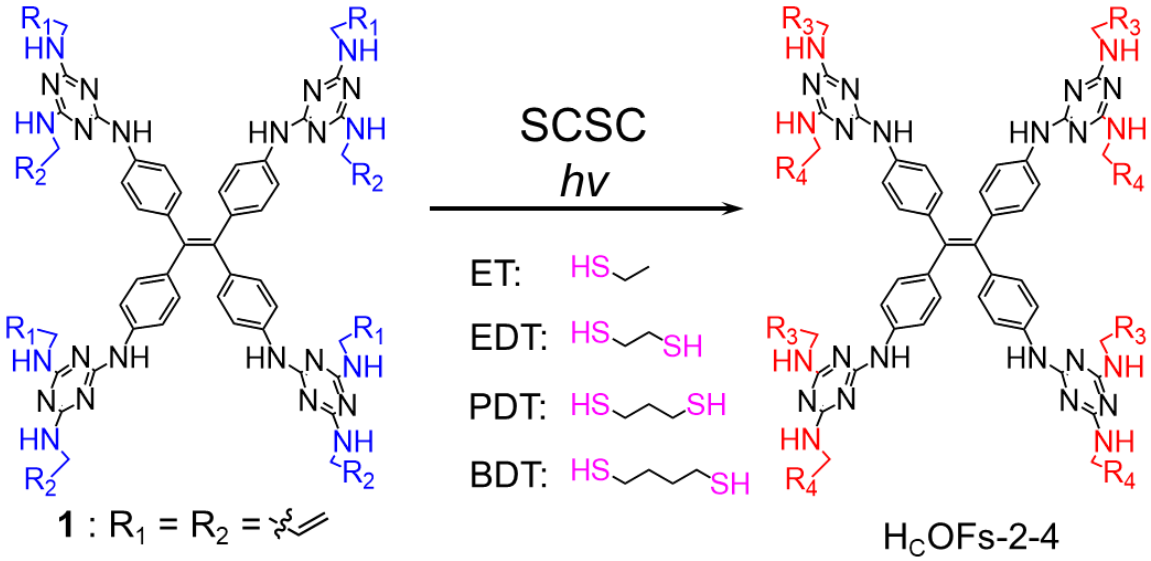

monomer	thiols	products	$R_3 = R_4$ =	allyl/thioether
1	ET	**1** + 6.7ET	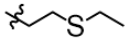	1.3 / 6.7
	EDT	H_COF-2	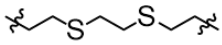	0 / 8.0
	PDT	H_COF-3	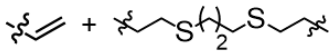	2.0 / 6.0
	BDT	H_COF-4	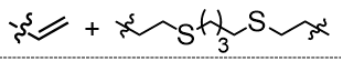	3.0 / 5.0

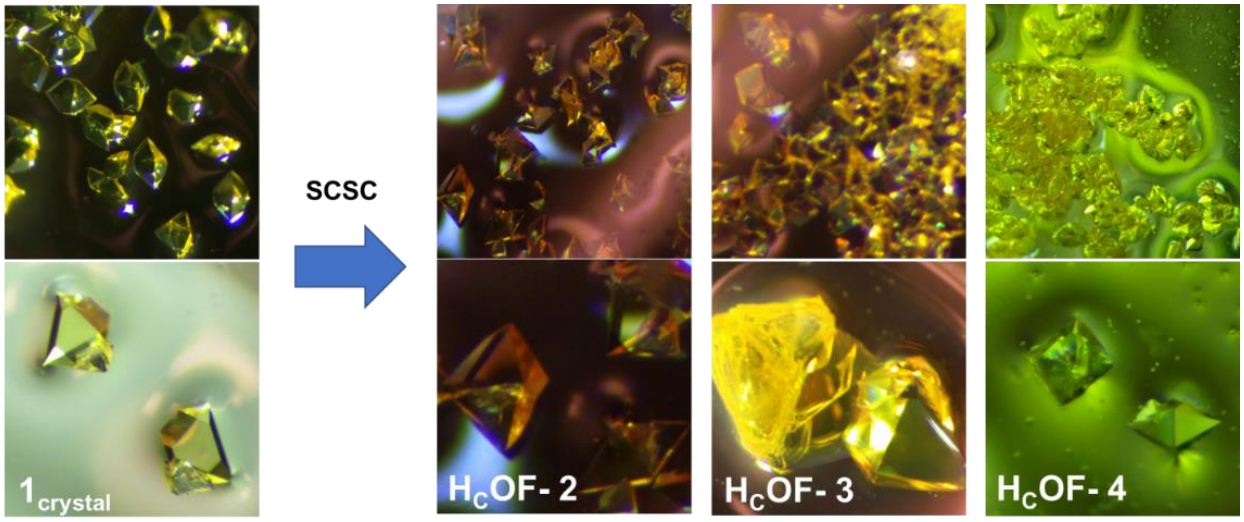

Figure S17. Single-crystal to single-crystal (SCSC) transformation of $\mathbf{1}_{crystal}$ to H_COFs-2–4 via photo-irradiated thiol-ene reaction, and images (*from left to right*) of $\mathbf{1}_{crystal}$, H_COF-2, H_COF-3, and H_COF-4 recorded on an optical microscope. Ethanethiol and alkyldithiols with different chain lengths (n = 1–3) were employed in the SCSC transformation.

H_COF-2: ^{13}C CPMAS NMR (100 MHz, 298K, 10,000 rpm): δ = 166.4, 164.5, 138.3, 132.3, 122.3, 113.4, 40.6, 31.1. Elemental analysis: [**1**]·$[C_2H_6S_2]_{4.10}$·$[CO_2]_{1.75,}$ calc.: C 53.59 %, H 5.79 %, N 20.85 %, S 16.30 %; found: C 53.50 %, H 5.72 %, N 20.92 %, S 16.26 %.

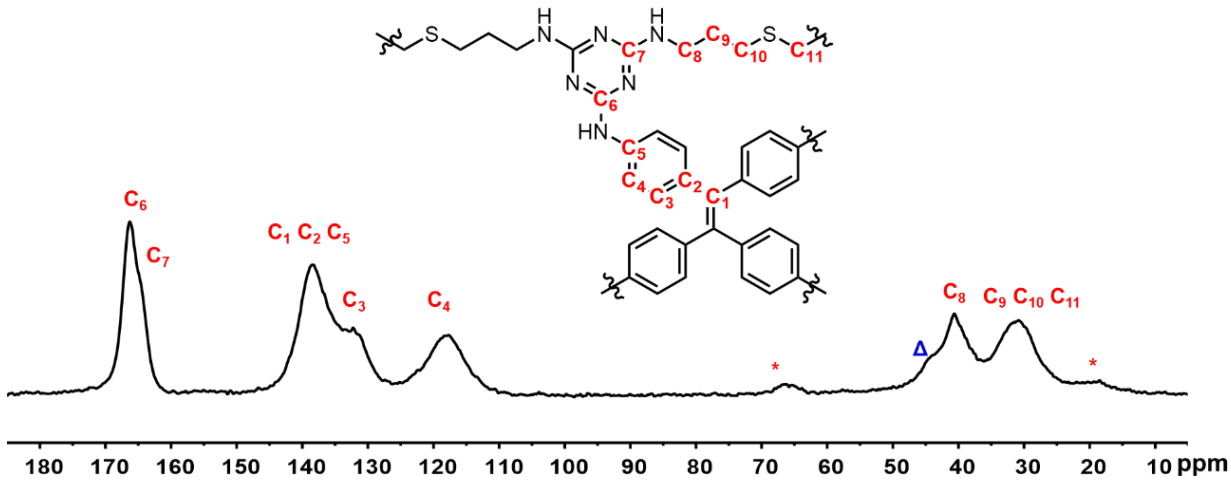

Figure S18. ^{13}C CPMAS NMR (100 MHz, 298K, 10000 rpm) spectrum of H_COF-2 (spinning sidebands are noted as *). Trace amount of unreacted allyl carbon was noticed (Δ) in the obtained H_COF-2 ([**1**]·$[C_2H_6S_2]_{3.85}$·$[CO_2]_{1.2}$) sample.

H_COF-3: ^{13}C CPMAS NMR (100 MHz, 298K, 10,000 rpm): δ = 166.1, 164.1, 140.3, 138.3, 135.6, 131.1, 121.3, 116.84, 41.5, 30.7. Elemental analysis: [**1**]·$[C_3H_8S_2]_{2.95}$·$[CO_2]_{1.40,}$ calc.: C 56.71 %, H 6.03 %, N 21.97 %, S 12.36 %; found: C 56.64 %, H 6.03 %, N 22.01 %, S 12.43 %.

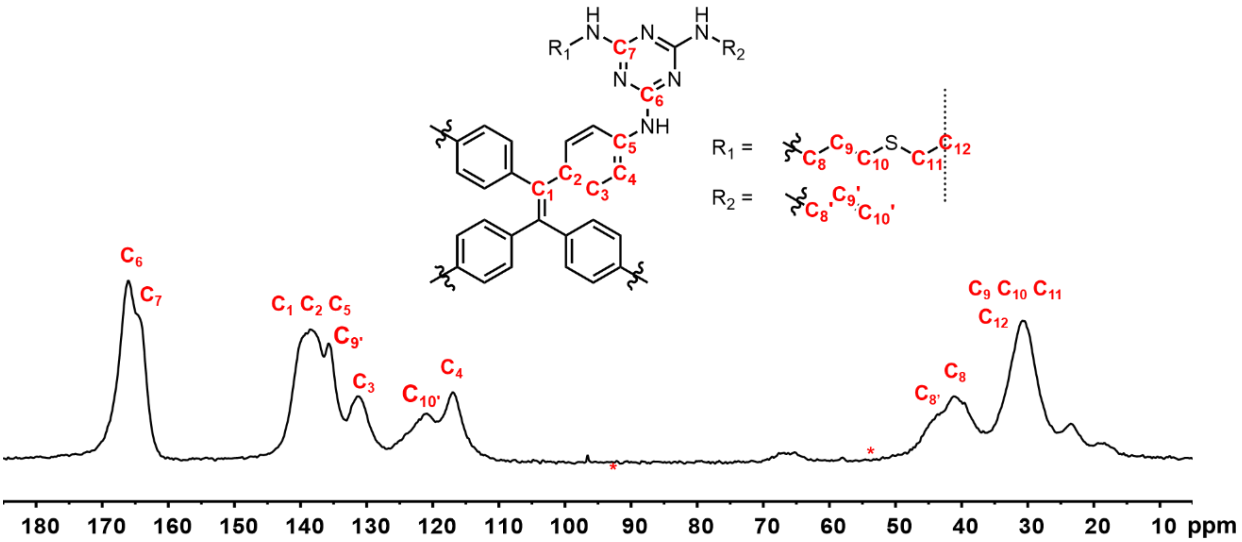

Figure S19. ^{13}C CPMAS NMR (100 MHz, 298K, 10000 rpm) spectrum of H_COF-3 (spinning sidebands are noted as *)

H_COF-4: ^{13}C CPMAS NMR (100 MHz, 298K, 10000 rpm): δ = 166.3, 164.4, 138.7, 135.6, 131.4, 118.17, 116.7, 44.1, 40.6, 30.5. Elemental analysis: [**1**]·$[C_4H_{10}S_2]_{2.55}$·$[CO_2]_{1.70,}$ calc.: C 57.79 %, H 6.14 %, N 22.89 %, S 10.65 %; found: C 57.45 %, H 6.22 %, N 22.23 %, S 10.95 %.

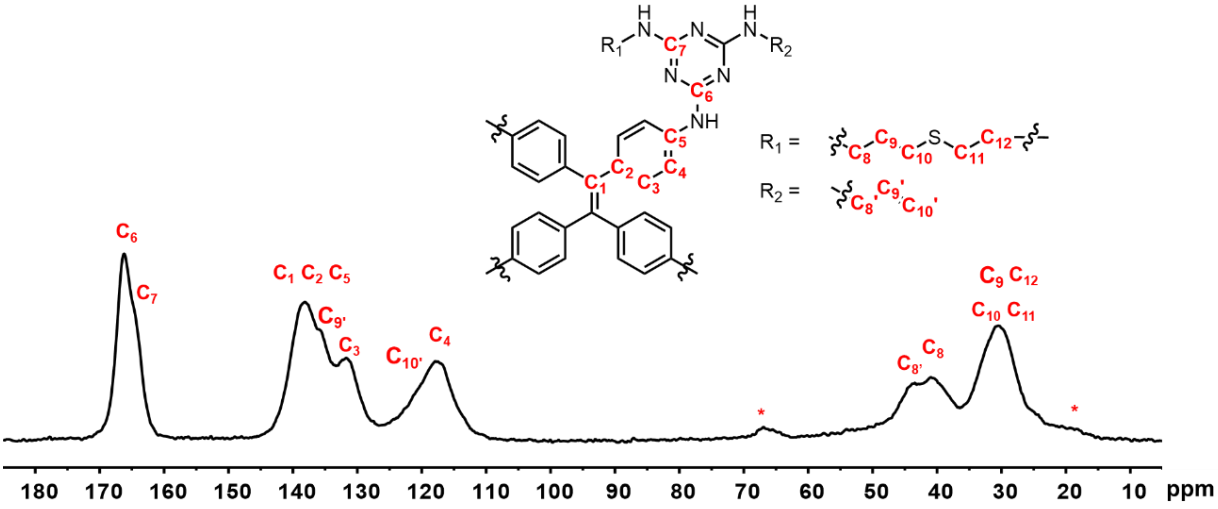

Figure S20. ^{13}C CPMAS NMR (100 MHz, 298K, 10000 rpm) spectrum of H_COF-4 (spinning sidebands are noted as *)

Table S1. Elemental analysis of H_COFs-2-4 synthesized using *methods* 1 and 2. Two parallel batches of H_COFs were synthesized by two individuals and analyzed independently.

H_COFs	Formula	Calc. (%)	Found (%)	max diff. (%)
H_COF-2	[**1**]·$[C_2H_6S_2]_{3.30}$·$[CO_2]_{2.20}$ (*method 1*)	C 54.62 H 5.68 N 21.59 S 13.59	C 54.42 H 5.78 N 21.77 S 13.40	0.35
	[**1**]·$[C_2H_6S_2]_{4.10}$·$[CO_2]_{1.75}$ (*method 2*)	C 53.59 H 5.79 N 20.85 S 16.30	C 53.50 H 5.72 N 20.92 S 16.26	0.09
	[**1**]·$[C_2H_6S_2]_{3.85}$·$[CO_2]_{1.2}$ (*method 2*)	C 54.42 H 5.87 N 21.48 S 15.78	C 54.25 H 6.02 N 21.65 S 15.77	0.17
H_COF-3	[**1**]·$[C_3H_8S_2]_{2.95}$·$[CO_2]_{1.40}$ (*method 2*)	C 56.71 H 6.03 N 21.97 S 12.36	C 56.64 H 6.03 N 22.01 S 12.43	0.07
	[**1**]·$[C_3H_8S_2]_{3.00}$·$[CO_2]_{1.44}$ (*method 2*)	C 56.59 H 6.03 N 21.87 S 12.51	C 56.45 H 6.03 N 22.01 S 12.43	0.14
H_COF-4	[**1**]·$[C_4H_{10}S_2]_{2.55}$·$[CO_2]_{1.70}$ (*method 2*)	C 57.79 H 6.14 N 22.89 S 10.65	C 57.45 H 6.22 N 22.23 S 10.95	0.34
	[**1**]·$[C_4H_{10}S_2]_{2.50}$·$[CO_2]_{2.42}$ (*method 2*)	C 57.24 H 6.00 N 21.53 S 10.27	C 56.83 H 6.23 N 21.94 S 10.62	0.41

S4. Probing alkene reactive sites

In order to probe the number of accessible alkene groups and their reactivities in the crystal lattice of **1** and **2**, we employed ET for the thiol-ene reaction. The products after photoirradiation were analyzed by NMR spectroscopy.

In practice, the mother solution of $\mathbf{1}_{crystal}$ or $\mathbf{2}_{crystal}$ was removed before MeCN was used to wash the surface of the crystals. Fresh MeCN (2 mL) was added to the crystal samples before ET (0.2 mL) was introduced. The sample was kept in the dark for 24 h to allow extensive diffusion into the crystal samples. Another two portions of ET (0.2 mL) were introduced subsequently after 24 h and 48 h. The glass vial was irradiated under UV light (medium-pressure 175-watt Hg lamp) for 72 h with forced air cooling. The crystal samples were collected and washed with an excess of MeCN to remove unreacted ET. The crystal samples were dried under reduced pressure and dissolved in DMSO-d_6 for NMR analysis.

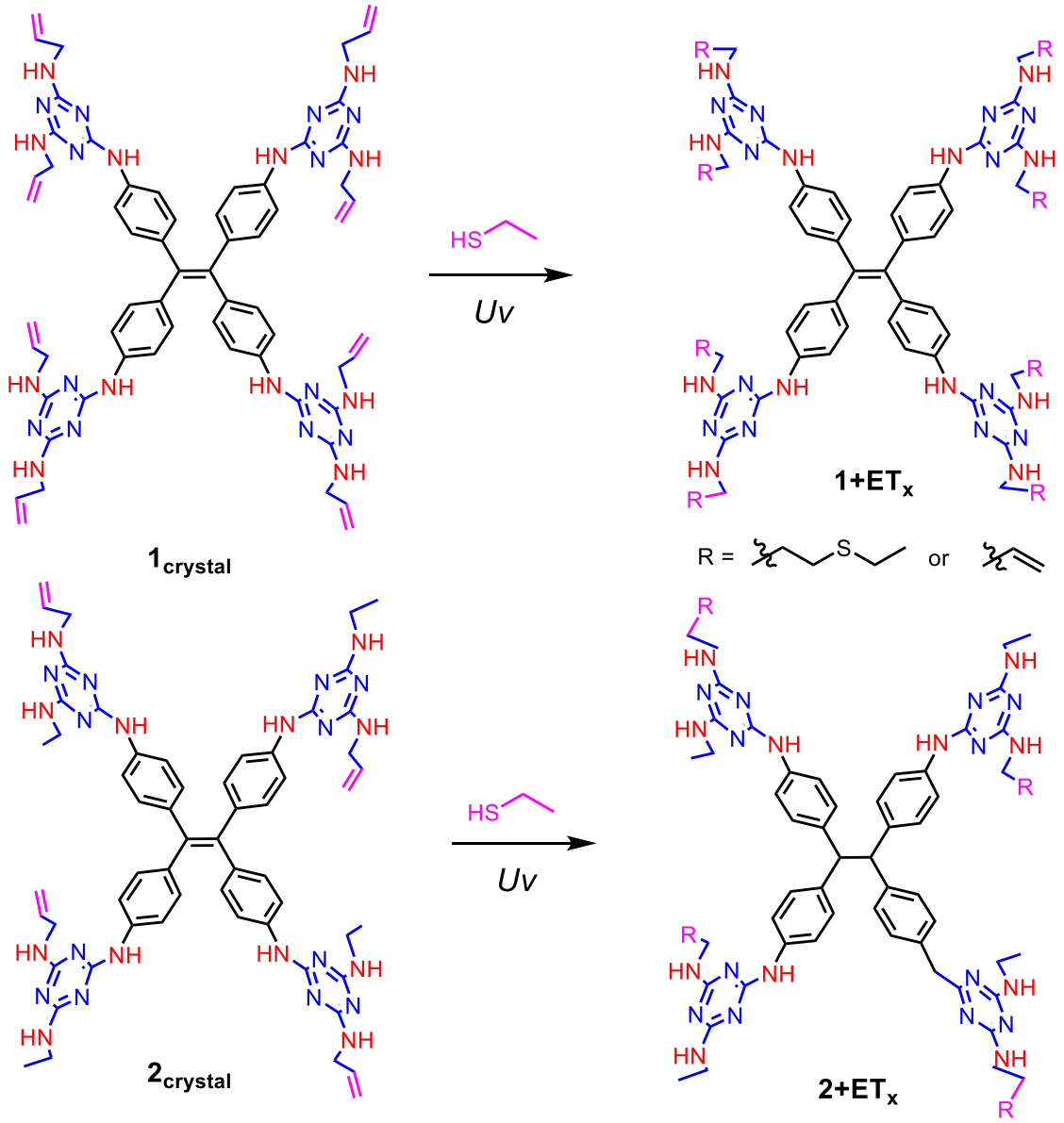

Scheme S2. SCSC transformation of $\mathbf{1}_{crystal}$ and $\mathbf{2}_{crystal}$ with ET via photo-irradiated thiol-ene reaction.

Table S2. Synthesis of ET-substituted products with varied ET diffusion and UV irradiation time. The averaged residual number of allyl groups listed herein were calculated based on the integrations of the alkene proton resonances in the ^{1}H NMR spectra (e.g., Figures S23-S29).

	entry	ET amount (μL)	diffusion time (day)	UV time (day)	residual allyl groups	Figure
1$_{crystal}$	1	600	3	3	3.3/8	S23
	2	600	3	14	1.3/8	S23
	3	300	3	2	5.1/8	
	4	600	2	1	5.0/8	
	5	600	2	2	4.9/8	
	6	600	2	2.5	4.2/8	
	7	600	2	2.5	4.3/8	S29
	8	600	4	2	4.2/8	
2$_{crystal}$	1	600	3	3	1.0/4	S26
	2	600	3	14	1.0/4	S26

[1 + x·ET]: The averaged x was calculated as [**1** + 4.8ET**]** and [**1** + 6.7ET**]** respectively after 3 and 14 d of diffusion. The slow increase in the monomer-to-ET ratio between 3 and 14 d suggests a difference in accessibility of the alkenes within the crystal lattice. The slow increase from 4.8ET to 6.7 ET following an additional 11 d of diffusion suggest that (1) half of the reactive alkenes are present in sterically easy accessible locations within the monomer crystals; and (2) the remaining alkenes are still accessible, as evidenced by the presence of *m/z* peaks corresponding to [**1** + 5ET**]**$^+$, [**1** + 6ET**]**$^+$, [**1** + 7ET**]** $^+$, and [**1** + 8ET**]**$^+$ in the mass spectrum (Figure S21).

[2 + y·ET]: The averaged y was calculated as [**2** + 2.9ET**]** and [**2** + 3.0ET**]** respectively after 3 and 14 d of diffusion. Similarly, mass spectra data clearly show the existence of [**2** + 4ET**]**$^+$ following 14 d of diffusion even though ^{1}H NMR spectra only reveal [**2** + 3.0ET**]** species as the averaged extent of reaction, again supporting the accessibility and reactivity of all four alkenes of **2**$_{crystal}$, with only 1-2 of the four alkenes being kinetically disfavored due to its location within the crystal lattice.

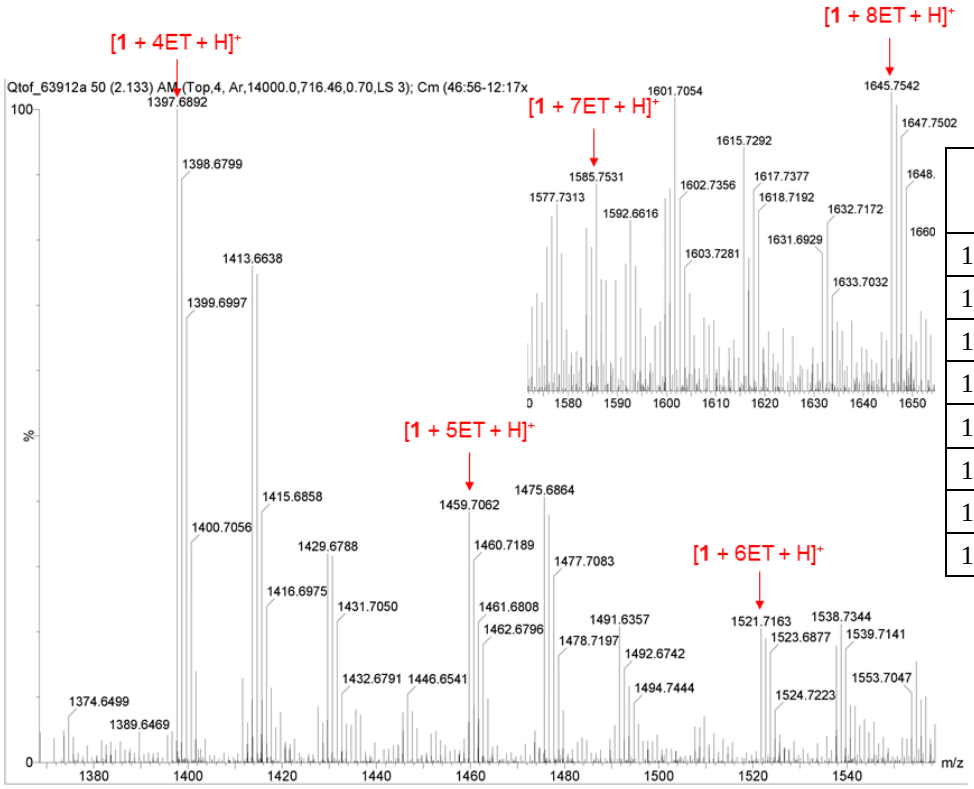

m/z	relative Intensity
1211.5537	n.o.
1273.5817	n.o.
1335.6597	13.50
1397.6892	100.00
1459.7062	38.33
1521.7163	20.46
1583.7531	7.72
1645.7532	14.16

Figure S21. High resolution ESI mass spectrum of [**1** + 6.7ET] mixture, which is composed of **1**•4ET (found *m/z* = 1396.6892, calc. *m/z* = 1396.6820), **1**•5ET (found *m/z* = 1458.7062, calc. *m/z* = 1458.7010), **1**•6ET (found *m/z* = 1520.7163, calc. *m/z* = 1520.7200), **1**•7ET (found *m/z* = 1582.7344, calc. *m/z* = 1582.7390) and **1**•8ET (found *m/z* = 1644.7542, calc. *m/z* = 1644.7581). The consistent occurrence of *m/z* = [M + 16n] (n = 1, 2) in the spectrum can be ascribed to sulfoxide derivatives, which are the oxidation products of those thioethers.

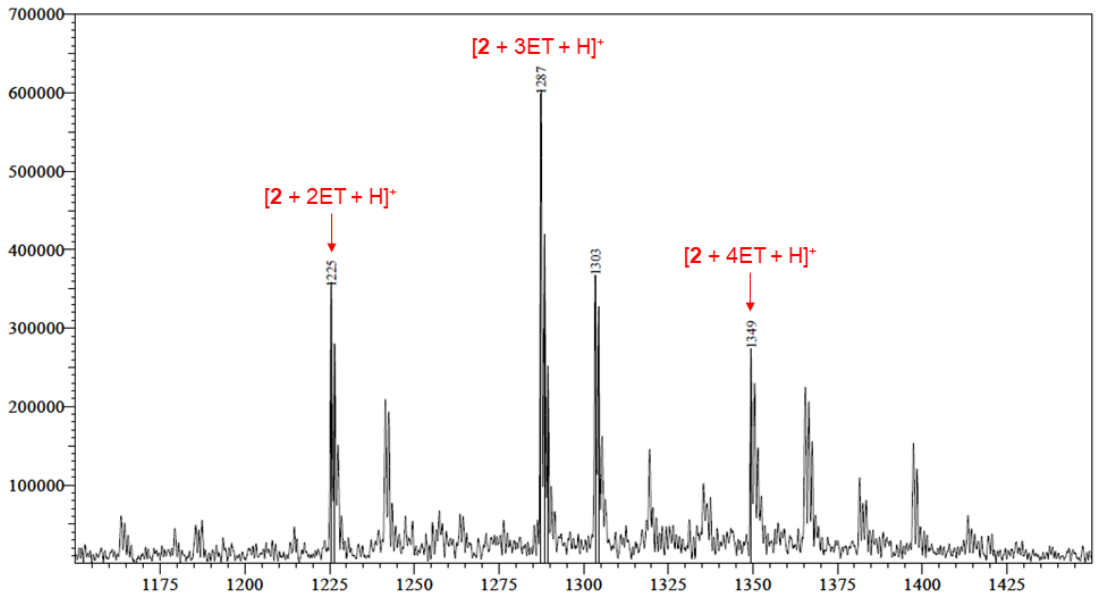

Figure S22. ESI mass spectrum of [**2** + 2.9ET], presents **2**•2ET (*m/z* = 1225.45), **2**•3ET (*m/z* = 1287.45) and **2**•4ET (*m/z* = 1349.45). The consistent occurrence of *m/z* = [M + 16n] (n = 1, 2) in the spectrum can be ascribed to sulfoxide derivatives, which are the oxidation products of those thioethers.

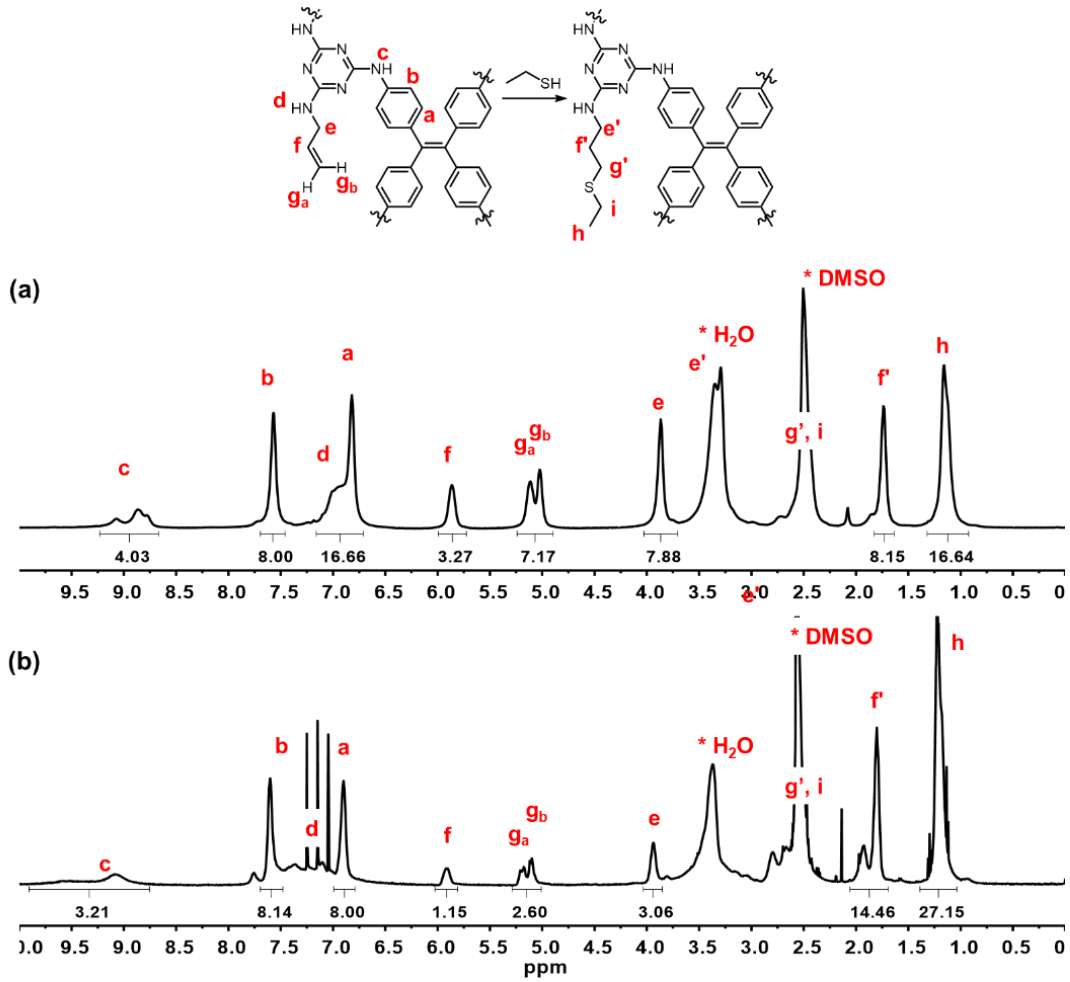

Figure S23. ^{1}H NMR spectra (298 K, 500 MHz, DMSO-d_6) of the dissolved crystal samples $\mathbf{1}_{\mathbf{crystal}}$ immersed in 2 mL MeCN solution of ET (0.6 mL) for (a) 3 d, and (b) 14 d, followed by 3 d UV irradiation.

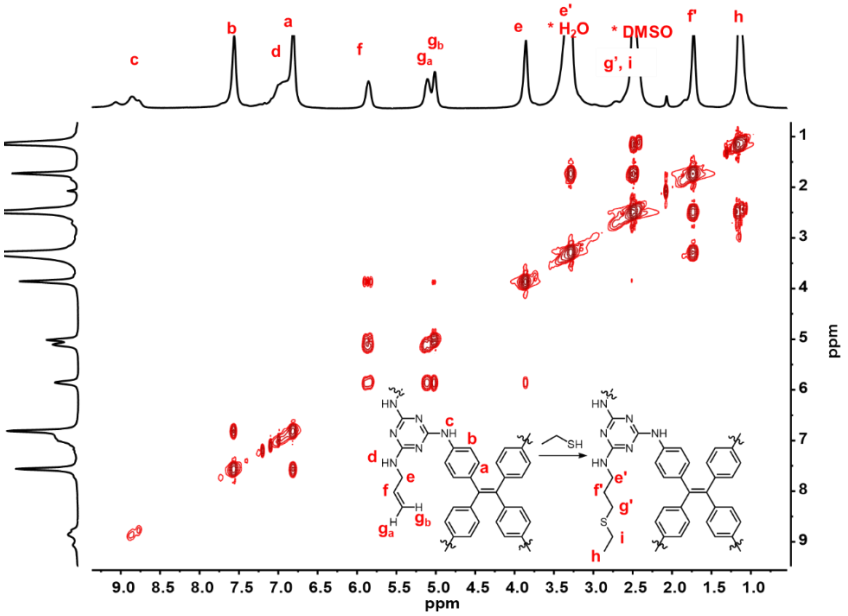

Figure S24. ^{1}H-^{1}H COSY NMR spectrum (298 K, 500 MHz, DMSO-d_6) of the dissolved crystal samples $\mathbf{1}_{\mathbf{crystal}}$ immersed in 2 mL MeCN solution of ET (0.6 mL) for 3 d, followed by 3 d UV irradiation.

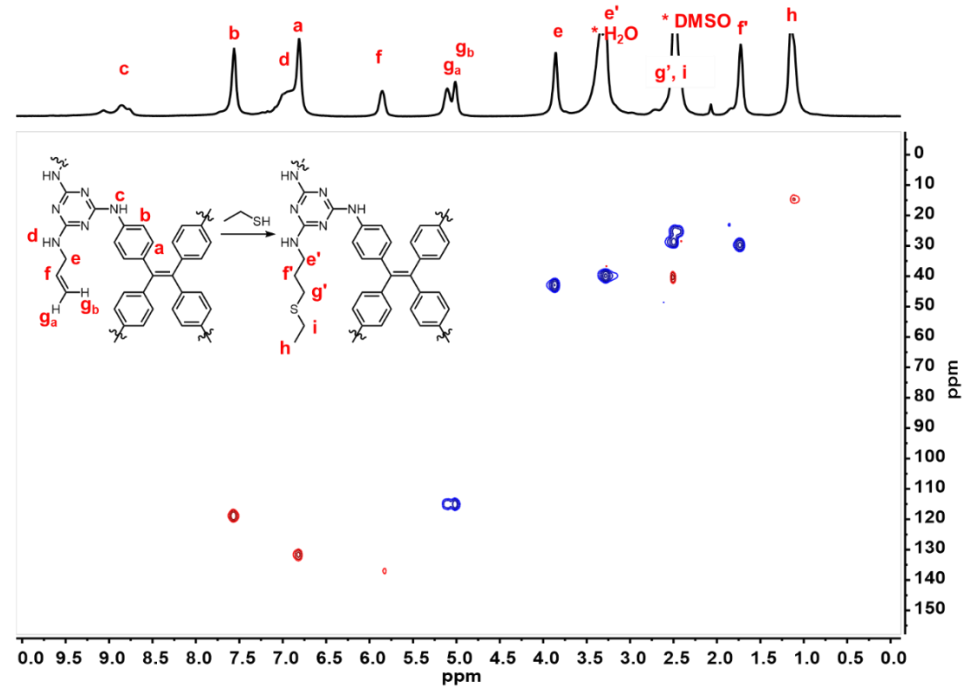

Figure S25. ^{1}H-^{13}C HSQC NMR spectrum (298 K, 500 MHz, DMSO-d_6) of the dissolved crystal samples $\mathbf{1}_{\mathbf{crystal}}$ immersed in 2 mL MeCN solution of ET (0.6 mL) for 3 d, followed by 3 d UV irradiation.

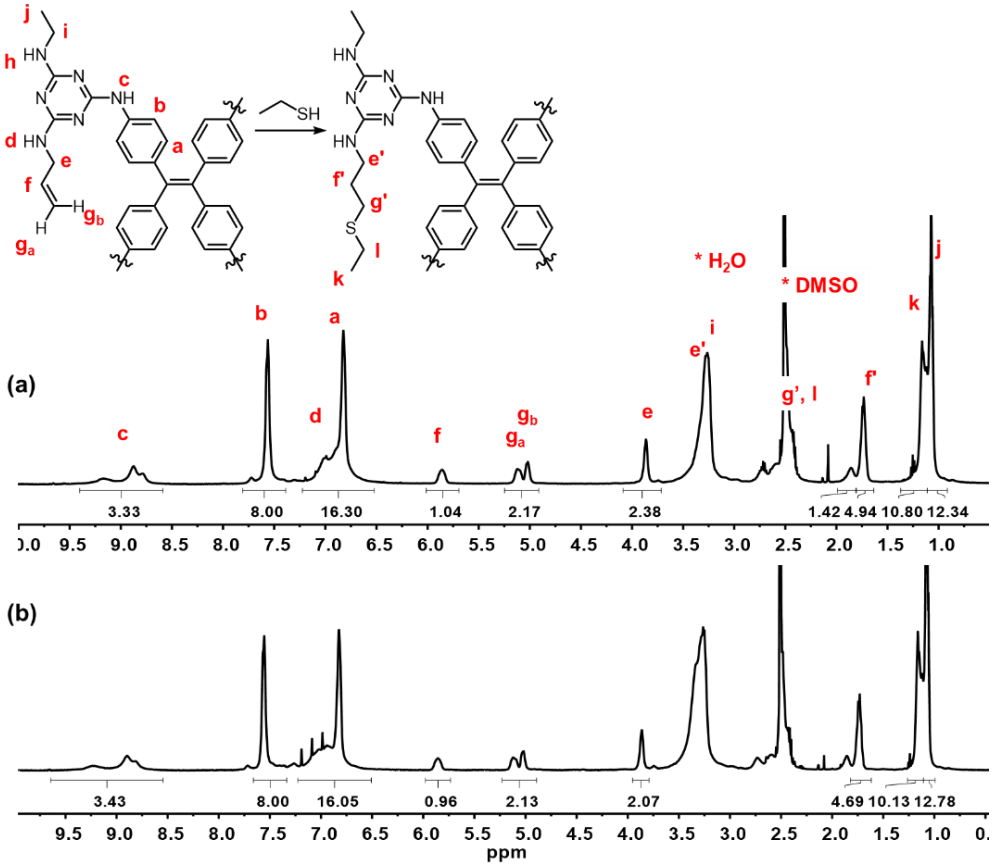

Figure S26. ^{1}H NMR spectra (298 K, 500 MHz, DMSO-d_6) of the dissolved crystal samples $\mathbf{2}_{\mathbf{crystal}}$ immersed in 2 mL MeCN solution of ET (0.6 mL) for (a) 3 d, and (b) 14 d, followed by 3 d UV irradiation.

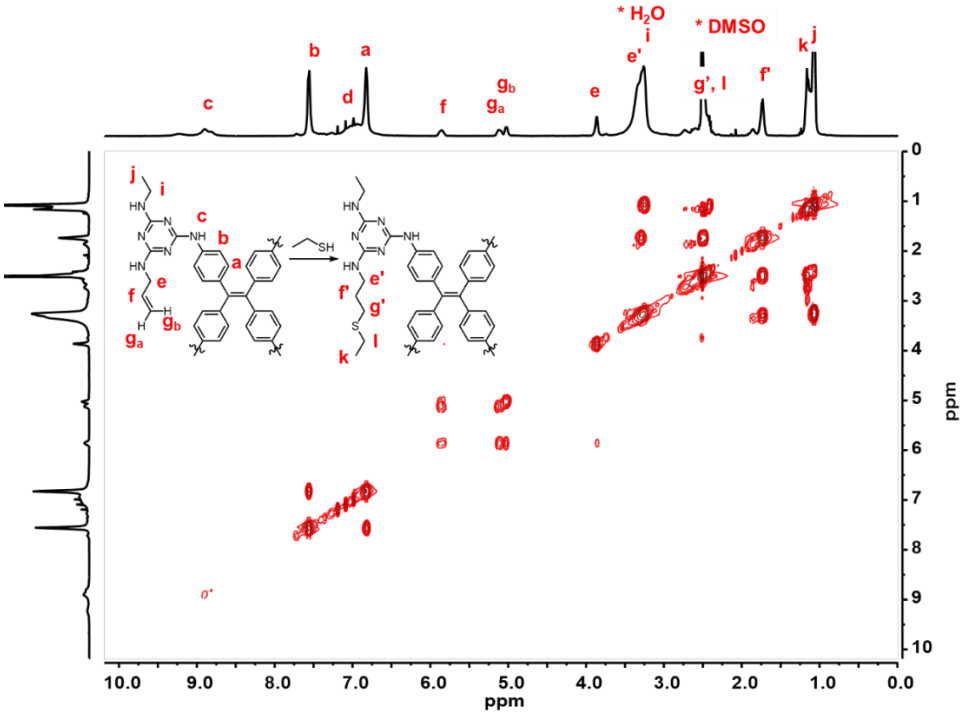

Figure S27. ^{1}H-^{1}H COSY NMR spectrum (298 K, 500 MHz, DMSO-d_6) of the dissolved crystal samples $\mathbf{2}_{\mathbf{crystal}}$ immersed in 2 mL MeCN solution of ET (0.6 mL) for 3 d, followed by 3 d UV irradiation.

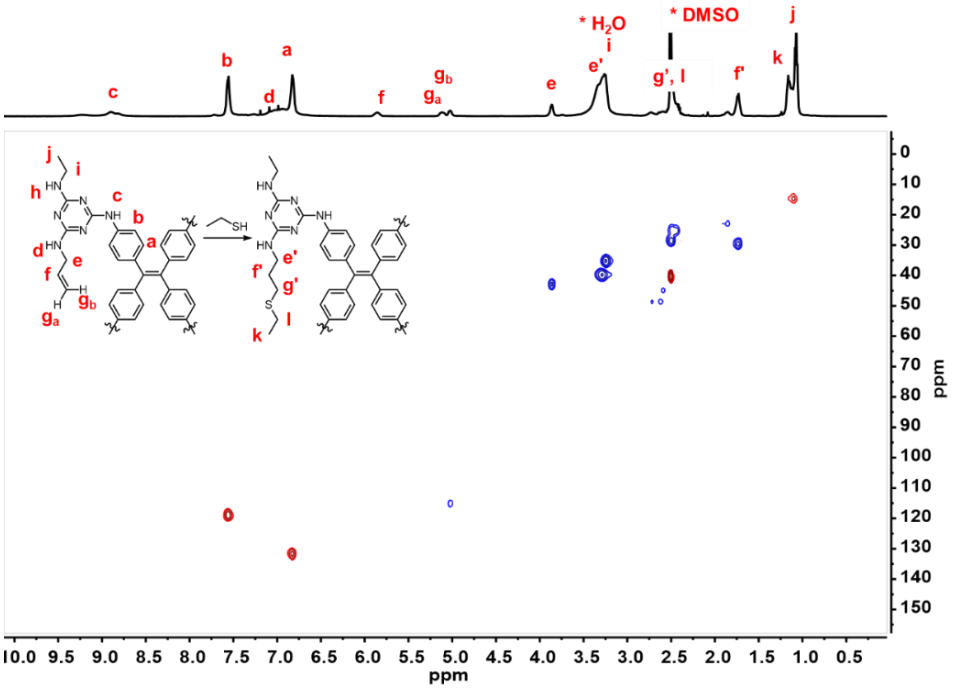

Figure S28. ^{1}H-^{13}C HSQC NMR spectrum (298 K, 500 MHz, DMSO-d_6) of the dissolved crystal samples $\mathbf{2}_{\mathbf{crystal}}$ immersed in 2 mL MeCN solution of ET (0.6 mL) for 3 d, followed by 3 d UV irradiation.

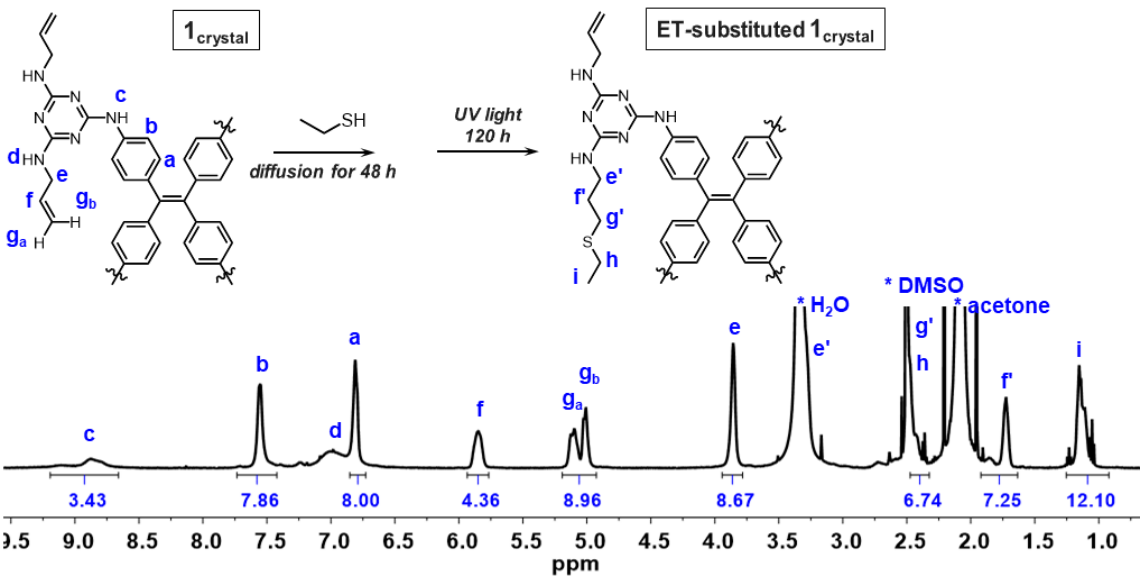

Figure S29. ^{1}H NMR spectrum (298 K, 500 MHz, DMSO-d_6) of crystal samples $\mathbf{1}_{\mathbf{crystal}}$, in which nearly four (3.60 by averaged alkene protons integration) of the eight alkenes have been substituted by ET.

S5. Synthesis of P5-P8

The mother solution of $\mathbf{2}_{\mathbf{crystal}}$ was removed before MeCN (3 mL) was added to wash the surface of the crystal samples. The resulting cloudy solution was removed. This process was repeated for another two times. Fresh MeCN (2 mL) was added to the crystal samples before alkyl(di)thiol (3.6 mmol) was added. The sample was kept in the dark for 24 h to allow extensive diffusion into $\mathbf{2}_{\mathbf{crystal}}$. Another two portions of alkyl(di)thiol (3.6 mmol) were introduced subsequently after 24 h and 48 h. The glass vial was irradiated under UV light (medium-pressure 175-watt Hg lamp) for 72 h with forced air cooling. The crystal samples were collected and washed with an excess of MeCN to remove the unreacted thiol and dried under reduced pressure. The crystal samples were dissolved in DMF-d_7 for NMR analysis.

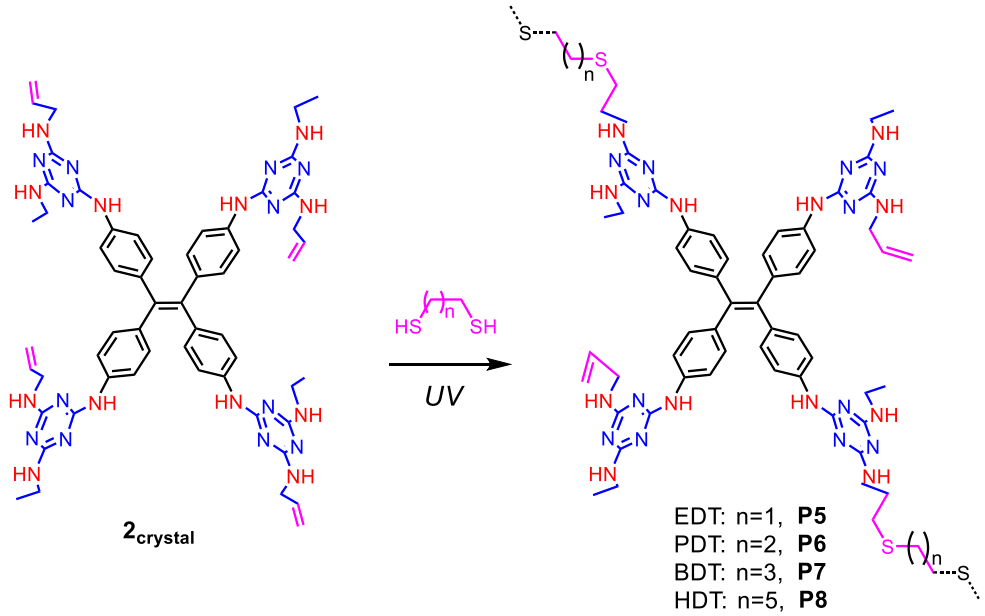

Scheme S3. SCSC transformation of $\mathbf{2}_{\mathrm{crystal}}$ to **P5-8** via photo-irradiated thiol-ene reaction. Alkyldithiols with different chain lengths (n = 1-5) were employed as cross-linkers in the SCSC transformation.

P5: ^{1}H NMR (500 MHz, DMF-d_7, 298 K): δ = 8.96 (m, 4H, *N*H$_c$), 7.74 (bs, 8H, H$_b$), 6.95 (bs, 8H, H$_a$), 6.75 (m, 4H + 4H, *N*H$_d$ + *N*H$_h$), 5.93 (bs, ~1.8H, residual H$_f$), 5.15 (m, ~1.8H, residual H$_g$), 5.01 (m, ~1.8H, residual H$_g$), 3.95 (m, ~3.6H, residual H$_e$), 3.39 (m, ~4.4H, H$_{e'}$), 3.34 (m, 8H, H$_i$), 2.72 (m, ~4.4, H$_{k'}$), 2.63 (m, ~4.4H, H$_{g'}$), 1.84 (bs, ~4.2H, H$_{f'}$), 1.13 (m, 12H, H$_j$). ^{13}C NMR (150 MHz, DMF-d_7, 298 K): δ = 166.15, 164.52, 139.58, 138.91, 137.51, 136.53, 131.43, 118.28, 114.35, 42.89, 39.53, 35.13, 31.86, 29.95, 29.11, 14.71.

P6: ^{1}H NMR (500 MHz, DMF-d_7, 298 K): δ = 8.96 (m, 4H, *N*H$_c$), 7.73 (bs, 8H, H$_b$), 6.94 (bs, 8H, H$_a$), 6.77 (m, 4H + 4H, *N*H$_d$ + *N*H$_h$), 5.92 (bs, ~1.7H, residual H$_f$), 5.16 (m, ~1.7H, residual H$_g$), 5.01 (m, ~1.7H, residual H$_g$), 3.95 (m, ~3.4H, residual H$_e$), 3.39 (m, ~4.6H, H$_{e'}$), 3.34 (m, 8H, H$_i$), 2.59 (m, ~9.2H, H$_{g'}$ + H$_{k'}$, overlapped with some free dithiol proton), 1.84 (m, ~6.9H, H$_{f'}$ + H$_{l'}$, overlapped with some free dithiol proton), 1.13 (m, 12H, H$_j$). ^{13}C NMR (150 MHz, DMF-d_7, 298 K): δ = 166.22, 164.55, 139.61, 138.85, 137.51, 136.54, 131.44, 118.27, 114.35, 42.88, 39.54, 35.17, 29.91, 29.04, 14.72.

P7: ^{1}H NMR (500 MHz, DMF-d_7, 298 K): δ = 8.94 (m, 4H, *N*H$_c$), 7.74 (bs, 8H, H$_b$), 6.94 (bs, 8H, H$_a$), 7.04-6.56 (m, 4H + 4H, *N*H$_d$ + *N*H$_h$), 5.93 (bs, ~2.2H, residual H$_f$), 5.16-5.02 (m, ~4.4 H, residual H$_g$), 3.95 (m, ~4.4 H, residual H$_e$), 3.56-3.33 (m, 8H + 3.6 H, H$_i$ + H$_{e'}$ + H$_{e''}$), 2.66-2.50 (m, 8.2 H), 1.84 (bs, 3.6 H, H$_{f'}$ + H$_{f''}$), 1.65 (bs, 4.6 H), 1.13 (m, 12H, H$_j$). ^{13}C NMR (150 MHz, DMF-d_7, 298 K): δ = 166.22, 164.55, 139.61, 138.87, 137.51, 136.55, 131.43, 118.27, 114.35, 42.89, 39.77, 39.57, 35.15, 33.05, 31.07, 29.95, 28.61, 28.19, 14.71.

P8: ^{1}H NMR (500 MHz, DMF-d_7, 298 K): δ = 8.94 (m, 4H, *N*H$_c$), 7.74 (bs, 8H, H$_b$), 6.94 (bs, 8H, H$_a$), 7.04-6.65k (m, 8H, *N*H$_d$ + *N*H$_h$), 5.93 (bs, ~2.6 H, residual H$_f$), 5.18-5.01 (m, ~5.2 H, residual H$_g$), 3.94 (m, ~5.2 H, residual H$_e$), 3.46-3.32 (m, 8H + 2.8 H, H$_i$ + H$_{e'}$ + H$_{e''}$), 2.59-2.48 (m, 8.1 H), 1.84 (bs, ~2.8 H, H$_{f'}$ + H$_{f''}$), 1.56 (m, 5.4 H), 1.37 (m, 5.4 H), 1.13 (bs, 12 H, H$_j$). ^{13}C NMR (150 MHz, DMF-d_7, 298 K): δ = 166.28, 164.67, 139.77, 139.06, 137.69, 136.69, 131.60, 118.44, 114.54, 43.05, 39.95, 39.74, 35.39, 31.72, 30.13, 29.67, 29.34, 29.10, 27.96, 27.87, 27.81, 24.16,23.66, 14.87.

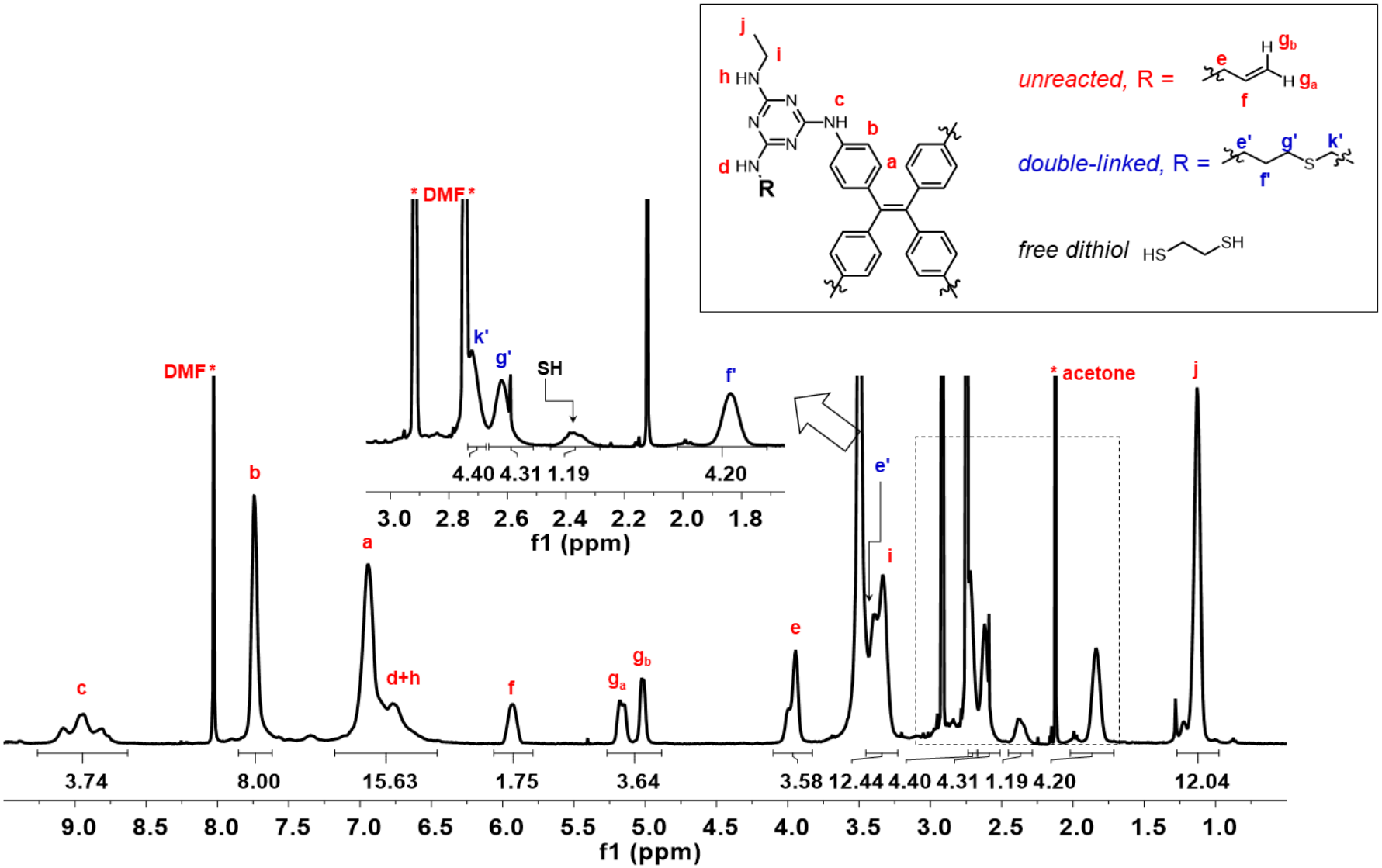

Figure S30. ^{1}H NMR spectrum (298K, 500 MHz, DMF-d_7) of **P5**

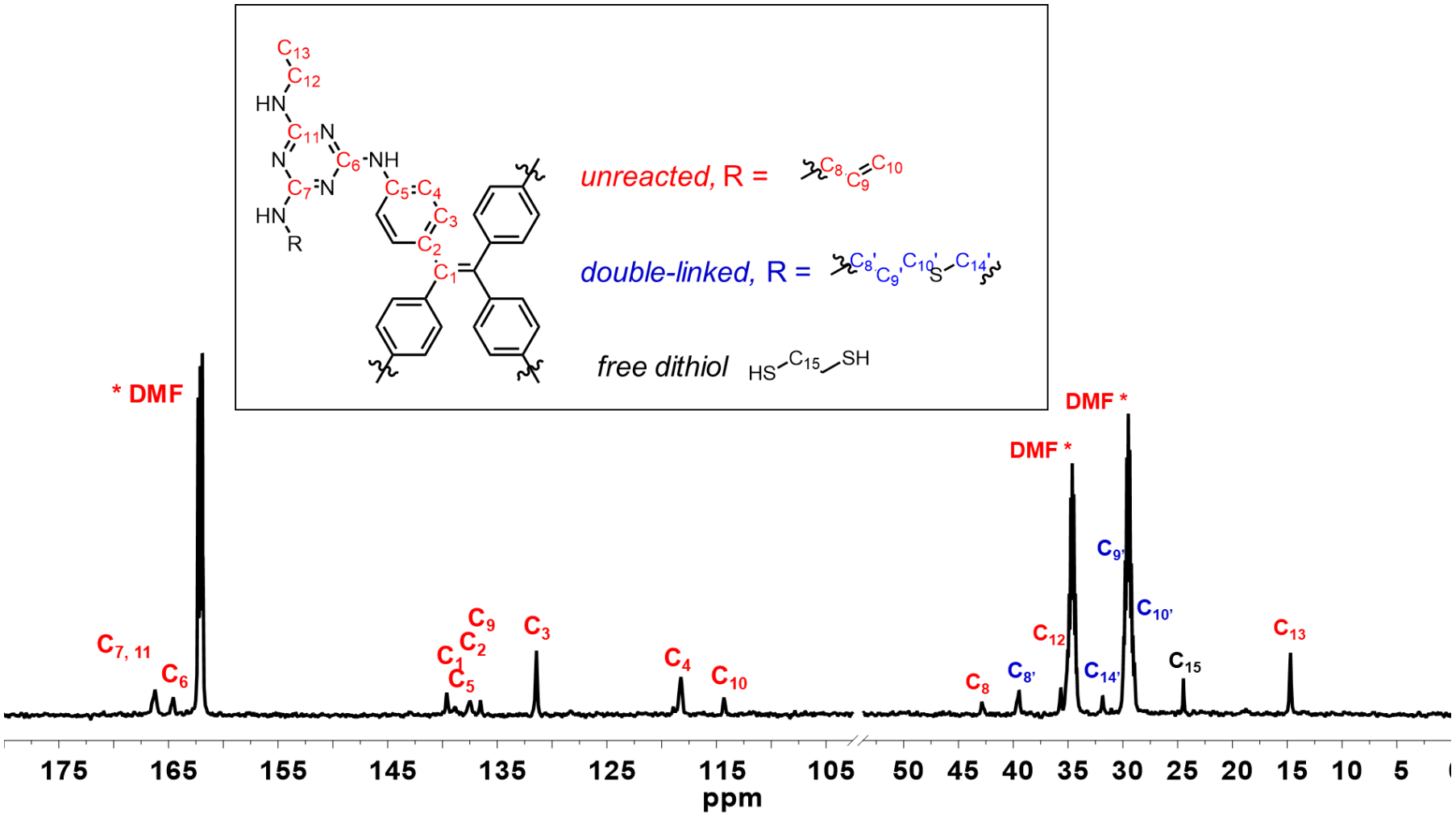

Figure S31. ^{13}C NMR spectrum (298K, 150 MHz, DMF-d_7) of **P5**

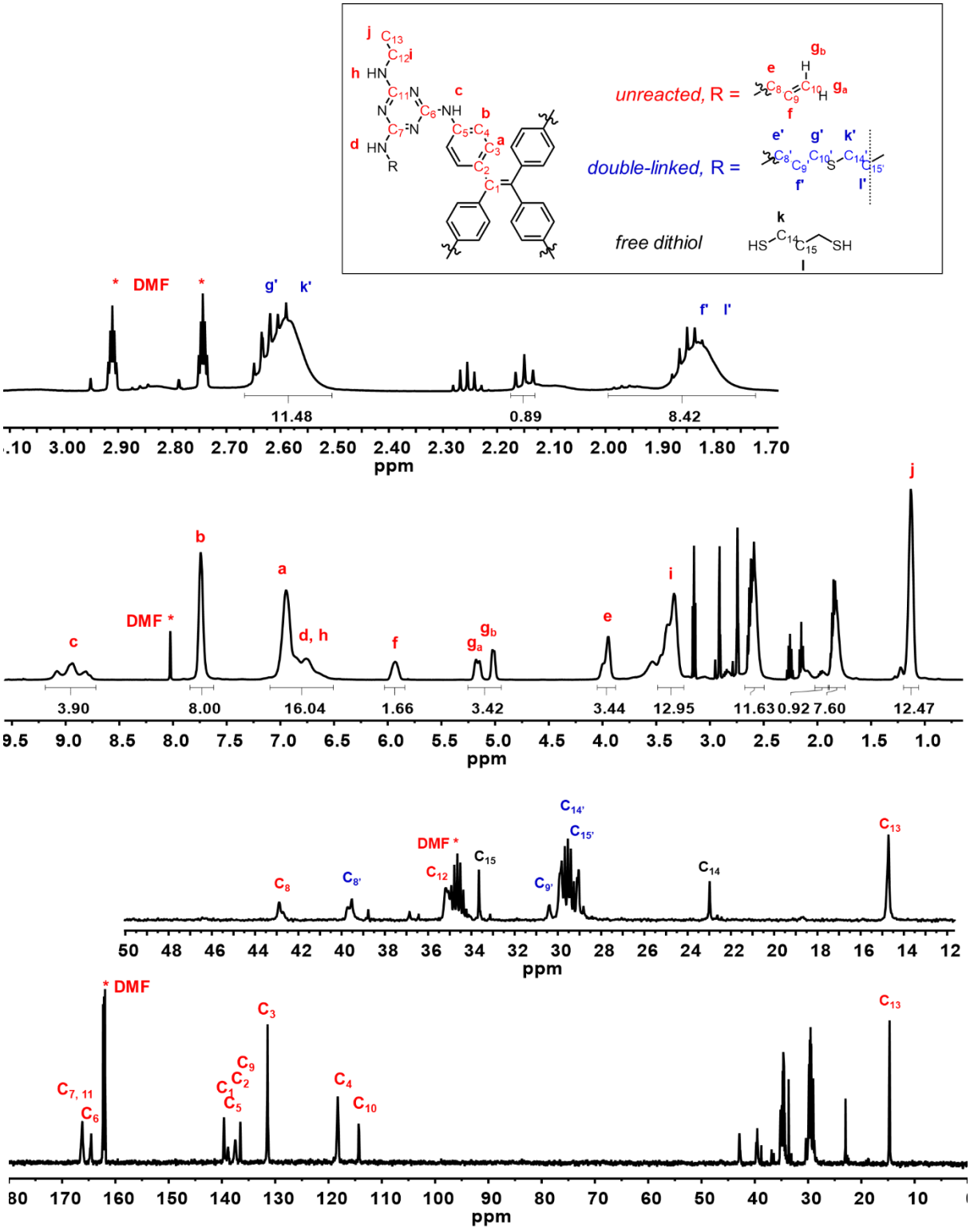

Figure S32. ^{1}H NMR and ^{13}C spectra (298K, 500 and 150 MHz, DMF-d_7) of **P6**. No significant amount of mono-substitute product was identified based on the proton integration of f'+l'.

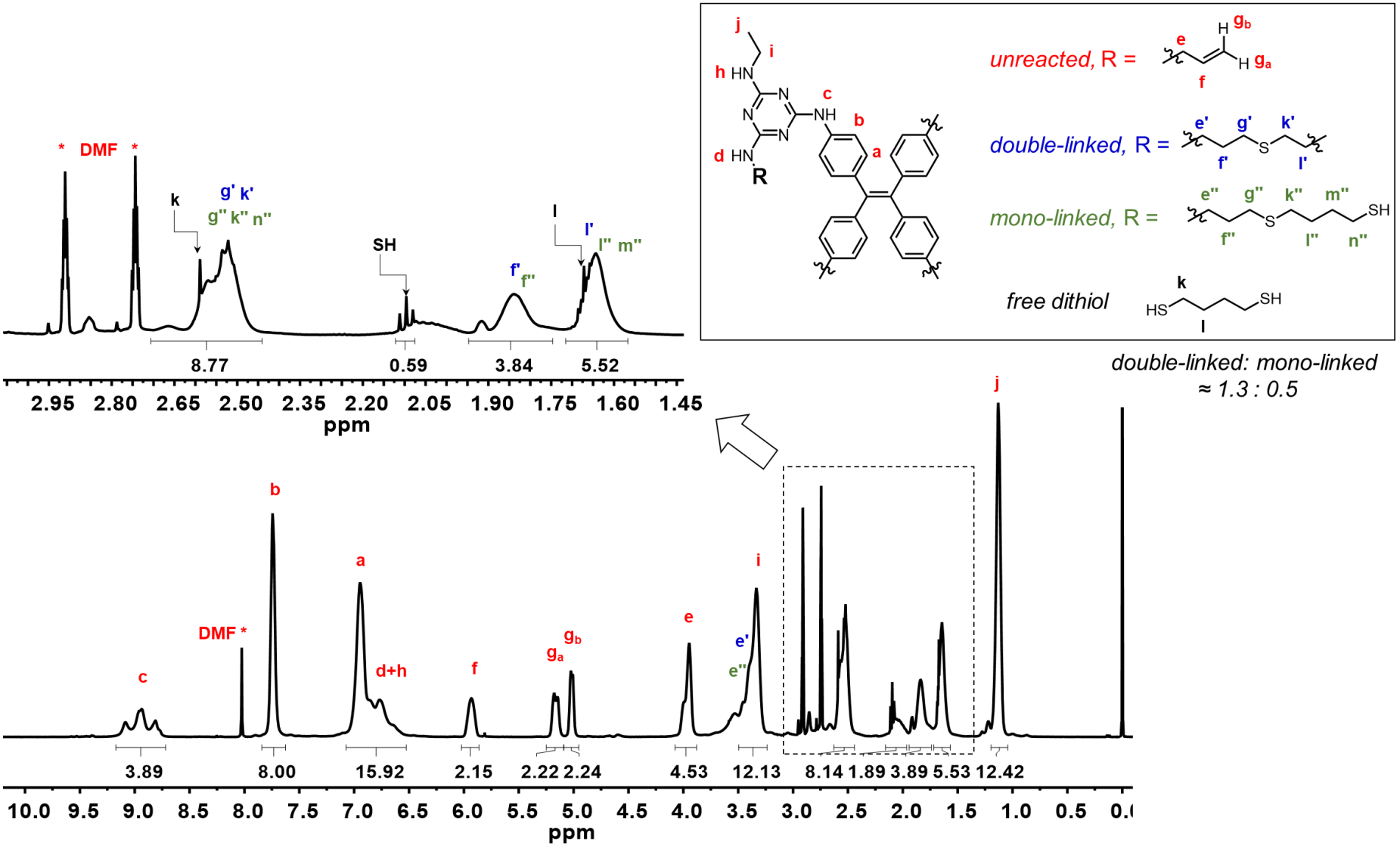

Figure S33. ^{1}H NMR spectrum (298K, 500 MHz, DMF-d_7) of **P7**

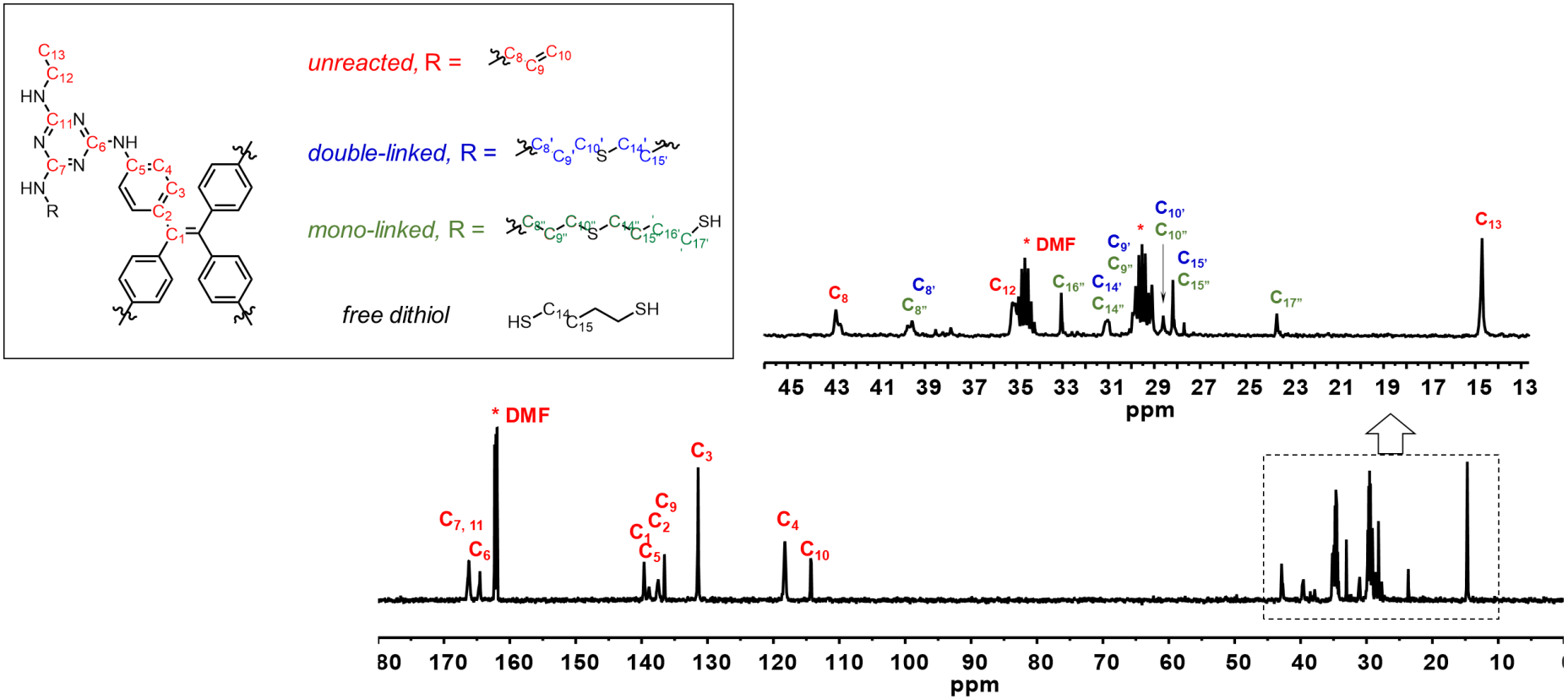

Figure S34. ^{13}C NMR spectrum (298K, 150 MHz, DMF-d_7) of **P7**

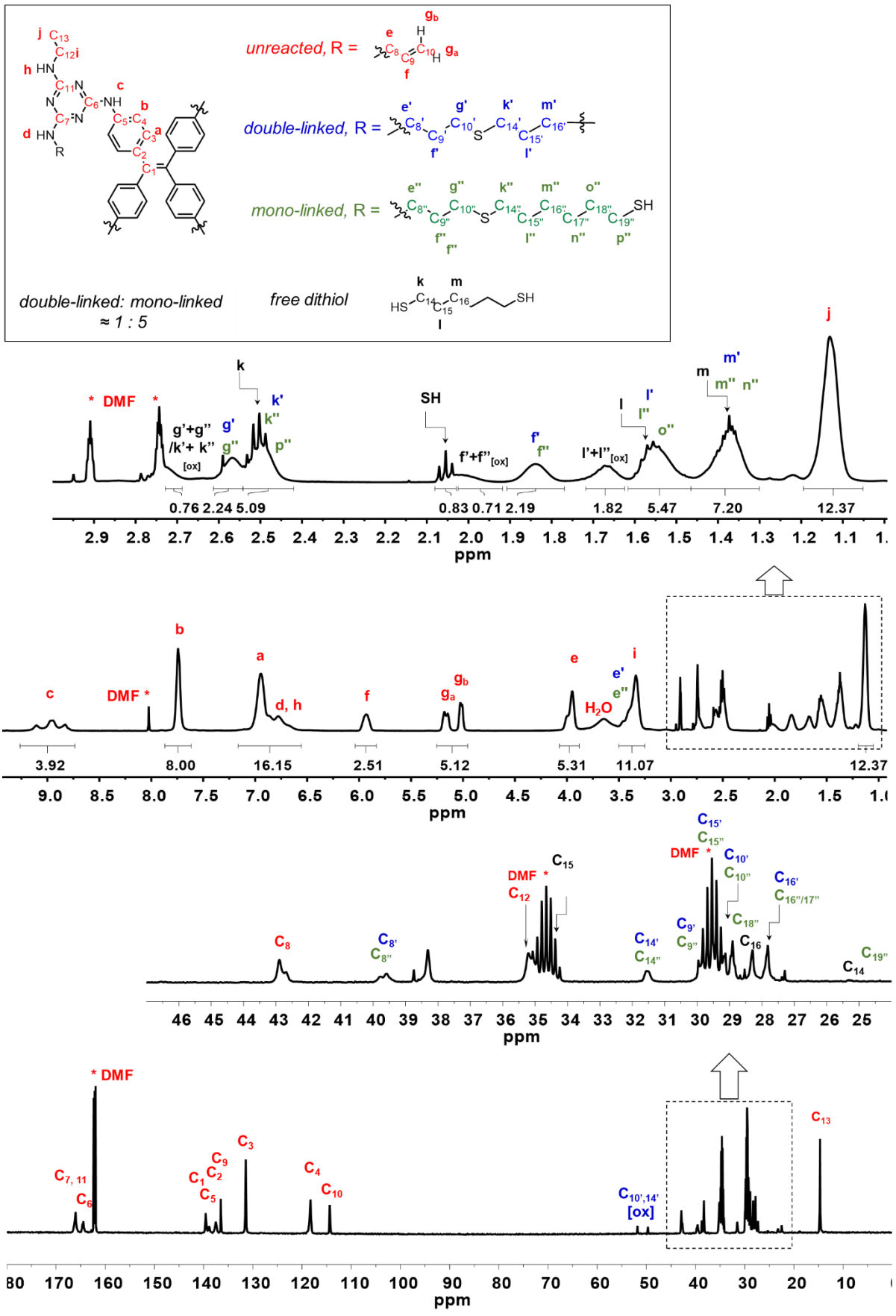

Figure S35. ^{1}H and ^{13}C NMR spectrum (298K, 500 and 150 MHz, DMF-d_7) of **P8**

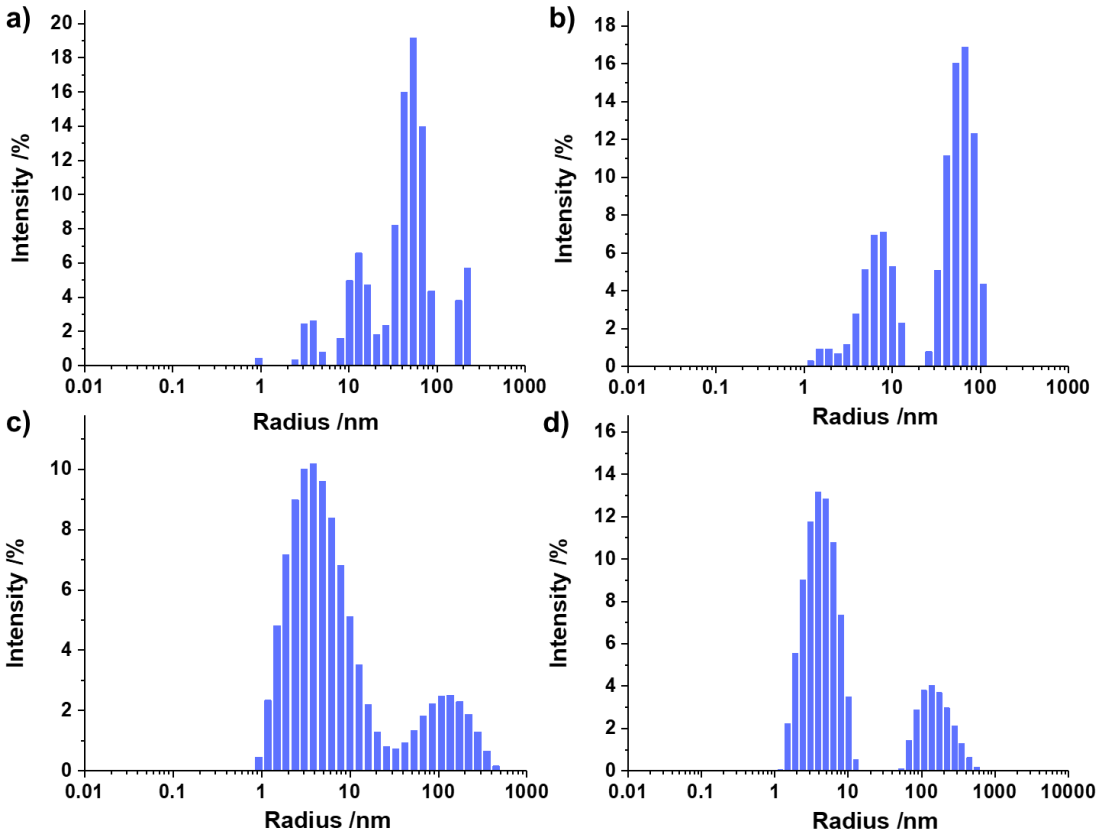

Figure S36. Dynamic light scattering (DLS) patterns of (a) **P5**, (b) **P6**, (c) **P7** and (d) **P8** in DMSO. Small amount of densely crosslinked polymers is insoluble in DMSO, which has been removed using a syringe filter. The solvodynamic radii of the dissolved oligomers lie in 1 – 20 (oligomer) and 50 - 600 nm (polymer) range.

S6. Single crystal X-ray crystallography

Single crystal X-ray diffraction data of monomers $\mathbf{1}_{crystal}$, $\mathbf{2}_{crystal}$, and **P5** were collected using Bruker D_8 Venture diffractometer at 150 K; **P6**, **P7**, and H_COF-2-4 were collected at either the 3W1A beamline station in the Beijing synchrotron radiation facility (BSRF) or the Argonne advance photon source (APS) in the Argonne national laboratory.

Single-crystal X-ray structures were solved by intrinsic phasing methods using ShelXT and refined against F^2 on all data by full-matrix least squares with SHELXL.[3,4] All non-hydrogen atoms were refined anisotropically. All hydrogen atoms bound to carbon atoms were modeled at geometrically constrained positions and refined using a riding model. Positions for hydrogen atoms associated with heteroatoms were located from residual density and allowed to refine via a riding model. The isotropic displacement parameters of the hydrogen atoms were fixed to 1.2 times the *U* value of the atoms they are linked to (1.5 *U* for methyl groups). Refinement of disordered solvent molecules present in the crystal was attempted, but positions for the solvent molecules were poorly determined. For monomers

1$_{crystal}$ and **2**$_{crystal}$, a second structural model was refined with contributions from the solvent molecules removed from the diffraction data using the solvent bypass ("SQUEEZE") procedure in PLATON.[5] No positions for the host network differed by more than two standard uncertainties (s.u.) between these two refined models. The electron count from the "squeeze" model converged in satisfactory agreement with the number of solvate molecules predicted by the complete refinement. The "squeezed" data are reported here. In all H_COFs **2-3** and **P5-6**, the unit cell included a large region of disordered alkyldithioether moieties, which could not be completely modeled as discrete atomic sites. More details will be discussed in the section below. CCDC 1908801-1908807 contains the supplementary crystallographic data, which can be accessed through the Cambridge Crystallographic Data Centre at https://www.ccdc.cam.ac.uk/.

Monomer 1$_{crystal}$. The X-ray structure for monomer **1** was refined in the orthorhombic space group *Fddd* with the asymmetric unit comprised of one-half molecule of **1**. The four melamine moieties of **1** provide a large number of hydrogen-bond (H-bond) donors and acceptors and, coupled with the non-planar conformation of the molecule, allowing it to interact with six neighboring molecules through a series of N-H···N hydrogen bonds [N···N distances (Å): N(1) –N(2) 3.035(4); N(3) – N(11) 3.018(4); N(7) – N(5) 2.959(4); N(6) – N(9) 3.093; N(12) – N(8) 2.970(4)]. The H-bonding pattern ultimately produces a 3D H-bonded network. However, it is worth noting that the network can be viewed as stacks of monomer bilayers, stacking perpendicular to the *b*-axis. The bilayers are comprised of interdigitated and H-bonded monomers wherein all of the central C=C bonds of the TPE core are aligned in parallel along the direction of the *a*-axis (red, Fig S37c). The adjacent bilayers (blue, Fig S37c) are oriented such that the central C=C bonds are angled approx. 60° from the *a*-axis. As a consequence of such layered stacking, 2D channels of solvent-accessible void space exists primarily between bilayers and extend through the crystal parallel to the *ac*-plane (Fig S39b).

Due to the offset of nearest-neighbor monomers, notable secondary features are observed in the packing of **1**. First, when viewed along the *a*-axis, the bilayer structures possess an undulating sinusoidal shape, wherein the stacked TPE cores constitute the broader parts of the waveform (Fig S39). Close packing is facilitated by an offset between neighboring bilayers, resulting in an approx. 90° phase difference. Second, when viewed along the [110] direction, a series of hexagonal pore-like channels become apparent (Fig S39a). These channels result from close proximity of melamine arms of neighboring monomers and extend infinitely through the crystal. Notably, the walls of the channels are lined with allyl groups (C_{25} and C_{28}) that occupy the space. The packing density of the allyl groups is lower than that of the TPE cores, providing a small amount of space for the allyl groups to move, contributing to the disorder. Additionally, the same hexagonal channel motif can be seen when viewed along the [$1\bar{1}0$] direction. The two sets of channels are canted at approx. 60° to each other and offset along the *b*-axis such that they do not intersect. The remaining four allyl groups (C_{22} and C_{31}) are situated in the congested regions of the lattice between neighboring channels. Curiously, the melamine arms of four monomers come together in this region and produce a junction between the adjacent hexagonal channels. This junction places eight allyl groups, all symmetry equivalents of C_{22} and C_{31}, in close proximity and is exposed to the void space on both faces of the bilayer structure (Fig S39a). These two domains, the hexagonal channel and the junction, constitute major foci for the photo-crosslinking reactions and their roles in the determination of the crosslinking topology of each system will be discussed at length in a later section.

Monomer $2_{crystal}$. Like **1**, monomer **2** crystallizes in the orthorhombic space group *Fddd* with one-half molecule of **2** in the asymmetric unit (Fig S38). Similarly, the melamine moieties provide a large number of H-bond donors and acceptors, allowing the formation of a 3D H-bonded network. A single monomer interacts with six surrounding molecules via a series of N-H ⋯N hydrogen bonds [N⋯N distances (Å): N(1) – N(8) 2.811(4), N(2) – N(5) 3.083(4), N(9) – N(3) 2.999(4), N(10) – N(7) 3.007(4), N(12) – N(4) 3.035(4)]. Similar to **1**, the monomers are arranged into stacked, interdigitated bilayers, with neighboring bilayers canted at roughly 60° to each other, which consequently produces a volume of void space between bilayers. The position of the C_{28} allyl group in the hexagonal channels of **1** is occupied by the C'_{27} ethyl group in **2**. Similarly, the C_{31} allyl groups that line the congested junction of **1** are replaced by the C'_{29} ethyl group in **2**. The installation of ethyl groups in the synthesis of **2** was aimed at a reduction of available crosslinking sites, which will be elaborated in the structural analysis of **P5-P8**.

H_COF-2. Crosslinking of C_{25}/S_1 and C_{28}/S_2 by EDT within the hexagonal channels proceeds via homo-ditopic connections (C_{25} to C_{25}*, C_{28} to C_{28}*). Each of the symmetry-equivalent pairs of atoms produces a link along the axis of one of the hexagonal channels (S_1 along [110], S_2 along [$1\bar{1}0$]). As a consequence of the relative positioning of the symmetry-equivalent pairs and the orientation of adjacent channels, the S_1 and S_2 crosslink chains lie entangled with one another (Figure S40). In considering potential topologies, these two crosslinks would result in a series of interwoven 2D polymer networks. Curiously, the crosslinks between C_{28} to C_{28}* do not attach monomers within the same bilayer, nor with a neighboring bilayer. Due to the heavy disorder and weak residual electron density, atomic positions for the crosslinkers residing within the congested junction, those bound to C_{22} and C_{31}, could not be modeled adequately. Discussion of the possible crosslinking products and the resulting framework topologies will be discussed in a later section.

H_COF-3. H_COF-3 exhibits homo-ditopic crosslinking by PDT. To accommodate the added size of the propylene dithiol, the S_1 crosslinker adopts an S-shape and attaches two symmetry equivalent sites C_{25} and C_{25}* on the same face of the bilayer, extending the structure along the *a*-axis. Like with H_COF-2, the crosslinking of C_{28}/S_1 within the hexagonal channels exhibits entanglement with a symmetry equivalent crosslinker in an adjacent channel. Similar to H_COF-2, the disorder and weak residual electron density involving C_{31} prohibited adequate modelling of the crosslinker beyond the terminal allyl carbon. In addition, the thermal ellipsoids for C_{20}, C_{21}, and C_{22} are much closer in magnitude to those of the C and N atoms of the TPE core, suggesting a higher degree of order than the first few atoms of the other crosslinking sites. Considering the lack of residual electron density in the vicinity of these three carbon atoms, it suggests that this allyl group remains unreacted through the course of the polymerization. This observation is further supported by the bond geometries of the three atoms (bond lengths and angles consistent with those expected of sp^2 carbons of allyl group) such that the X-ray

structure corroborates the monomer:crosslinker ratios determined from elemental analysis and solid-state NMR spectroscopy (Table S1 and Figure S66).

H_COF-4. Attempts to refine the structure of H_COF-4 were more strongly challenged by data quality than with H_COF-2 and H_COF-3. As a result, refined positions could be obtained only for the atoms corresponding to the starting material **1**. While the disorder of the terminal groups is more substantial than in $\mathbf{1}_{crystal}$, there is inadequate electron density to suitably model any fragment of the BDT crosslinkers. However, the magnitude of the thermal ellipsoids for the carbon atoms of one allyl group are comparable to those of the C and N atoms in the TPE core. As such, the limited motion and lack of disorder in these atoms may suggest that, as with H_COF-3, this allyl group (C_{22}) remains unreacted, which partially supports the sub-equimolar ratio of monomer to BDT determined via elemental analysis and solid-state NMR spectroscopy (Table S1 and Figure S67).

P5. Crosslinking of C'_{25}/S'_1 with EDT produced links along the walls of the hexagonal channels. The two monomer entities bound by this crosslinker comprise opposite faces of the same bilayer structure. As the resulting polymer extends along the *a*-axis, and as a result of the relative orientation of the two halves of the bilayer, the polymer takes on a helical shape (Fig S42). The broad helical pitch produced by the S'_1 crosslink also results in entanglement with neighboring polymer chains, producing an interwoven 2D sheet as a topological prototype. The congested junction appears unperturbed by the crosslinking reaction, and the central four allyl groups C'_{22} remain unmoved and unreacted.

P6. Similar to H_COF-3, homo-ditpopic crosslinking in **P6** is achieved by reaction of the C'_{25} allyl group with PDT. The C'_{25}/S'_1 crosslinker joins two monomer entities within the same face of the bilayer structure. Additionally, the crosslinker adopts an S-shaped conformation, similar to the PDT moiety in H_COF-3, and extends the polymer along the *a*-axis. This stands in contrast to the entangled crosslinkers observed in **P5**. While the entangled crosslinkers are seen in the EDT crosslinked structures, and even in H_COF-3, the presence of the S-shaped crosslinker in **P6** suggests that each crosslinking site may exhibit selectivity to certain crosslinkers.

P7. Similar to H_COF-4, the flexibility of the BDT crosslinker has likely resulted in a greater degree of atomic disorder and limited the extent to which an adequate model may be refined. The atomic positions of the TPE core have been refined anisotropically. However, the reacted-allyl and ethyl carbons exhibit more disorder than in any of the other structures. Unlike H_COF-4, the data suggest that carbon atoms at each of the four crosslinking sites are either disordered, experiencing a significant degree of thermal motion, or both, making it impossible to speculate which of the ally groups remain unreacted.

Table S3. Single crystal X-ray diffraction data of monomers $\mathbf{1}_{crystal}$ and $\mathbf{2}_{crystal}$

Compound	$\mathbf{1}_{crystal}$	$\mathbf{2}_{crystal}$
Formula weight	1149.40	1101.36
Color, habit	Yellow, Block	Yellow, Block
Temperature (K)	150.0	100.0
Crystal system	orthorhombic	orthorhombic
Space group	F d d d	F d d d
Unit cell dimensions *a* (Å) *b* (Å) *c* (Å) α β γ	 20.5062(13) 35.210(2) 42.652(4) 90 90 90	 20.6068(5) 35.0090(10) 42.3618(10) 90 90 90
Volume ($Å^3$)	30796(4)	30560.8(14)
Z	16	16
Calculated density (Mg/m^3)	0.992	0.957
Absorption coefficient (mm^{-1})	0.064	0.493
F (000)	9728	9344
Crystal size/mm^3	0.15 x 0.12 x 0.1	0.18 x 0.14 x 0.12
Radiation	MoKα (λ =0.70173)	CuKα (λ = 1.54178)
2θ Range for data collection (°)	4.408 to 49.998	5.396 to 150.15
Reflections collected	58859	43222
Independent reflections	6754	7826
Absorption correction	Empirical	Empirical
Data / restraints / parameters	6754 / 159 / 411	7826 / 140 / 412
Goodness-of-fit on F^2	1.061	1.333
Final R indices [I>2σ(I)]	R_1 = 0.092, wR_2 = 0.2571	R_1 = 0.0996, wR_2 = 0.3171
Final R indices [all data]	R_1 = 0.1067, wR_2 = 0.27809	R_1 = 0.1297, wR_2 = 0.3465
Largest diff. peak/hole ($e/Å^3$)	0.97/-0.48	0.63/-0.55
CCDC number	1908807	1908801

Table S4. Single crystal X-ray diffraction data of **P5**, **P6** and **P7**

Compound	**P5**	**P6**	**P7**
Color, habit	Yellow, Block	Yellow, Block	Yellow, Block
Temperature (K)	100	100	100
Crystal system	orthorhombic	orthorhombic	orthorhombic
Space group	F d d d	F d d d	F d d d
Unit cell dimensions			
a (Å)	19.6681(12)	19.99290(10)	20.1440(3)
b (Å)	34.306(2)	34.6322(2)	34.7052(4)
c (Å)	42.246(2)	42.3319(2)	42.3035(3)
α	90	90	90
β	90	90	90
γ	90	90	90
Volume ($Å^3$)	28505(3)	29310.5(3)	29574.4(6)
Z	16	16	16
Calculated density (Mg/m^3)	1.084	1.072	1.5436
F (000)	9888	9835	5824
Crystal size (mm^3)		0.1 x 0.05 x 0.05	
Radiation	MoKα (λ =0.70173)	Synchrotron (λ = 0.61992)	Synchrotron (λ = 0.61992)
2θ Range for data collection (°)	3.75 to 41.702	3.248 to 48.82	3.24 to 45
Reflections collected	59786	120665	95293
Independent reflections	3752	9072	7259
Absorption correction	Empirical	Empirical	Empirical
Data / restraints / parameters	3752/86/395	9072/406/444	7259/4/367
Goodness-of-fit on F^2	1.973	2.439	2.984
Final R indices [I>2σ(I)]	R1 = 0.1337, wR2 = 0.4033	R1 = 0.1673 wR2 = 0.4760	R1 = 0.1579, wR2 = 0.3979
Final R indices [all data]	R1 = 0.1428, wR2 = 0.4174	R1 = 0.1725, wR2 = 0.4904	R1 = 1663, wR2 = 0.4066
Largest diff. peak/hole ($e/Å^3$)	0.97/-0.68	1.42/-0.88	1.34/-0.50
CCDC number	1908804	1908803	1910292

Table S5. Single crystal X-ray diffraction data of H_COF-2, H_COF-3 and H_COF-4

Compound	H_COF-2	H_COF-3	H_COF-4
Color, habit	Yellow, Block	Yellow, Block	Yellow, Block
Temperature (K)	100	100	100
Crystal system	orthorhombic	orthorhombic	orthorhombic
Space group	F d d d	F d d d	F d d d
Unit cell dimensions			
a (Å)	21.0124(4)	20.2514(2)	20.8296(2)
b (Å)	35.3974(3)	35.0504(2)	35.3105(3)
c (Å)	42.5092(2)	42.5407(2)	42.4936(2)
α	90	90	90
β	90	90	90
γ	90	90	90
Volume (Å^3)	31617.7(7)	30196.2(4)	31254.2(4)
Z	32	32	20
Calculated density	1.100	1.172	1.300
F (000)	10880.0	11040.0	13000
Radiation	Synchrotron (λ = 0.61992)	Synchrotron (λ = 0.61992)	Synchrotron (λ = 0.61992)
2θ Range for data collection (°)	3.186 to 45	3.222 to 47.998	3.196 to 44.996
Reflections collected	102927	118202	96529
Independent reflections	7735	8915	7684
Absorption correction	Empirical	Empirical	Empirical
Data / restraints / parameters	7735/397/454	8915/470/473	7684/339/418
Goodness-of-fit on F^2	2.153	2.249	2.044
Final R 38ndices [I>2σ(I)]	R_1 = 0.1832, wR_2 = 0.4534	R_1 = 0.1677, wR_2 = 0.4472	R_1 = 0.1762, wR_2 = 0.4288
Final R 38ndices [all data]	R_1 = 0.1903, wR_2 = 0.4666	R_1 = 0.1724, wR_2 = 0.4599	R_1 = 0.1799, wR_2 = 0.4408
Largest diff. Peak/hole (e/Å^3)	1.38/-0.77	1.20/-0.88	1.23/-1.01
CCDC number	1908806	1908802	1908805

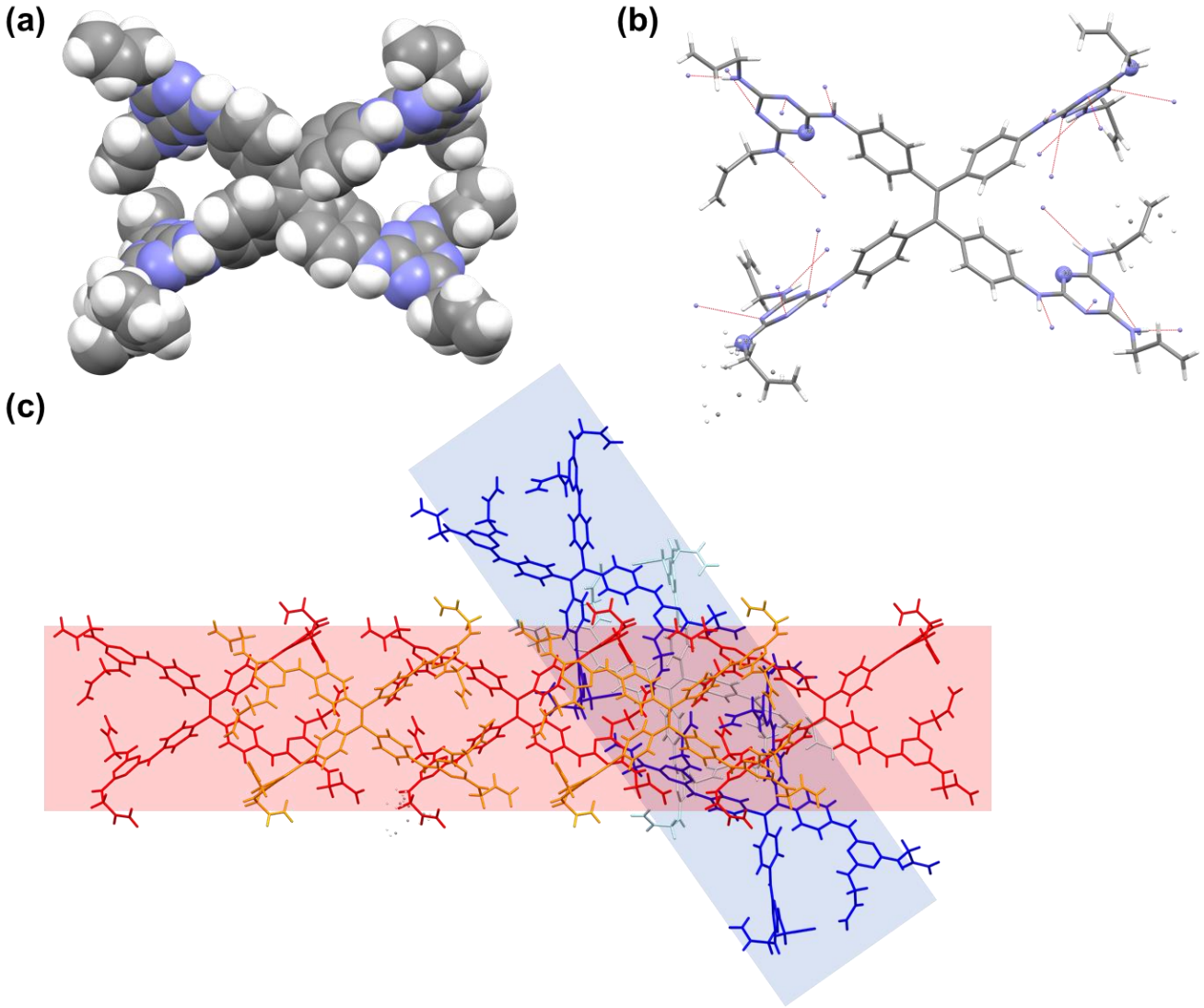

Figure S37. (a) Space-filled model of $\mathbf{1}_{crystal}$ in the solid state. (b) 20 N-H···N hydrogen bonding sites of $\mathbf{1}_{crystal}$, N_{11} and N_6 (highlighted in ball model) do not contribute to the hydrogen bonding network formation. (c) Alternating layers of monomers connected by hydrogen bonds in $\mathbf{1}_{crystal}$.

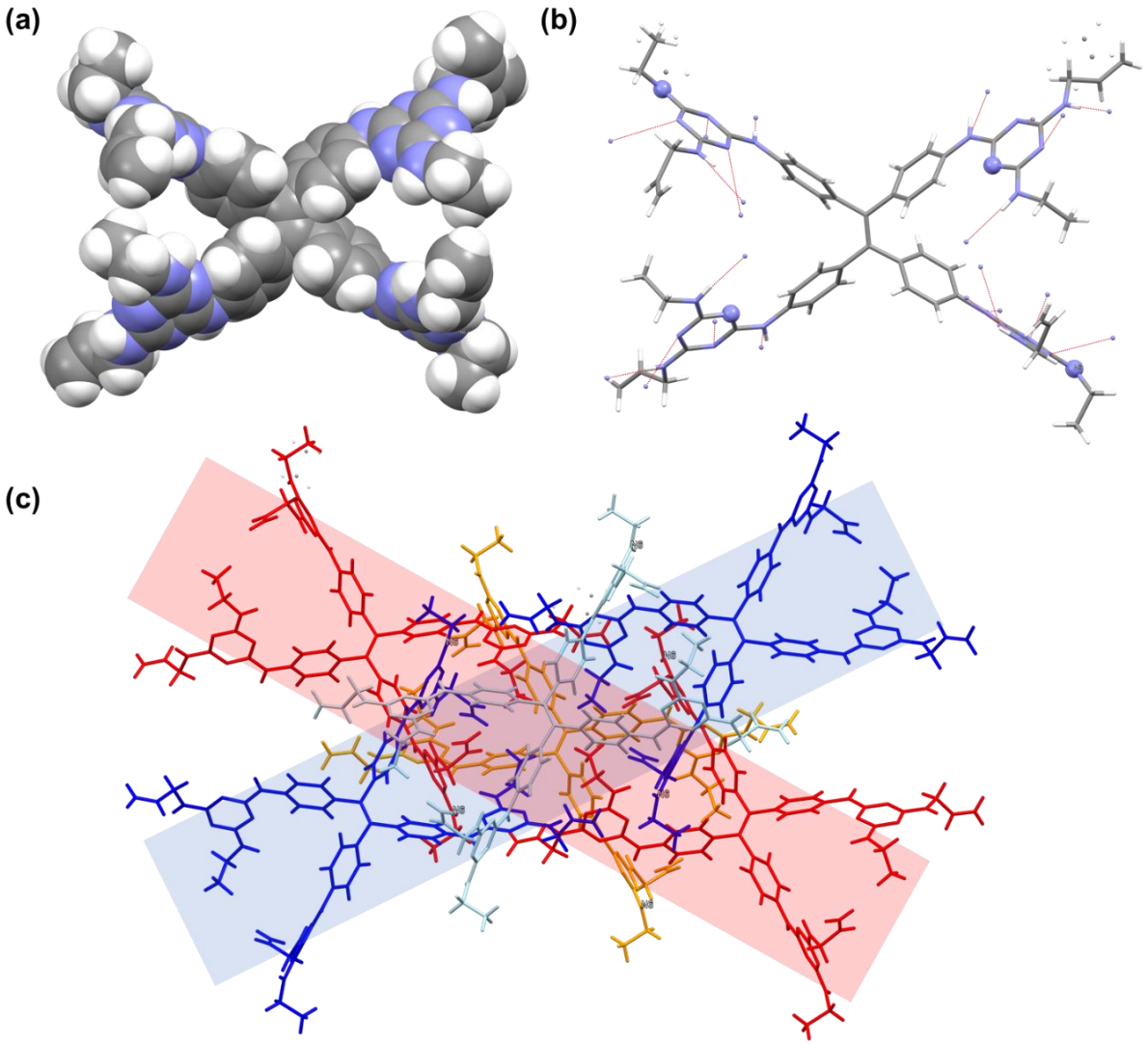

Figure S38. (a) Space-filled model of $\mathbf{2}_{crystal}$ in the solid state. (b) 20 N-H···N hydrogen bonding sites of $\mathbf{2}_{crystal}$, N_6 and N_{11} (highlighted in ball model) do not contribute to the hydrogen bonding network formation. (c) Alternating layers of monomers connected by hydrogen bonds in $\mathbf{2}_{crystal}$.

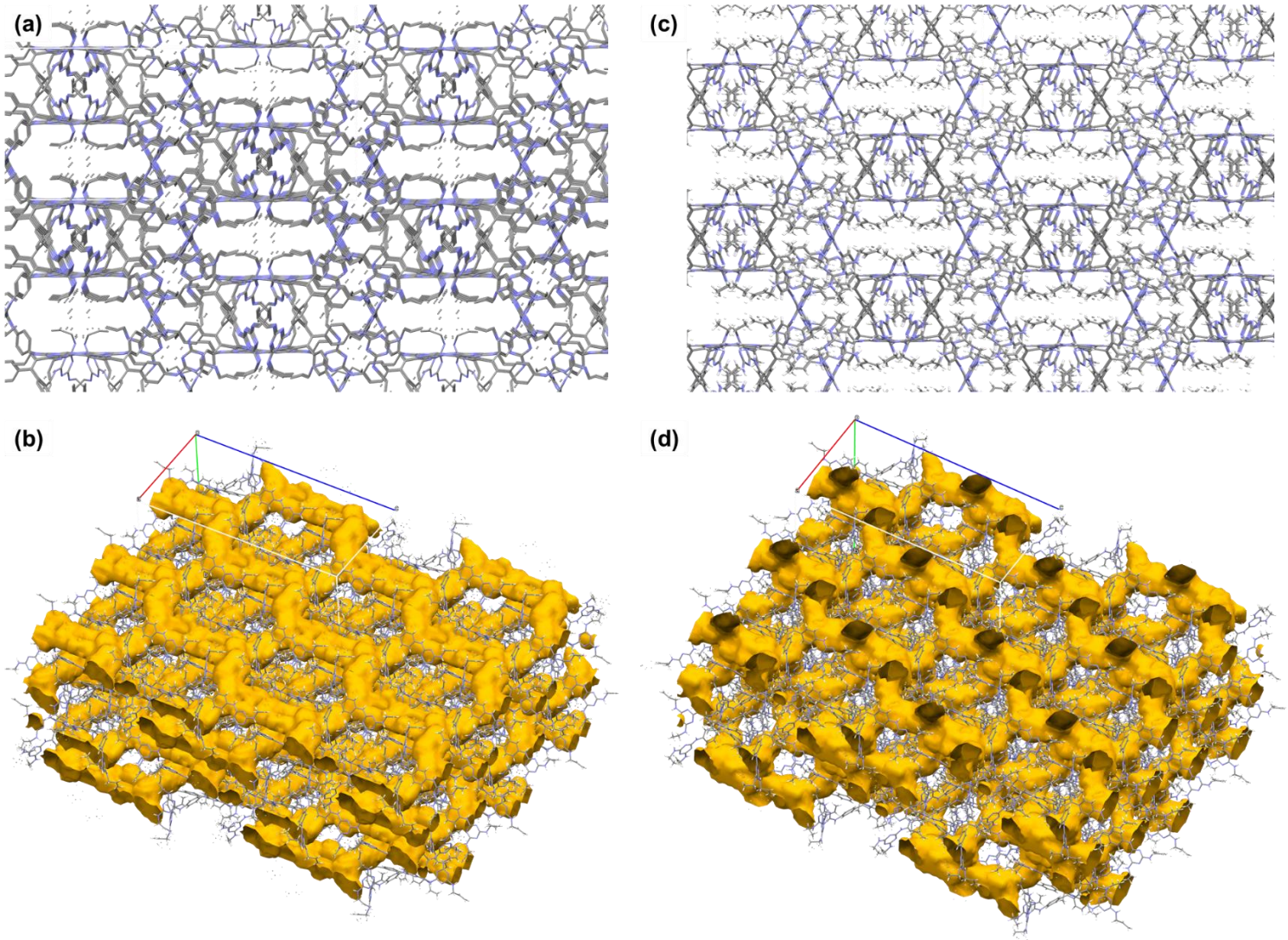

Figure S39. (a) Packing diagram of $\mathbf{1}_{crystal}$ along the [110] direction. (b) The highlighted pore surfaces of $\mathbf{1}_{crystal}$ with a calculated void space of 20 %. (c) Packing diagram of $\mathbf{2}_{crystal}$ along the [110] direction. (d) The highlighted pore surfaces of $\mathbf{2}_{crystal}$ with a calculated void space of 23 %.

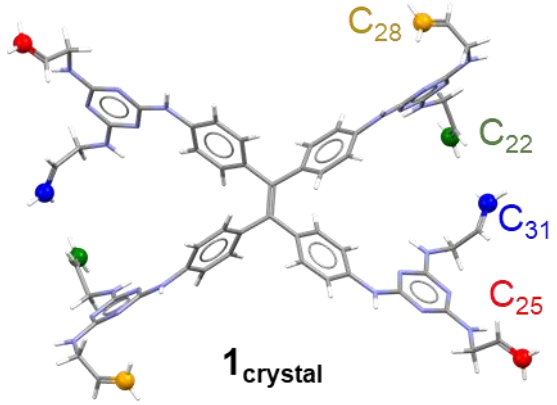

Table S6. Distances of the nearby alkene carbon atoms in the lattice of **1**$_{crystal}$.

Alkene carbon atom		Distance (Å)	Alkene carbon atom		Distance (Å)
C31B	C31B	3.330	C31A	C28A	8.188
C31A	C31A	3.468	C31B	C28B	8.197
C31A	C31B	3.644	C31B	C25	8.257
C31A	C22	3.689	C28C	C28A	8.296
C31B	C31B	3.728	C25	C31A	8.431
C31A	C31B	3.766	C28A	C28A	8.444
C28A	C28B	3.905	C31A	C22	8.455
C22	C22	3.975	C31A	C28B	8.468
C28C	C28B	4.054	C31B	C28A	8.491
C28C	C28C	4.170	C28A	C28B	8.505
C31B	C22	4.178	C25	C22	8.517
C31A	C31A	4.242	C28C	C28B	8.525
C31B	C31B	4.298	C25	C22	8.607
C28A	C28B	4.375	C25	C31B	8.611
C25	C28B	4.522	C25	C28C	8.639
C25	C28C	4.589	C31B	C28B	8.652
C31A	C31B	4.654	C31A	C28C	8.653
C25	C28A	4.788	C28C	C28B	8.741
C31A	C31A	5.050	C28B	C28B	8.746
C28C	C28B	5.166	C31A	C22	8.774
C28C	C28A	5.237	C28C	C28C	8.888

C31A	C22	5.570	C31B	C22	8.906
C25	C28A	5.702	C28B	C22	8.911
C28A	C28A	5.739	C25	C31A	8.916
C25	C31B	5.820	C25	C31A	8.937
C25	C28C	5.884	C28B	C22	8.939
C31B	C22	5.929	C31B	C28C	9.012
C25	C31A	5.930	C25	C28B	9.045
C28A	C28A	6.243	C31B	C22	9.054
C31B	C22	6.328	C28A	C22	9.090
C28C	C28A	6.408	C25	C31B	9.131
C25	C28C	6.566	C25	C28A	9.139
C25	C28A	6.792	C28C	C28B	9.253
C22	C22	6.897	C25	C25	9.282
C28C	C28C	6.906	C28C	C22	9.306
C31A	C22	6.915	C25	C22	9.372
C28C	C28B	6.985	C31A	C22	9.475
C25	C25	7.024	C25	C28B	9.477
C28A	C22	7.063	C25	C25	9.557
C28C	C22	7.346	C25	C25	9.609
C31A	C22	7.404	C22	C22	9.640
C28A	C28B	7.548	C28B	C22	9.702
C25	C22	7.551	C28B	C22	9.777
C31B	C22	7.794	C28A	C28B	9.783
C28A	C28A	7.844	C31B	C28C	9.833
C28C	C28C	8.025	C31B	C28A	9.853
C31B	C22	8.078	C31B	C28C	9.866
C28A	C28B	8.104	C25	C28C	9.902
C28C	C28A	8.150	C31A	C28A	9.926
C31A	C28B	8.168	C25	C28A	9.967
C25	C28A	8.175	C31A	C28C	9.971

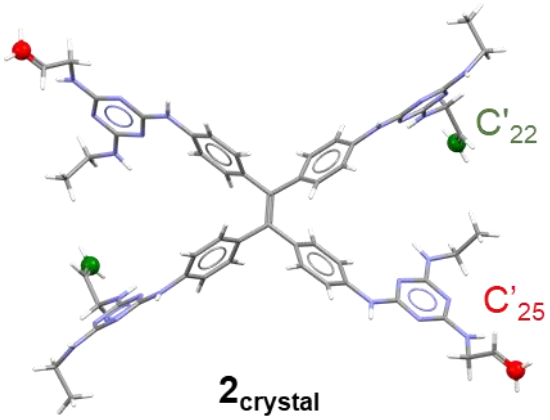

Table S7. Distances of the nearby alkene carbon atoms in the lattice of $\mathbf{2}_{crystal}$

Alkene carbon atom		Distance (Å)	Alkene carbon atom		Distance (Å)
C'22	C'22	3.650	C'25A	C'25A	9.401
C'25B	C'25B	5.882	C'25A	C'25A	9.545
C'25B	C'25B	6.481	C'22	C'25B	9.603
C'25A	C'25B	6.782	C'22	C'25B	9.746
C'25A	C'25A	6.840	C'22	C'22	9.911
C'22	C'22	7.042	C'25A	C'25A	10.085
C'25B	C'25B	7.163	C'22	C'22	10.201
C'22	C'25A	7.484	C'22	C'25A	10.285
C'25A	C'25B	7.767	C'22	C'25B	10.323
C'25B	C'25B	7.871	C'22	C'25A	10.506
C'22	C'25A	8.521	C'22	C'25A	11.323
C'22	C'25B	8.572	C'25A	C'25B	11.420
C'22	C'25A	8.681	C'22	C'25A	11.441
C'22	C'25B	8.760	C'25A	C'25A	11.664
C'25A	C'25B	8.889	C'22	C'22	11.703
C'22	C'25A	9.122	C'25B	C'25B	11.748
C'25B	C'22	9.232	C'22	C'25A	11.762
C'25A	C'25B	9.246	C'25A	C'25A	11.789
C'25A	C'25B	9.325	C'22	C'22	11.964

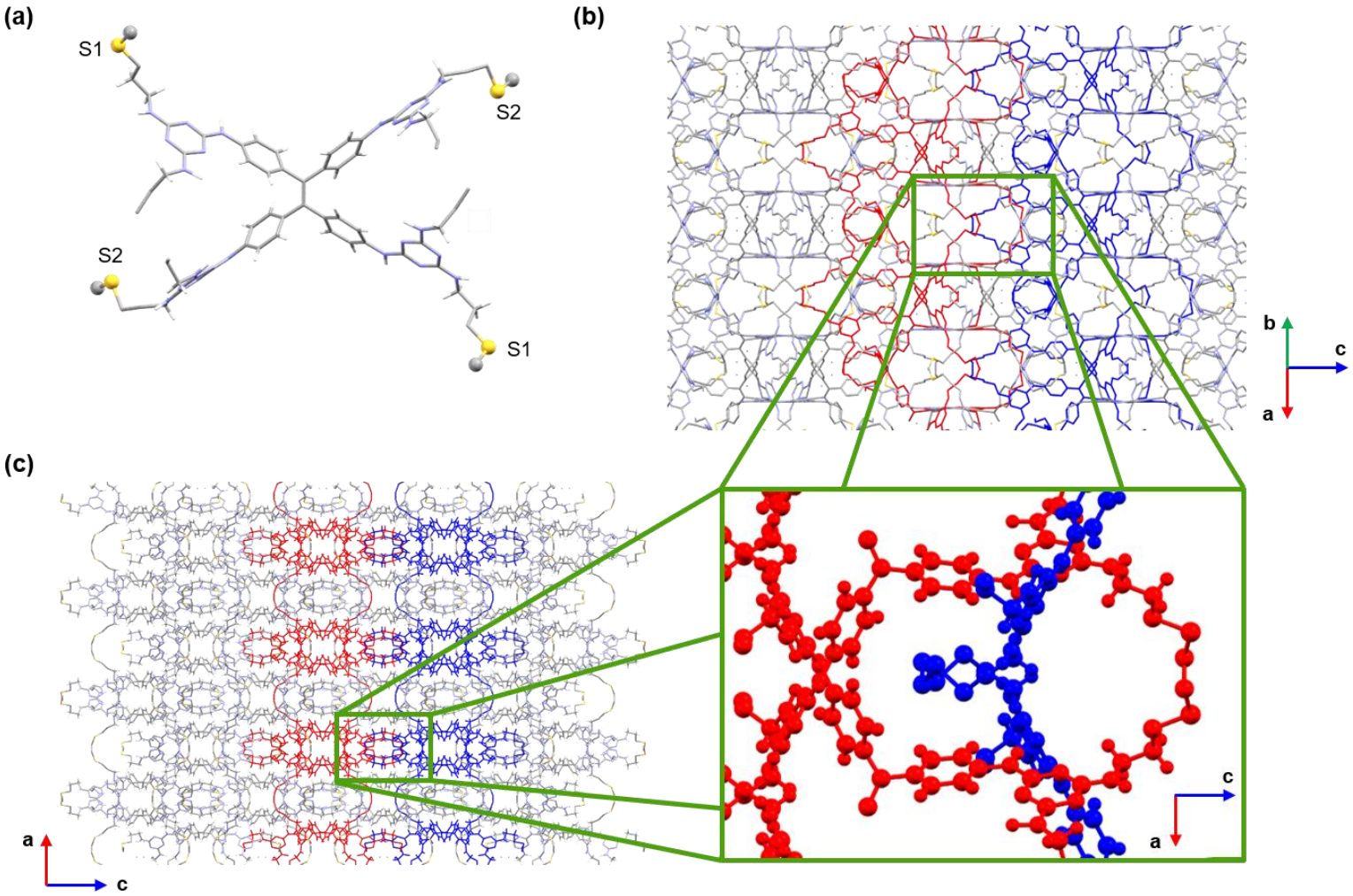

Figure S40. (a) Repeating unit of H_COF-2 network with crosslinking moieties highlighted in ball and stick model. (b) Extended packing of H_COF-2 viewed along the [110] direction with mechanically entangled networks highlighted in red and blue. (c) Alternate view of red and blue entangled networks showing crosslinking of alternating, in-phase bilayers, and (inset) close-up of interwoven dithioether moieties. For clarity, disordered atoms were omitted from (a) and hydrogen atoms were omitted from (b).

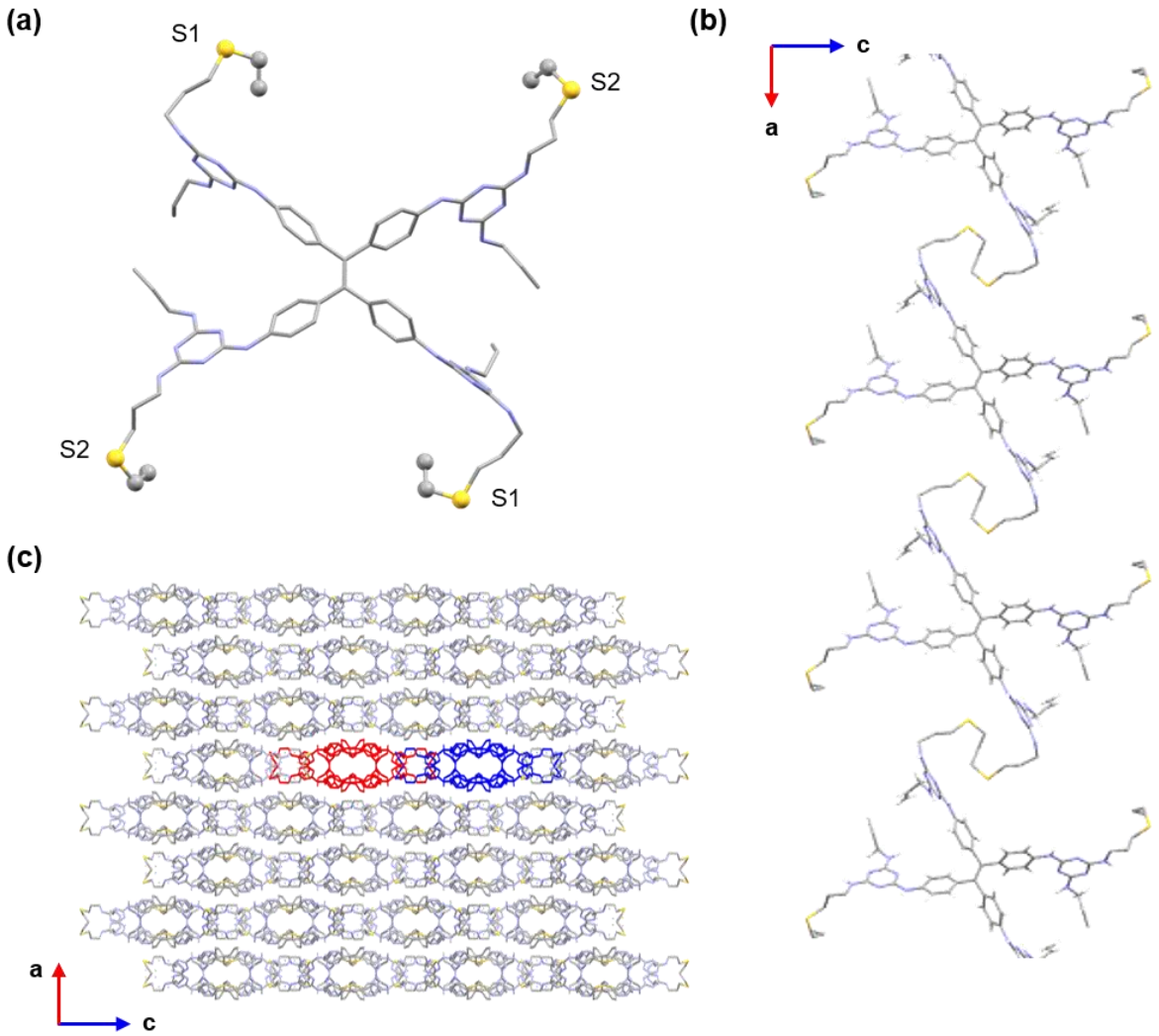

Figure S41. (a) Repeating unit of H_COF-3 network with crosslinking moieties highlighted in ball and stick model. (b) Expansion of polymer fragment showing S-shaped conformation of crosslinker. (c) Extended packing of H_COF-3 with mechanically entangled polymers highlighted in red and blue. For clarity, hydrogen atoms were omitted from (a) and (c).

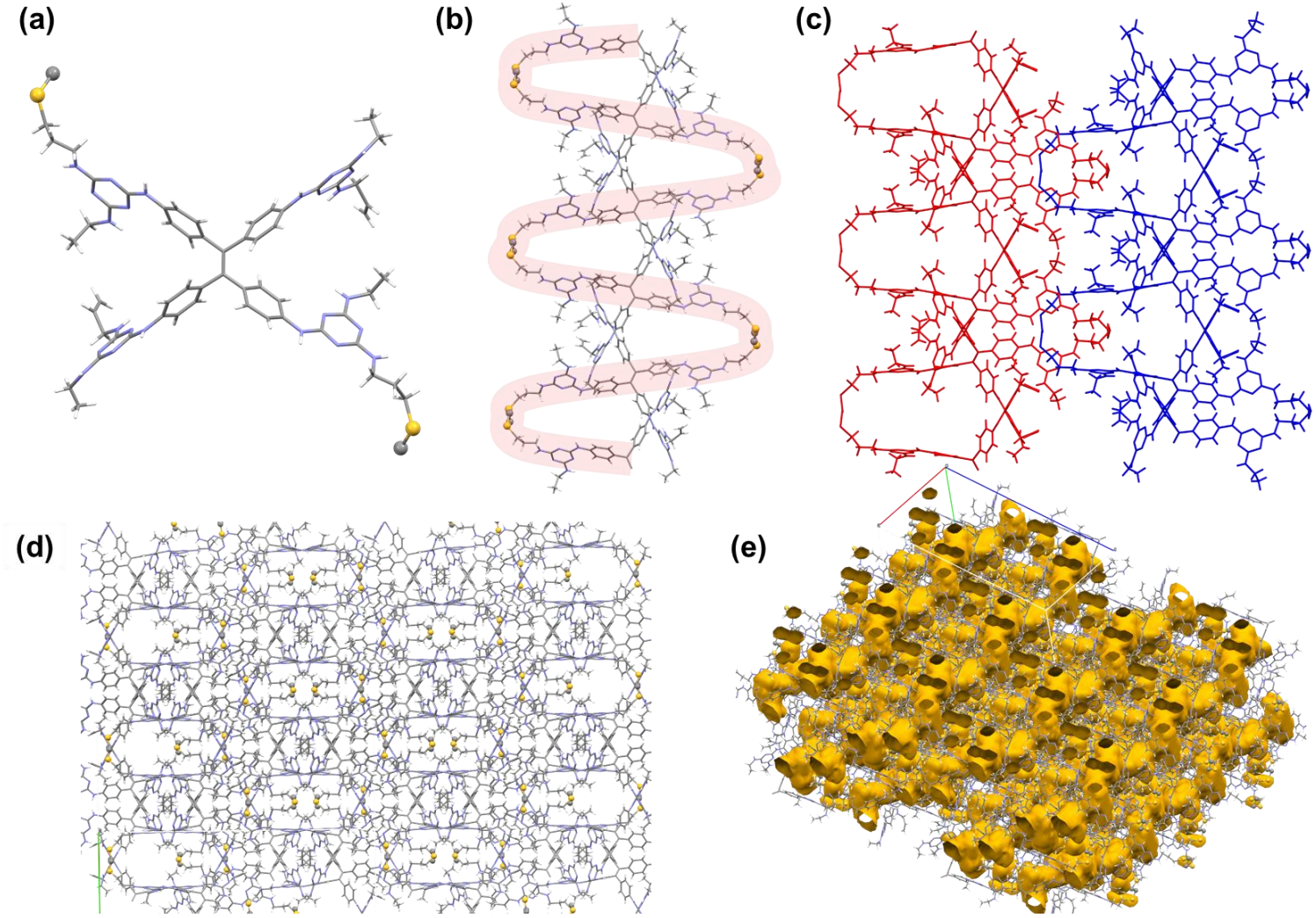

Figure S42. (a) Capped stick model of **P5** in the solid state with ethanedithioether linkage highlighted in ball and stick model. Hydrogen atoms of the linker in the solid-state were not modeled due to the co-existence of many conformations of the crosslinking motif. (b) S-shaped 1D polymer formed after photo-crosslinking. (c) Inter-woven structure of **P5**. (d) Packing diagram of **P5** along the [110] direction. (e) The highlighted pore surfaces of **P5**.

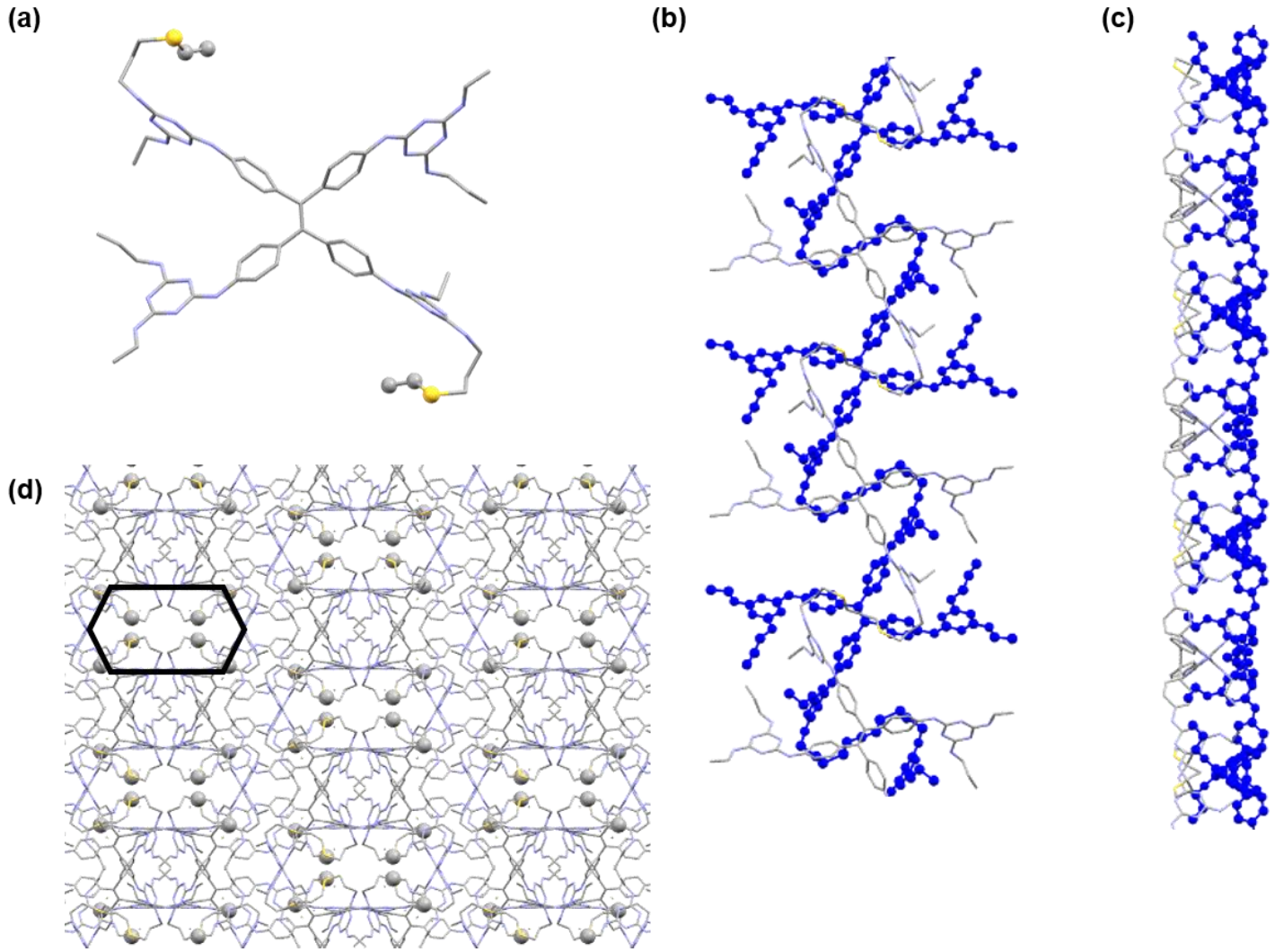

Figure S43. (a) Repeating unit of **P6** polymer with linking moieties highlighted in ball and stick model. (b) and (c) Perspectives of a stacked pair of polymer chains. Different from **P5**, the polymer chains of **P6** are not interwoven. (d) Extended packing of **P6** viewed along [110], a hexagonal channel is outlined in black and positions of C'_{27} ethyl group have been highlighted. Hydrogen atoms and disordered positions have been removed for clarity.

S6.1 Structural comparisons

Structural comparisons were performed based on the root mean square deviation (*rmsd*, equation 1) of atomic positions and were calculated using the Mercury software suite from the Cambridge Crystallographic Data Center (CCDC).

$$rmsd = \sqrt{\frac{1}{N}\sum_{i=1}^{N}\sigma_i^2} \qquad (1)$$

Two *rmsd* values were computed for comparison of each relevant pair of structures (*e.g.* **1** to H_COF-2, **2** to **P5**, **P5** to H_COF-2). First, the *rmsd* of the TPE-melamine core was determined for the atomic positions of all non-H atoms of the monomer excluding those of the allyl-amine moieties (Scheme S4a) and are summarized in the top right half of Table S8. Second, the *rmsd* of the melamine arms was calculated from the position of all non-H atoms in the melamine substituents (Scheme S4b) and are summarized in the lower left half of Table S8. All *rmsd* values are reported in Angstrom (Å).

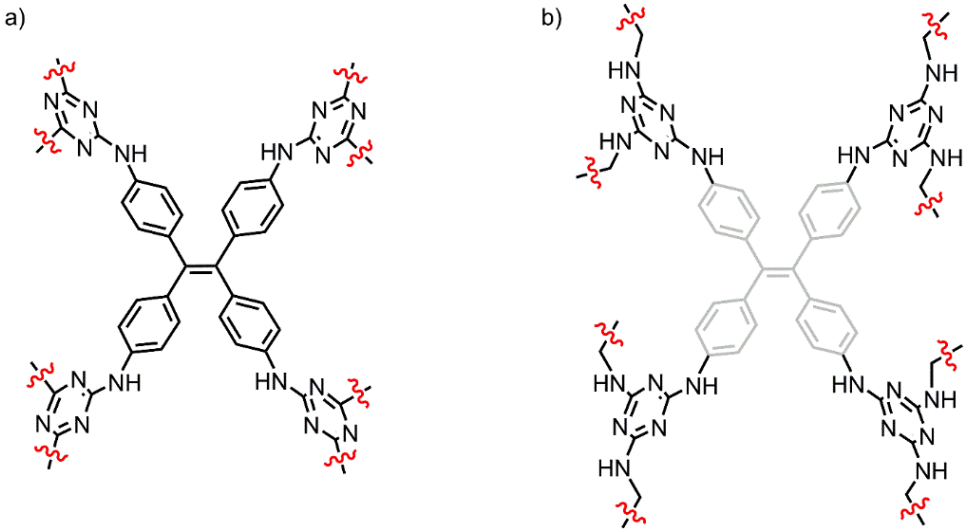

Scheme S4. Molecular components used for *rmsd* calculations of (a) TPE-melamine core (56 atoms) and (b) melamine arms (44 atoms).

Table S8. Calculated *rmsd* values for monomers, polymers, and H_COFs comparisons

	1	**2**	**P5**	**P6**	**P7**	H_COF-2	H_COF-3	H_COF-4
1		0.109				0.184	0.0825	0.074
2	0.0793		0.154	0.0992	0.0751			
P5		0.22				0.16		
P6		0.138					0.0446	
P7		0.109						0.104
H_COF-2	0.116		0.284					
H_COF-3	0.0819			0.0866				
H_COF-4	0.1				0.154			

S6.2 Crosslinking topology analysis

The presence of the ethyl substituents in the polymer systems removed half of the cross-linking sites compared to H_COFs. In each case, the asymmetric monomer **2** produced linear polymeric or oligomeric species when treated with dithiol and exposed to UV light. Analyses of the X-ray structures of the polymers and structural comparisons of the polymers with the corresponding H_COFs were able to confirm the accuracy of the crosslinking chains that were partially refined in the hexagonal pore areas of H_COFs, e.g. H_COF-2 with **P5**, etc. Coupled with the low *rmsd* values (Table S8), it follows that the remaining allyl groups, and the way in which they are or are not connected, would determine the crosslinking topology. However, it was impossible to determine the complete crosslinking topology of each of the H_COF structures solely based on the SCXRD analysis, since the data quality was too poor to provide definitive atomic positions for those sterically demanding areas (C_{31} and C_{22} allyl groups, Scheme S6). Based on the refined positions of the allyl carbon atoms C_{31} and C_{22}, a number of possible crosslinking topologies for both H_COF-2 and H_COF-3 can be hypothesized (Scheme S6). Combined with the experimental data, we can successfully eliminate the unlikely possibilities of the crosslinking topology (gray in Scheme S6), revealing the most reasonable crosslinking topology (red, Scheme S6) in the disordered areas. For the purpose of this discussion, each cross-linking site will be referenced solely by the label of its terminal carbon of sulfur atom. When multiple sites are designated with the same atom name, an asterisk (*) will be used to denote a symmetrically equivalent position.

Identifying the crosslinking topology of H_COF-2

H_COF-2. Local packing of the undetermined linking sites shows four different monomer units coming together in a tightly clustered junction, wherein eight crosslinking sites reside (Scheme S5). The four sites in the center of this area are symmetry-related C_{31}, while the remaining four are symmetry-related copies of C_{22}. When considering possible topologies, it simplifies the analysis to assume that the proposed cross-linking is uniform throughout the crystal. The reality of this assumption will be discussed as possible topologies are eliminated.

From the localization of the eight cross-linking sites and the estimated possible S-S distance of a single EDT crosslinker, it is impossible for a single dithiol molecule to crosslink between junctions as the distances are on the order of 8 Å or larger. Thus, should one thiol of an EDT react with an allyl group in this junction, the other thiol sulfur must crosslink to a site within the same junction or leave it unreacted. As a result, there are only seven possibilities for crosslinking in H_COF-2 (Scheme S5).

The comparison between H_COF-2 and the corresponding **P5** polymer provide accurate X-ray analysis of the crosslinking taking place between C_{25}/C'_{25} and C_{28}/C'_{28} allyl groups. In order to gain a clearer understanding of the crosslinking patterns of the eight alkenes (four C_{22} and four C_{31}) in the restricted cavities of $\mathbf{1}_{\mathbf{crystal}}$, which is a challenging task for the X-ray diffraction analysis alone due to the heavy disorder caused by crosslinker diffusion inside the crystals, we sought to experimentally eliminate the possible crosslinking topologies.

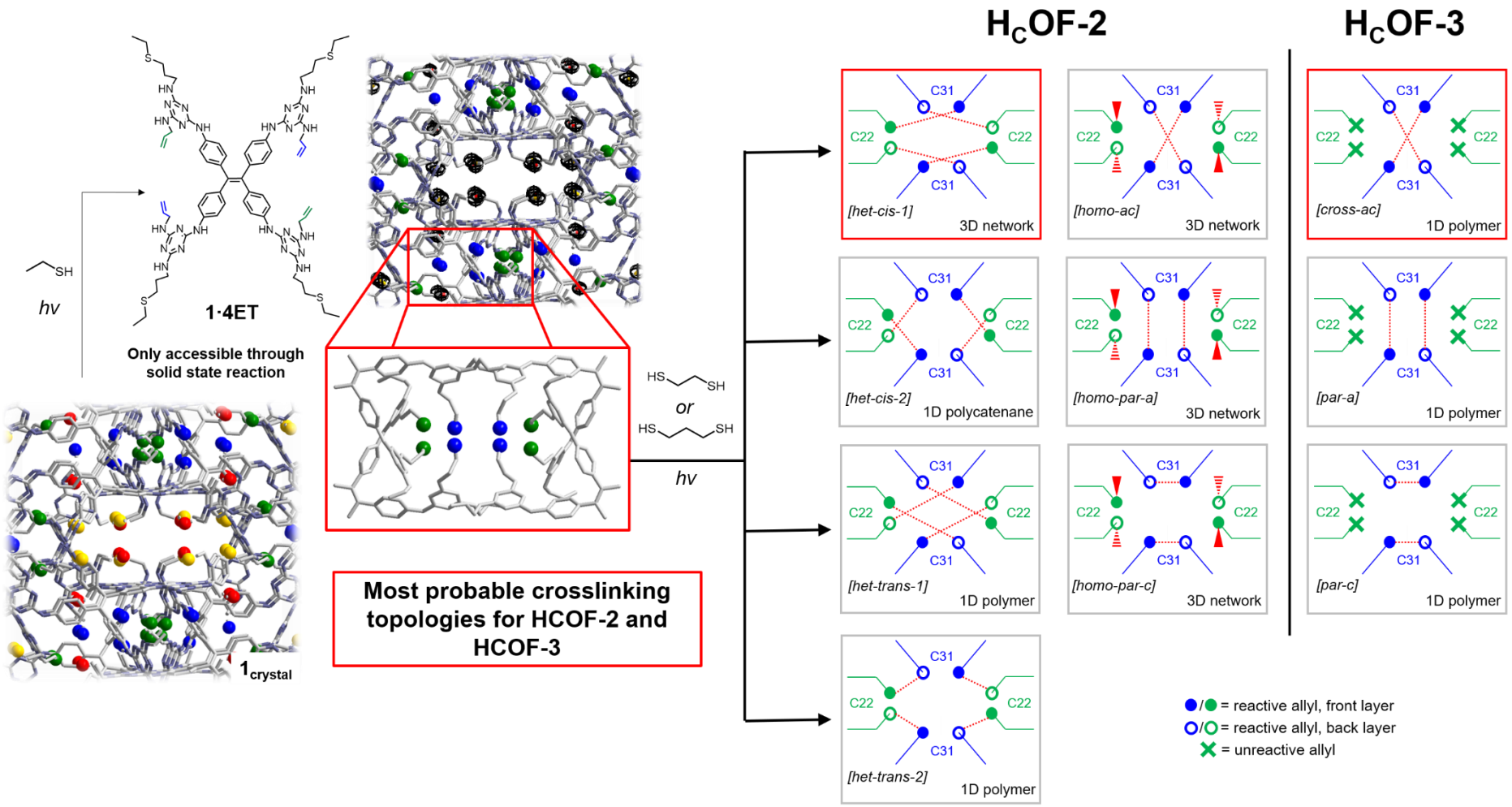

Scheme S5. Experimental design to reveal the EDT crosslinking between C_{22} and C_{31} allyl groups in $\mathbf{1}_{\mathbf{crystal}}$ by chemically blocking the C_{25} and C_{28} allyl groups through ET-substitution followed by EDT crosslinking. Expansions of the X-ray structure of H_COF-2 highlighting the congested C_{22}/C_{31} junction. ET-substituted alkenes are shown as black spheres, C_{31} sites as blue spheres, and C_{22} sites as green spheres. Also shown is a schematic representation of the possible crosslinking topologies to arise from the reaction of EDT in the junctions. C_{31} and C_{22} are presented as blue and green circles, respectively (filled = front layer, open = back layer), and proposed crosslinks are denoted in red.

In this design, we take advantage of the kinetic selectivity of the various alkene sites within the monomer crystals and ***selectively block the C_{25} and C_{28} allyl groups using ET***. In this series of experiments (Table S2, entry 3-8), the four alkenes in $\mathbf{1}_{\mathbf{crystal}}$ exposed in the accessible channels (C_{25} and C_{28}) were substituted by ET in order to prevent crosslinking at these sites. Then, the crystals were introduced to dithiol crosslinkers (EDT and PDT) to react with the remaining four alkenes in the congested areas (C_{22} and C_{31}), and the products were characterized after photoirradiation. In this way, we will elucidate the remaining features of the crosslinking topologies in the highly crosslinked frameworks of H_COF-2 and H_COF-3.

[1·(3-4)ET**]$_{\mathbf{crystal}}$** with EDT

[1·(3-4)ET**]$_{\mathbf{crystal}}$.** Mother solution of $\mathbf{1}_{\text{crystal}}$ was removed before MeCN was used to wash the surface of crystal samples. Fresh MeCN (2 mL) was added to the crystal samples before ET was added. The sample was kept in the dark for 24 h to allow an extensive thiol diffusion into the crystal samples. Another portion of ET were introduced subsequently after 24 h. The glass vial was then irradiated under UV light (medium-pressure 175-watt Hg lamp) with forced air cooling. The **ET**-substitution process was monitored by ^{1}H NMR spectroscopy to ensure that approximately four of the eight alkenes in monomer $\mathbf{1}_{\mathbf{crystal}}$ had reacted with ET. The crystal samples were collected after photoirradiation and washed with an excess of MeCN and acetone to remove unreacted ET. The crystal samples were dried under vacuum and dissolved in DMSO-d_6 for NMR analysis. The ^{1}H NMR spectrum (Figure S29) suggests approximately four allyl groups have been substituted by ET. The mass spectrum (Figure S45a) suggests that the product is a mixture composed of mostly **[1·**(3-4)ET**]**.

[1·(3-4)ET**]$_{\mathbf{crystal}}$** with EDT. In order to reveal the crosslinking topology between C_{22} and C_{31} allyl groups, crystal samples of **[1·**(3-4)ET**]$_{\mathbf{crystal}}$** were placed in a glass vial with 2 mL neat EDT, and the vial was kept in the dark for 24 h to allow extensive diffusion of the EDT followed by 120 h UV irradiation (medium-pressure 175-watt Hg lamp). After photo-irradiation, the crystal samples were collected and washed with an excess of acetone to remove any unreacted dithiols. These crystals were dried under reduced pressure and dissolved in DMSO-d_6 for MS and NMR analysis.

In the NMR sample, a majority of the crystals (> 90 wt %) are dissolved in DMSO-d_6 with a small amount of undissolved species. The soluble sample was also characterized by mass spectrometry and DLS. As shown in Figure S44a, two out of the four remaining allyl groups have been consumed by EDT. Surprisingly, no oligomeric or polymeric species were detected in the DLS analysis. In the high-resolution mass spectrum (Figure S46), monomeric species were identified. These results suggest that only one thiol of the EDT participated in the thiol-ene reaction, leaving the other thiol unreacted in the crystal lattice. To confirm this hypothesis, we washed these EDT-reacted crystal samples extensively using acetone, and further irradiated these washed crystals for another 60 h. The quantity of undissolved solids increased rapidly and only a small fraction of the crystal samples can be dissolved in DMSO-d_6. As presented in the NMR spectrum (Figure S44b), the integration ratio of the allyl group to the TPE core is increased in the soluble product after the additional 60 h irradiation. This result suggests that most of the monomeric species observed after initial 120 h EDT reaction have been polymerized into insoluble polymers, leaving only unreacted **[1·**(3-4)ET**]** monomers or uncrosslinked species in the solution.

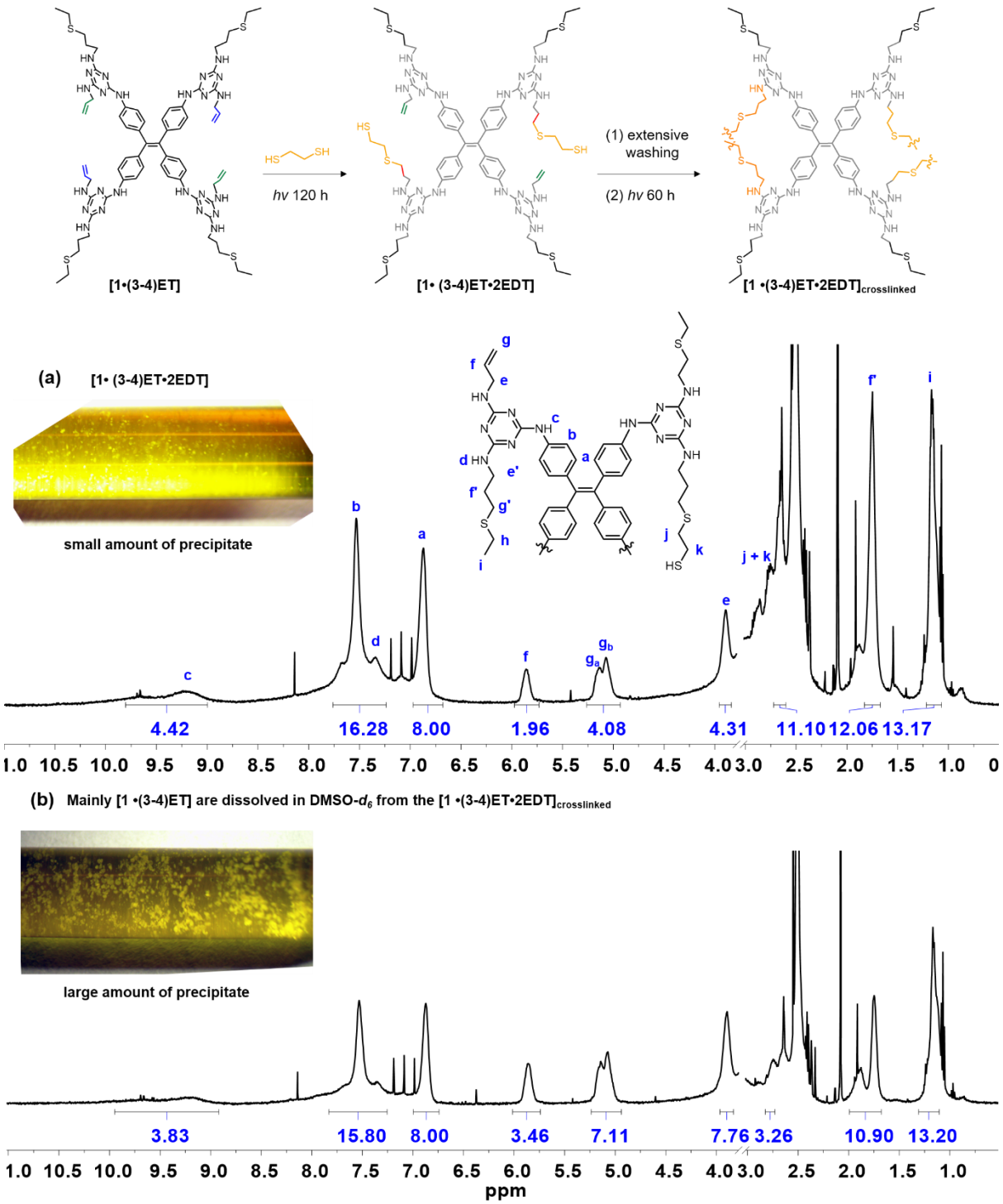

Figure S44. ^{1}H NMR spectra (298 K, 500 MHz, DMSO-d_6) of ET-substituted crystal samples **[1**·(3-4)ET**]** immersed in 2 mL neat EDT and UV for 120 h (a) and then then another 60 h of UV in blank acetone with EDT removed (b). In Figure S44b, the dissolved species demonstrated an increased alkene proton integration (~3.5), compared with the sample (~2.0) in Figure S44a. This observation suggests that, after most of the monomers were converted to insoluble polymer, the soluble fraction is composed of unreacted **[1**·(3-4)ET**]** monomers or uncrosslinked species in the solution.

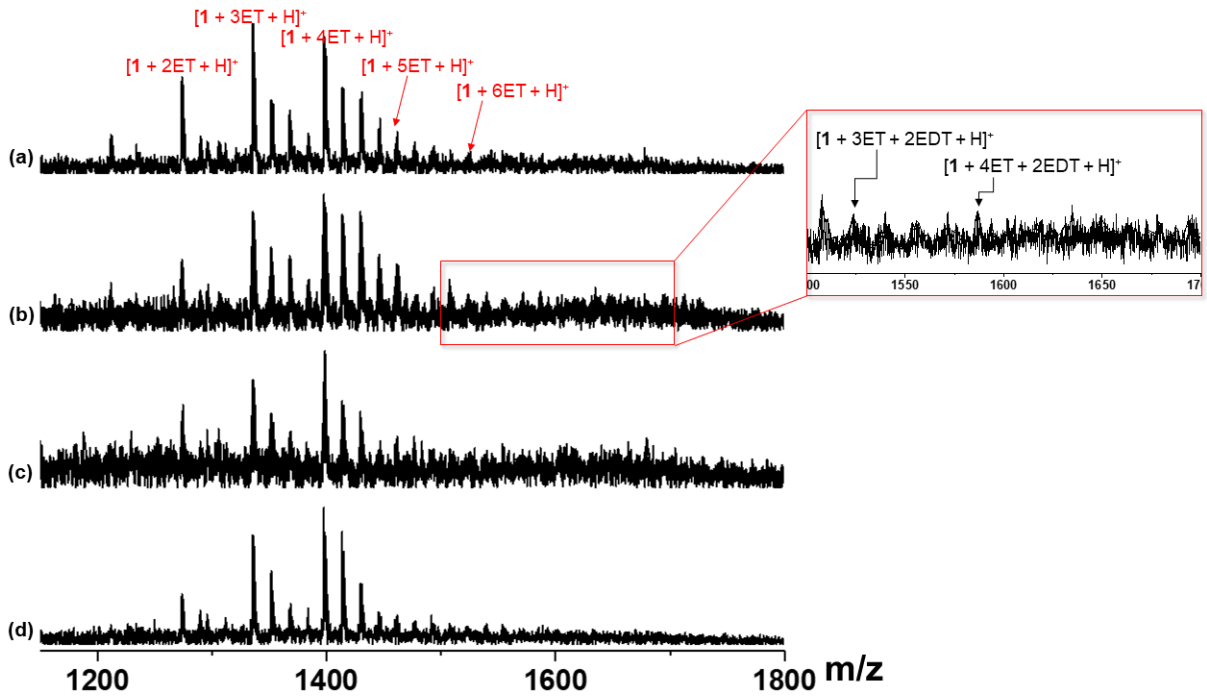

Figure S45. (a) ESI mass spectrum of the ET-substituted crystal samples, presents **1**•2ET (*m/z* = 1272.64), **1**•3ET (*m/z* = 1334.66), **1**•4ET (*m/z* = 1396.68), **1**•5ET (*m/z* = 1458.70), **1**•6ET (*m/z* = 1520.72), and **1**•7ET (*m/z* = 1582.74). The consistent occurrence of *m/z* = [M + 16n] (n = 1, 2) in the spectrum can be ascribed to sulfoxide derivatives, which are the oxidation products of those thioethers. The obtained crystal samples were immersed in 2 mL neat EDT and irradiated under UV lamp for (b) 60 h, and (c) 120 h. The crystal samples were dissolved in DMSO, and a small amount of insoluble residues was removed using syringe filters. These samples were injected for ESI-MS analysis. (d) Crystal samples of (c) were washed extensively using acetone to remove any unreacted EDT. These washed crystal samples were re-subjected to UV irradiation in acetone for another 60 h. Majority of the crystal samples became insoluble in DMSO, and the mass spectrum (d) of the filtrate is listed here for comparison.

After a second UV irradiation, existence of EDT-substituted molecular species can be observed at (b) and (c), which decrease after extra 60 h blank irradiation, suggesting the existence of EDT substituted in (b) and (c), which, with prolonged exposure to UV, were able to react with free alkene to crosslink more monomers, leading to the disappearance of these species in (d).

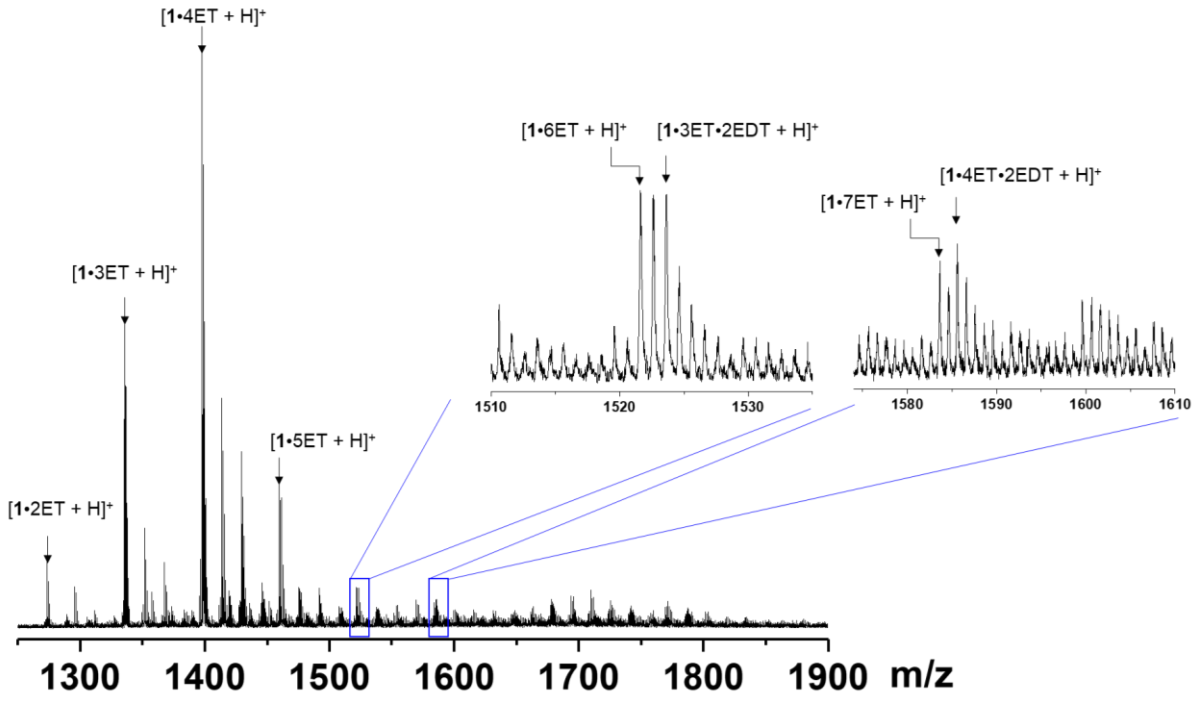

Figure S46. High resolution ESI-MS of the dissolved samples of the **[1**·(3-4)ET**]** crystals after being irradiated in neat EDT for 60 h. The consistent occurrence of *m/z* = [M+16n] (n = 1, 2) in the spectrum can be ascribed to sulfoxide derivatives, which are the oxidation products of those thioethers. Besides the ET-substituted species, EDT-substituted species are observed, confirming the existence of monomeric with EDT substitution.

Identifying the crosslinking topology of H_COF-2

The SCXRD analysis demonstrated in Scheme S5 suggested seven possible crosslinking between C_{22} and C_{31}. These possibilities are discussed individually as below:

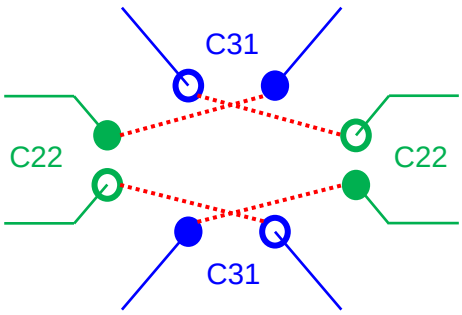

Possibility 1. [het-cis-1] The first possibility for heterotopic crosslinking takes place between C_{31} and C_{22} [C···C separation (Å): 5.826/7.144] in a cisoid orientation. These crosslinks would propagate within the bilayer structure along the *c*-axis. Taken with the C_{28}/S_1 and C_{25}/S_2 crosslinks from the X-ray data, the full structure would comprise a formal 3D framework with one degree of interpenetration.

Such a framework topology is consistent with our observation of the step-wise formation of large quantities of insoluble material in the reaction of **[1**·(3-4)ET**]**$_{crystal}$ with EDT. Firstly, the dithiols react with the C_{31} allyl groups, affording monomeric species that are soluble in the NMR (Figure S44) and MS analysis (Figure S45b-c, S46). The subsequent photocrosslinking after removing the excess of EDT rapidly increased the crosslinking density to afford insoluble crystalline materials, leaving little unreacted primarily monomeric species in solution (Figure S45d). Thus, this topology cannot be rejected on the bases of experimental observations and **must be considered as a candidate for the true topology of H_COF-2**.

Possibility 2. *[het-cis-2]* The second possibility of a heterotopic crosslinking may take place between C_{31} and C_{22} [C···C separation (Å): 3.677/5.501] in a cisoid orientation, which produces a theoretical topology of a self-catenated 1D polymer resulting from an intramolecular cyclization between C_{31} and C_{22}. When **[1·**(3-4)ET**]** was employed for EDT crosslinking, a 1D polycatenane would be produced in theory, which is inconsistent with our experimental observation in the reaction of **[1·**(3-4)ET**]**$_{crystal}$ with EDT (Figures S44-46). As we observed in the experiment, neither macrocycle nor polycatenane was identified in the MS or DLS analysis. Furthermore, this crosslinking topology could not explain our experimental observation of the stepwise formation of a large amount of insoluble material. Therefore, we can eliminate this possibility.

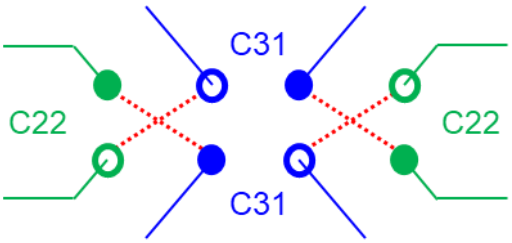

Possibility 3 and 4. *[het-trans-1]* and *[het-trans-2]* The third and fourth possibilities for heterotopic crosslinking take place between trans-oriented C_{31} and C_{22} for *[het-trans-1]* [C···C separation (Å): 7.784/8.535] and *[het-trans-2]* [C···C separation (Å): 5.686/6.317], respectively. While both topologies would result in the formation of formal 2D networks for H_COF-2, in the reaction of **[1·**(3-4)ET**]**$_{crystal}$ with EDT, either crosslinking mode would result in large quantities of 1D polymer chains. As with [*het-cis-2*], no evidence of 1D polymeric products were observed by MS or DLS analysis, and such polymer formation would not clarify the formation of insoluble products in **[1·**(3-4)ET**]**$_{crystal}$ crosslinking experiments. Therefore, we can conclude, based on experimental evidence, that *[het-trans-1]* and *[het-trans-2]* can be eliminated as possible candidates for the topology of H_COF-2.

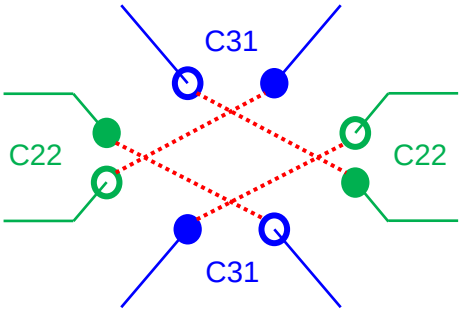

[het-trans-1]

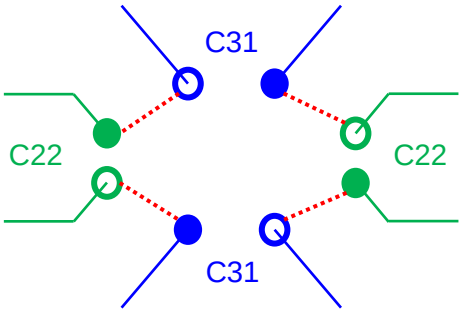

[het-trans-2]

Possibility 5. *[homo-par-a]* The first possible topology by homotopic crosslinking of can be generated from *trans*-facial linking of C_{31} atoms parallel to the *a*-axis [C···C *separation* (Å): 3.125/3.802/4.402] and C_{22} atoms parallel to the *b*-axis [C···C separation (Å): 3.688]. In H_COF-2, this would result in a 3D crosslinked framework. However, when C_{25} and C_{28} crosslinking sites are blocked by ET, as in **[1·**(3-4)ET**]**$_{crystal}$, the *[homo-par-a]* crosslinking mode would result in an extended 2D network, which is inconsistent with our experimental observation of the formation of monomeric species in the first step EDT reaction.

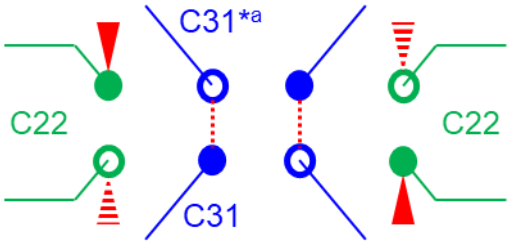

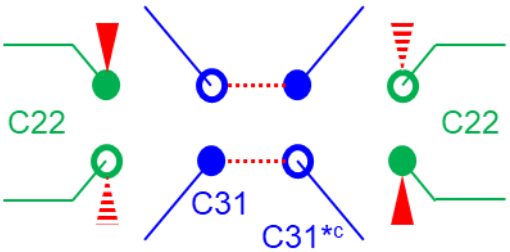

Possibility 6. [homo-par-c] The second possible homotopic crosslinking of H_COF-2 develops similarly to the first. As there is only one pair of C_{22} atoms positioned at a suitable distance for homotopic crosslinking, the crosslink at C_{22} [C···C separation (Å): 3.688] must extend along the *b*-axis, as described above. Linking of C_{31} and C_{31}^{*c} [C···C separation (Å): 3.015/4.175/5.063] must then occur *trans*-facially and would provide extension of the molecular framework along the *c*-axis, granting a higher degree of dimensionality and producing a 3D framework in H_COF-2. However, similar to *[homo-par-a]*, an extended 2D network would be produced in the case of **[1**·(3-4)ET**]**$_{\textbf{crystal}}$ reacting with neat EDT.

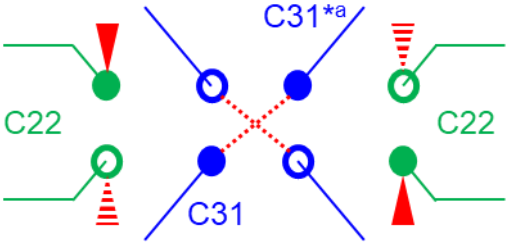

Possibility 7. [homo-ac] The last possible topology hypothesized for H_COF-2 arises from crosslinking of C_{31} along the ac-plane. Similar to the [*homo-par-a*] and [*homo-par-c*] topologies, C_{22} must crosslink along the *b*-axis. A crosslink formed between C_{31} and C_{31}^{*ac} [C···C separation (Å): 3.336/3.669] will produce a 3D framework in H_COF-2. In the crosslinking of **[1**·(3-4)ET**]**$_{\textbf{crystal}}$ by EDT, the *[homo-ac]* topology would, as with *[homo-par-a]* and *[homo-par-c]*, produce an extended 2D network.

While *possibilities 5*, *6*, and *7* all suggest the formation of a 3D framework in H_COF-2, the three hypothetical topologies do not adequately explain the kinetic aspects of the reaction of **[1**·(3-4)ET**]**$_{\textbf{crystal}}$ with EDT. Following treatment of **[1**·(3-4)ET**]**$_{\textbf{crystal}}$ with neat EDT and exposure to UV radiation, MS and DLS data suggest the formation of predominantly monomeric species. The formation of largely insoluble products is not observed until after the irradiated crystals are washed to remove excess EDT and irradiated again. Based on our kinetic studies of allyl accessibility, we believe the C_{22} allyl groups to be the least accessible of all crosslinking sites in monomer **1**. As such, it is expected that exposure to neat EDT and UV light would result in saturation of available C_{31} sites prior to reaction of the C_{22} allyl groups. The presence of the half-reacted dithiols in the junction would exacerbate the already sterically hindered environment of C_{22} and further prohibit reaction of the C_{22} allyl group and result in primarily soluble, monomeric products. Once the excess neat EDT is removed, extended exposure to UV light could only result in polymerization, and subsequent precipitation of highly crosslinked particles, as mostly C_{22} allyl groups would be available to react with the hanging, unreacted thiols. **This observed step-wise process strongly favors the formation of *heterotopic* crosslinks and cannot be reconciled with the homotopic crosslinking topologies described above, effectively eliminating all homotopically crosslinked topologies as candidates for the final H_COF-2 structure.**

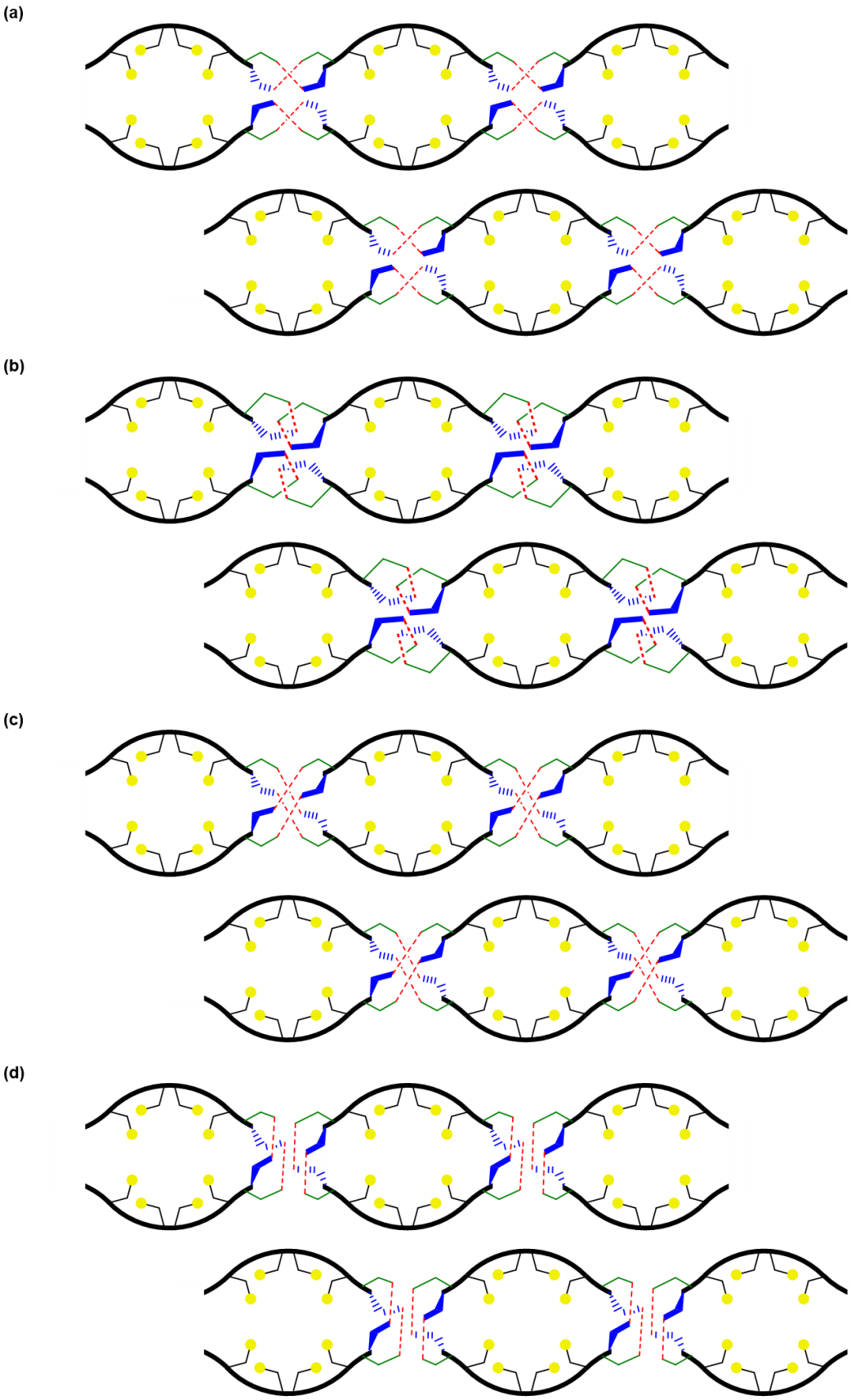

Scheme S6. Schematic representation of hypothetical topologies formed from heterotopic crosslinking of **[1**·(3-4)ET**]**$_{\textbf{crystal}}$ by EDT. (a) 2D network topology expected from *[het-cis-1]* crosslinking mode, (b) 1D polycatenane expected from *[het-cis-2]* crosslinking mode, (c) 1D polymer expected from *[het-trans-1]* crosslinking mode, and (d) 1D polymer expected from *[het-trans-2]* crosslinking mode.

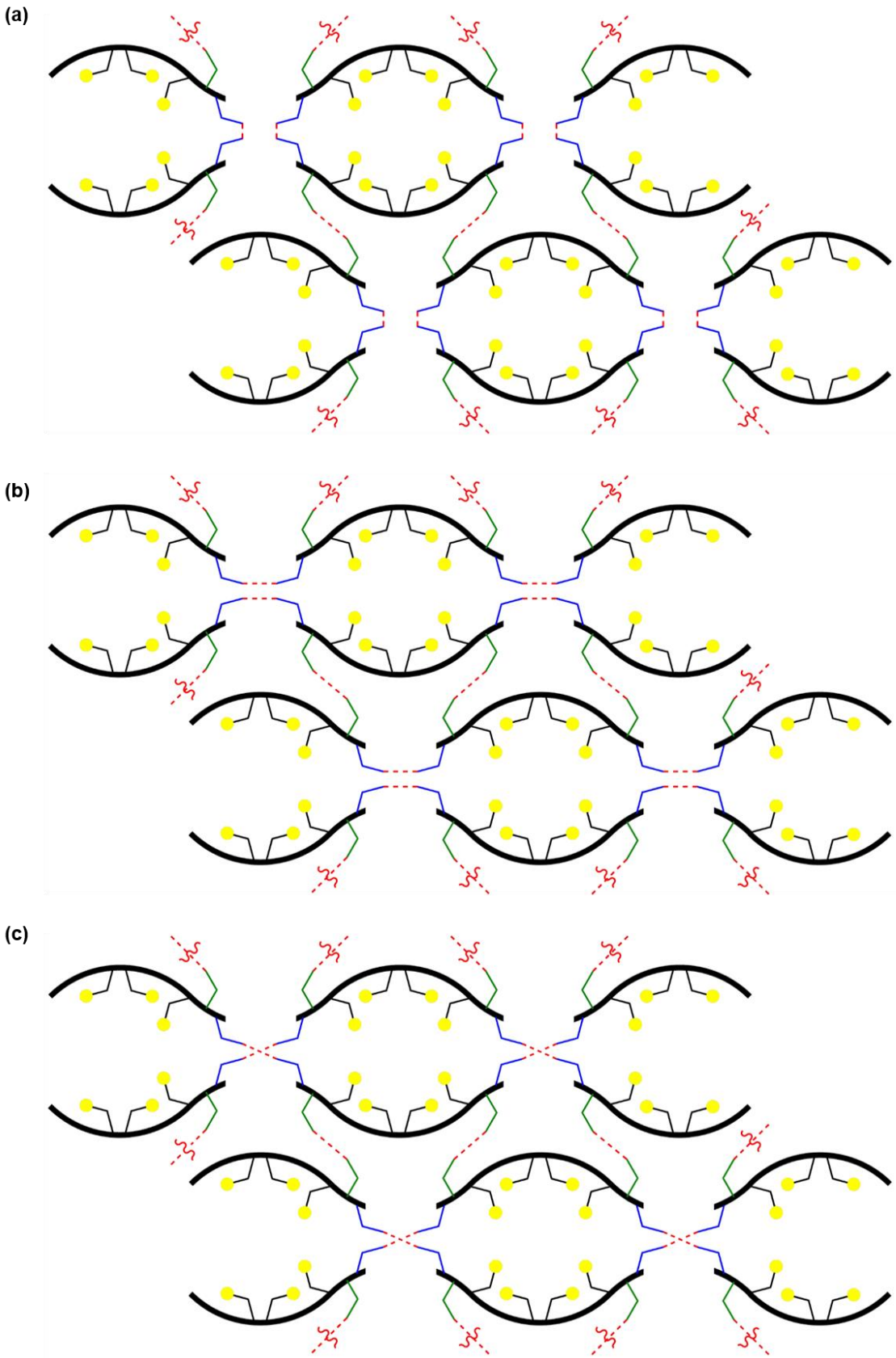

Scheme S7. Schematic representation of hypothetical topologies formed from homotopic crosslinking of **[1**·(3-4)ET**]**$_{crystal}$ by EDT. (a) 2D network topology expected from *[homo-par-a]* crosslinking mode, (b) 2D network topology expected from *[homo-par-c]* crosslinking mode, and (c) 2D network topology expected from *[homo-ac]* crosslinking mode.

Identifying the crosslinking topology of H_COF-3

Since we can conclude that the C_{22} allyl group is unreacted in H_COF-3, the possible topologies of H_COF-3 must be determined by the homotopic crosslinking of C_{31}.

[1·(3-4)ET**]$_{crystal}$** with PDT. Similar to the reaction with EDT, crystal samples of **[1**·(3-4)ET**]$_{crystal}$** were placed in a glass vial with 2 mL neat PDT and the vial was kept in the dark for 24 h to allow extensive diffusion of the PDT followed by 120 h UV irradiation. After photo-irradiation, the crystal samples were collected and washed with an excess of acetone to remove any unreacted dithiols. The crystals were dried under reduced pressure and dissolved in DMSO-d_6 for NMR, MS, and DLS analysis (no insoluble residual was identified). As shown in Figure S47, a little less than two of the four remaining allyl groups have been consumed. In contrast to the case of EDT reaction, the integration of proton *f'+l'* in the ^{1}H NMR spectrum suggests both thiol groups of the PDT were reacted with allyl groups. This result is consistent with our observation in the DLS analysis (Figure S48), in which the polymeric species with solvodynamic radius ~ 100 nm were observed. Therefore, linear polymeric chains were formed between the two C_{31} allyl groups and further support that C_{22} sites remain unreacted as suggested by the X-ray analysis.

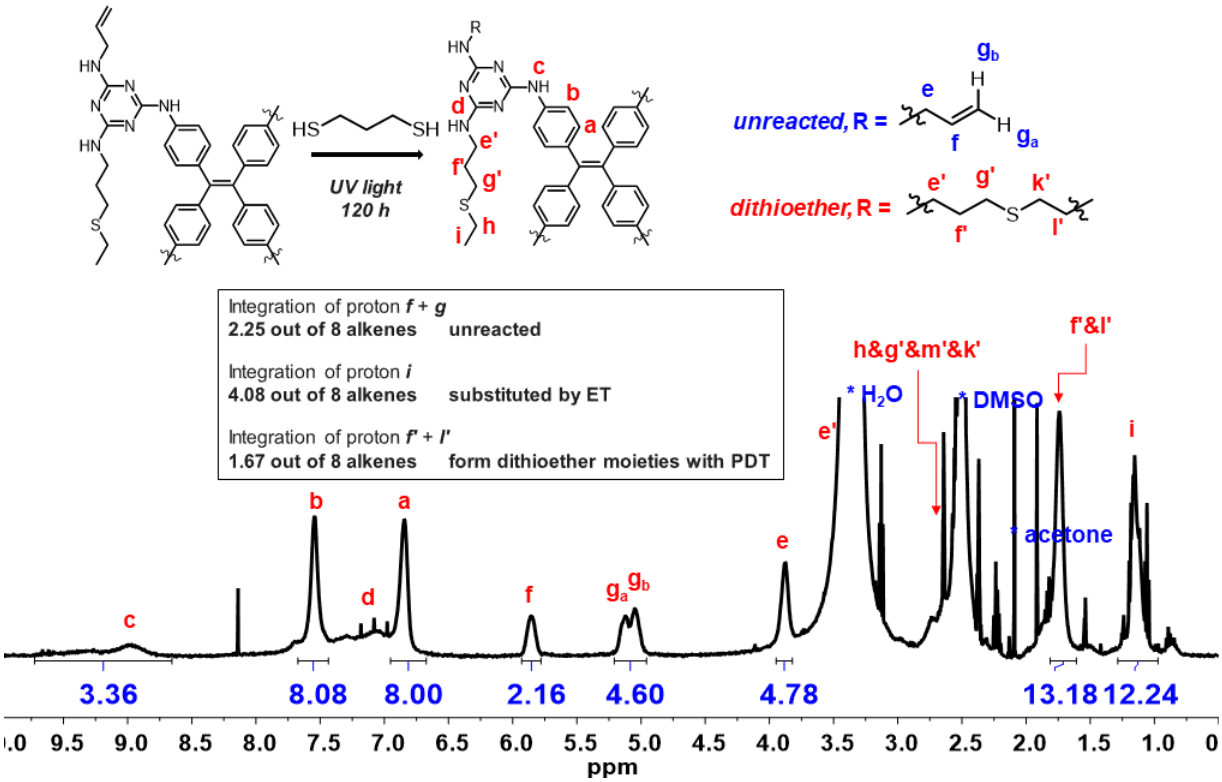

Figure S47. ^{1}H NMR spectrum (298 K, 500 MHz, DMSO-d_6) of ET-substituted crystal samples **[1**·(3-4)ET**]** immersed in 2 mL neat PDT and UV irradiated for 120 h. After 120 h of irradiation, two out of eight alkenes per monomer in the crystal samples remained unreacted, with less than two of the alkenes reacted with PDT.

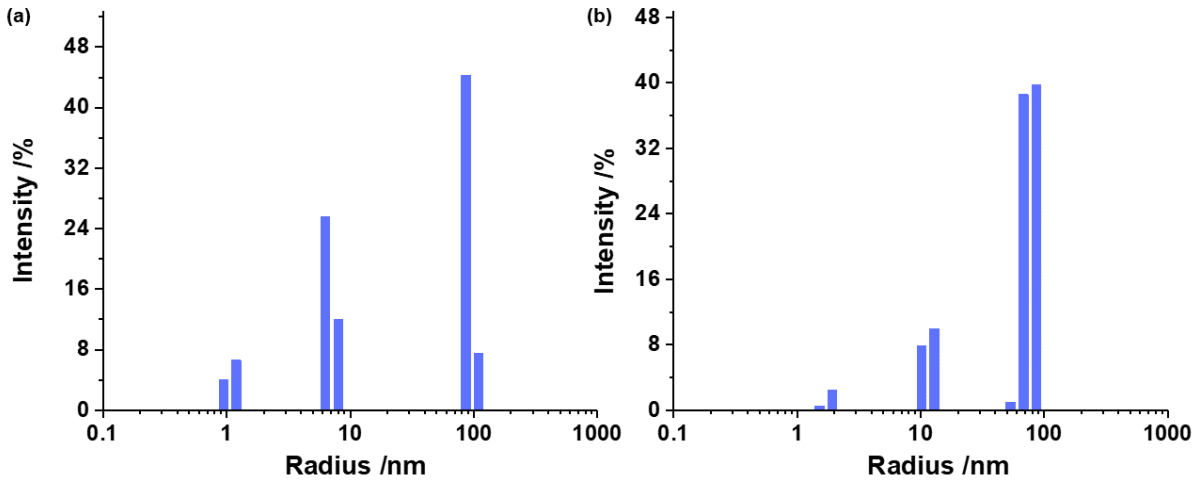

Figure S48. Dynamic light scattering pattern of the ET-substituted crystal samples **[1**·(3-4)ET**]** immersed in 2 mL neat PDT and UV irradiated for 60 h (a) and 120 h (b). The particle sizes of the sample lie in 1 – 10 (oligomer) and 80-120 nm (polymer) range.

Identifying the crosslinking topology in H_COF-3

Possibility 1. The first possible topology for H_COF-3 arises from crosslinking of C_{31} parallel to the *a*-axis. Cross-linking in this manner supplements that of the S_1 and S_2 sites in extending the structure along the *a*-axis. The carbon-carbon separation for this pair of crosslinking sites is quite short compared to the length of the PDT crosslinker. Also, in order for a single PDT molecule to react with both C31 and C31*[a], it must penetrate the bilayer. Such intercalation would likely produce too much steric crowding to allow the second pair to react, leading to potential assembly errors in the bulk crystal. Crosslinking of an ET-blocked sample of $\mathbf{1}_{crystal}$ in this manner would produce a disentangled 1D polymer.

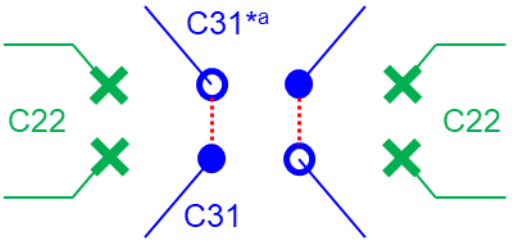

Possibility 2. Crosslinking between C_{31} and C_{31}*[c] produces a linker orthogonal to those of S_1 and S_2, extending the structure along the *c*-axis producing a formal 2D network topology. The carbon-carbon separation is more suitable to the length of the PDT molecule. However, similar to *possibility 1*, C_{31} and C_{31}*[c] lie on opposite faces of the bilayer structure and thus require some degree of inter-layer penetration in order for crosslinking to occur at these sites. Such intercalation would likely produce too much steric crowding to allow the second pair to react, leading to potential assembly errors in the bulk crystal. Crosslinking of an ET-blocked sample of $\mathbf{1}_{crystal}$ in this manner would also produce a disentangled 1D polymer.

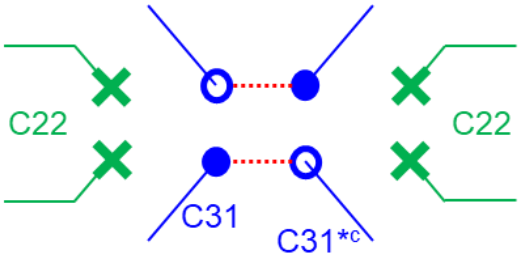

Possibility 3. The third proposed topology results from crosslinking of C_{31} with C_{31}*[ac]. Carbon-carbon separations are comparable to *possibilities 1&2*, however, unlike *possibilities 1&2*, C_{31} and C_{31}*[ac] lie on the same face of the bilayer, obviating the need for PDT to diffuse through the layers themselves and allowing crosslinking to occur more readily in a superficial manner. The result is a formal 2D network topology of H_COF-3. This crosslinking will generate the least steric hinderance for PDT crosslinking, therefore resulting in a 1D polymer as we observed in the analysis of **[1**·(3-4)ET**]** with PDT. **Based on the experimental results and SCXRD analysis, we suggest *possibility 3* is the most reasonable crosslinking scenario**.

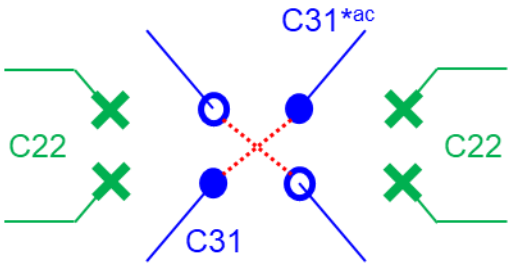

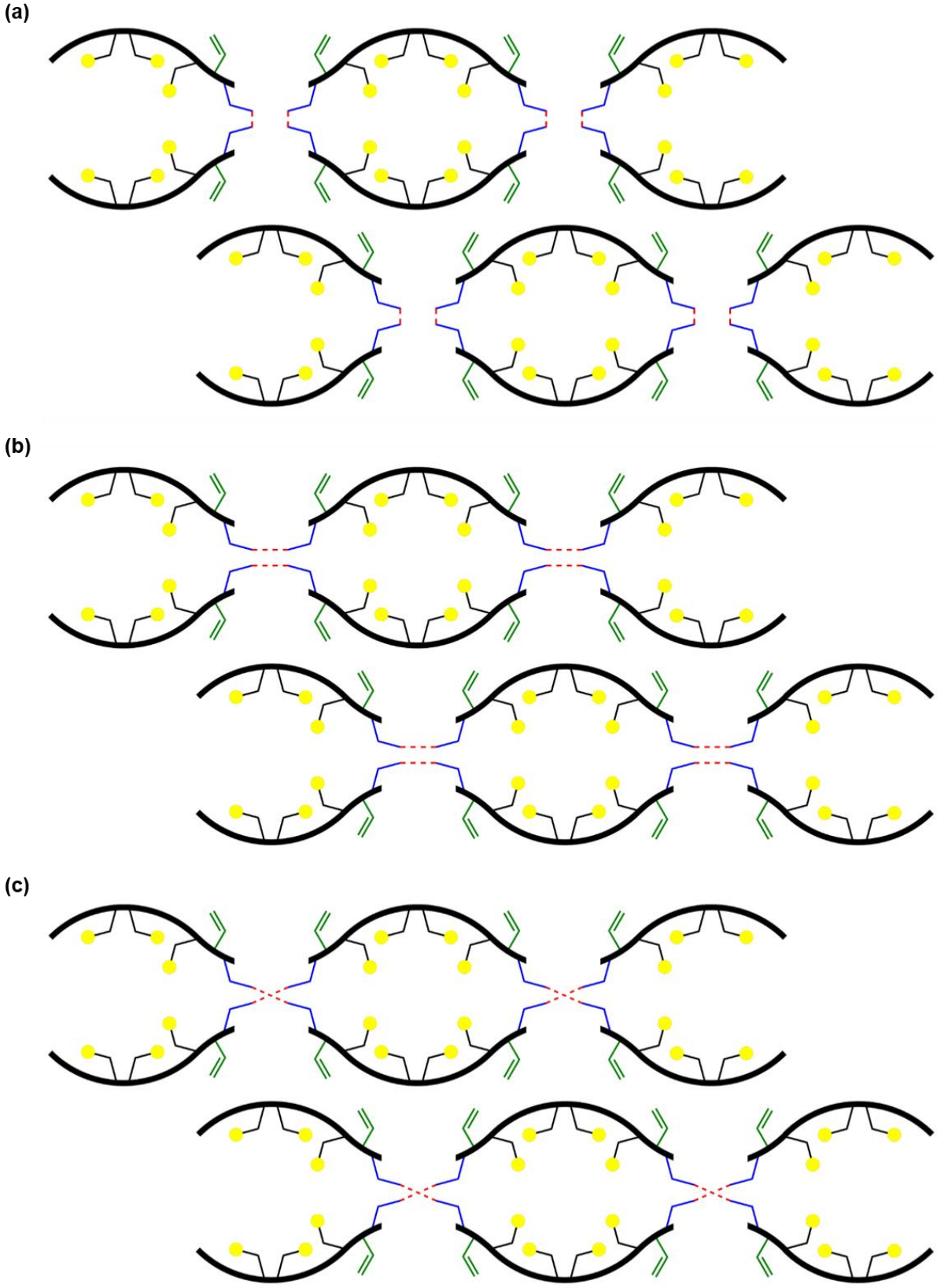

Scheme S8. Schematic representation of hypothetical topologies formed from homotopic crosslinking of **[1**·(3-4)ET**]**$_{crystal}$ by PDT: (a) 1D polymer expected from *[par-a]* crosslinking mode, (b) 1D polymer expected from *[par-c]* crosslinking mode, and (c) 1D polymer expected from *[cross-ac]* crosslinking mode.

Topological Analysis

1. H-bonded packing of molecules. Topological analysis was performed using ToposPro software[6] (https://topospro.com/). Following the approach for the analysis of H-bonded networks,[7] in $\mathbf{1}_{\mathbf{crystal}}$, as discussed above, each monomer is connected to six adjacent monomers via N–H···N hydrogen bonding, hence can be simplified as a six-coordinated node to assemble into a uninodal ***snw*** 3D network with point symbol of $(4^9.6^6)$ (Figure S49). This net was found only in two H-bonded networks (CCDC RefCodes QUJTEV and XUDROF) and one (BIHBAX) metal-organic framework.[8] Alternatively, to better match the topology of the monomer, it can be represented as a group of five nodes producing a centered rectangle: one at the center of the C_2Ph_4 moiety (node Y) and four in the centers of melamine corners (nodes B). The resulting topology is a new 3-nodal 4,4,4-c net B_2YB_2 with point symbol $(4.6^4.8)_2(4^2.6^2.8^2)(4^2.6^4)_2$. We gave a new name to the net, *cdc*1 (**C**hemistry **D**artmouth **C**ollege), and deposited it to the collection of topological types of ToposPro (TTD).[9] The $\mathbf{2}_{\mathbf{crystal}}$ shares the same topology since it possesses the identical monomer packing as in $\mathbf{1}_{\mathbf{crystal}}$. The H-bonded 3D network also remains the same in all the polymeric and framework compounds H_COFs-2-4 and **P5-P8**.

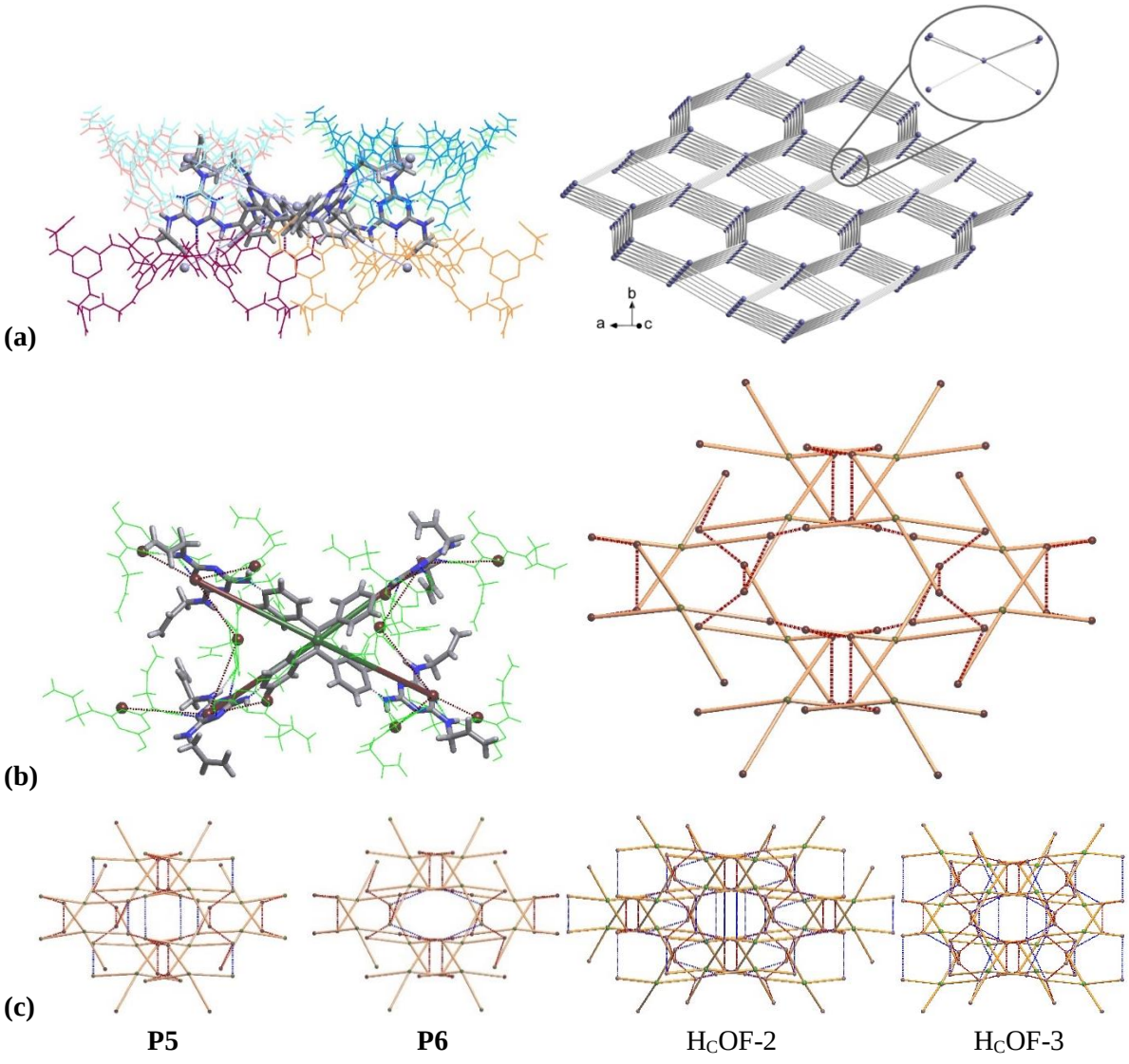

Figure S49. Topological representation of crystal packing in $\mathbf{1}_{\mathbf{crystal}}$ by 6-c **snw** net (a) and 4,4,4-c *cdc*1 underlying net (b) (dashed brown lines are edges corresponding to intermolecular H-bonds). The nets for **P5**, **P6**, H_COF-2, and H_COF-3 are represented as 4,4,5-c, 4,4,5-c, 4,6,6-c, and 4,5,6-c supernets of *cdc*1, respectively, with additional edges in blue dashed lines denoting dithiolate links (c).

2. Topology of crosslinking

2.1. Enumeration of hypothetical crosslinking

The *cdc*1 net serves as a blueprint for the construction of cross-linked networks of H_COFs-2-4 and **P5-P8**. The Y-B edges are related to valence links between the TPE core and melamine corners of one molecule, while B-B edges represent intermolecular linkage by H-bonds between melamine corners of neighboring molecules. Additional edges representing dithiolate links can be established only between B nodes: melamine corners of the same molecule or neighboring molecules. The maximal number of extra edges per one B node is two, that it is equal to the number of allyl groups per one melamine corner, and the maximal number of links incident to one monomer equals eight. We can generate all topologically possible variants of crosslinking for the structure $\mathbf{1}_{\mathbf{crystal}}$ in the space group *Fddd b*y sequential addition of links, one by one, between C_{22}, C_{25}, C_{28}, and C_{31} atoms (nodes) that are at a distance less than 12 Å. This approach has been implemented in ToposPro for generation of intermediate phases in phase transformation modelling.[10] Here we adapt it for SCSC chemical reactions. There are in total 68 possible C-C contacts of different length for C_{22}, C_{25}, C_{28}, and C_{31} atoms in the structure.

As a result, 2225 different networks (sets of additional edges) can be generated. However, as it was outlined above not all links can be realized in structures H_COFs-2-4 and **P5-P8**; only five links are acceptable: C_{25}-C_{25} (11.962 Å), C_{28}-C_{28} (two of 4.174 Å and 6.909 Å), C_{22}-C_{31} (*[het-cis-1]*; 6.745 Å), C_{31}-C_{31} (*[cross-ac]*; 3.919 Å). Considering only reasonable links leads to 17 different networks and only four of them were experimentally proven for structures of H_COFs-2-4 and **P5-P8**. Two 4,4,5-c nets represent the topologies of **P5** (C_{25}-C_{25} link of 11.962 Å) and **P6** (C_{28}-C_{28} link of 4.174 Å), one 4,6,6-c net of H_COF-2 (C_{28}-C_{28} of 6.909 Å, C_{25}-C_{25} of 11.962 Å, C_{22}-C_{31} of 6.745 Å), and one 4,5,6-c net of H_COF-3 (C_{28}-C_{28} of 4.174 Å, C_{25}-C_{25} of 11.962 Å, C_{31}-C_{31} of 3.919 Å) (Figure S49). The list of the four nets with centers of monomers in Y nodes, melamine centers in B nodes, and C-C links between B nodes are presented in the supplementary file "cdc1_supernets.cif" with bonding list written in ToposPro format (https://comcifs.github.io/Topology.dic.html). The other 13 generated nets do not satisfy the experimental observations revealed above by SCXRD, NMR, and DLS analysis.

2.2. Description of crosslinking topologies from SCXRD data, NMR, and DLS analysis

In **P5**, the crosslinker, EDT, connects adjacent monomers into a simple chain along [100]. The flexible dithiol crosslinkers thread through another half ring that is circled by neighboring EDT, weaving the 1D chains into overall 2D nets packing along the *c*- axis in the (010) plane following the "chicken-wire" pattern ***wvx*** described[11] before (Figure S50a). To the best of our knowledge, only two other examples of the same weaving pattern were found previously.[12]

In **P6**, however, the PDT crosslinkers directly link neighboring monomers along the *a*-axis into a 1D linear chain (Figure S50b). Thus, topology of crosslinking in **P5** and **P6** are similar, but they differ by shape of the resulting chains and realization of weavings.

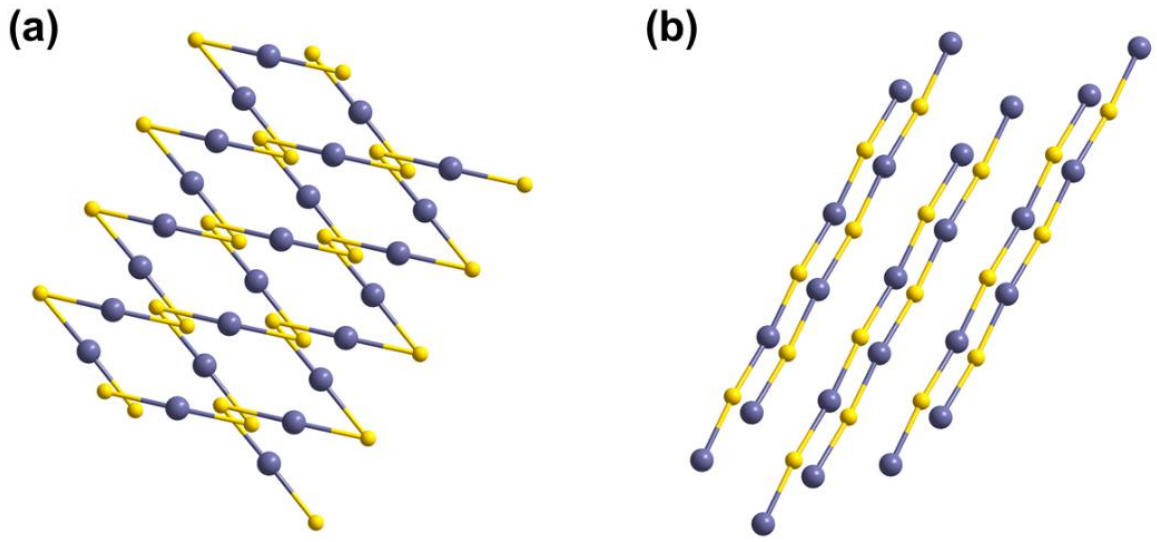

Figure S50. Topological representation of crosslinking in **P5** (a) and **P6** (b). The monomers (blue gray) are connected by dithiol crosslinkers (yellow) to 1D chains.

With more crosslinkers in H_COFs, more discrepancies in crosslinking topology are brought into the valence-bonded frameworks (Figure S51). From SCXRD analysis we can identify that in H_COF-2, the monomers as nodes are connected in most reactive sites by EDT as bridges C_{28}-C_{28} and C_{25}-C_{25} into the topological motif of a 2D 4-c uninodal net 4L7 with point symbol (6^6). The layers are oriented normal to the [001] direction. EDT links enclose monomers in 6-rings of the net and, taking into account mutual weaving of EDT links, the 2D→3D parallel polycatenation of Hopf type (with enclosed rings) can be detected along the *c*-axis. The polycatenation is characterized by index of separation IS=2 (two 2D net should be removed to disjoint the polycatenated array into separate parts) and degree of catenation DOC=4 (four 2D nets are catenated with each one). This unique topology of catenation, described by 70,76,80,81-c Hopf Ring net, is observed for the first time.[13] The net 4L7 was found before in 17 other structures (3 H-bonded molecular crystals and 13 MOFs), but none of them are entangled [https://topcryst.com/].

Consideration of the additional link C_{22}-C_{31}, identified by NMR and DLS analysis for **[1**·(3-4)ET**]**$_{\mathbf{crystal}}$ with EDT, gives us the opportunity to build a complete picture of topology of crosslinking that was impossible to do only from SCXRD data. Thus, the topology of crosslinking now can be described as a 3D 3-nodal 3,3,4-c net with stoichiometry $(3\text{-c})_2(3\text{-c})_2(4\text{-c})$ and point symbol $(6.10.12)_2(6.12^2)_2(6^2.10.12^3)$ (TD10=1129). This 3D net is self-entangled since it keeps catenations determined for 4L7 subnet.

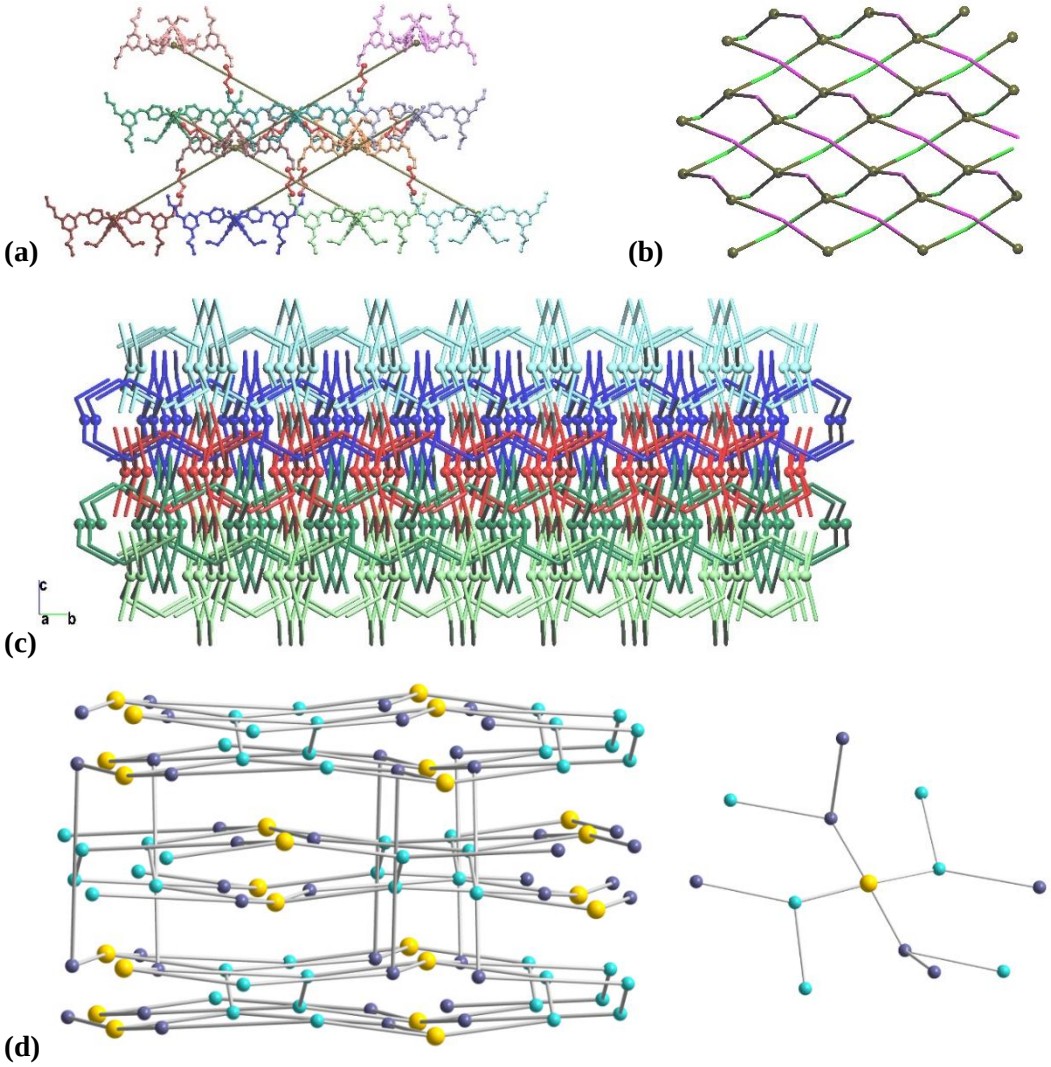

Figure S51. (a) Topological representation of partial crosslinking of monomers by EDT links in H_COF-2 as 2D 4L7 net determined from SCXRD data. The EDT crosslinkers are highlighted in red, and monomers are highlighted in different colors. Hydrogen atoms are omitted for clarity. (b) The 2D uninodal 4-c net 4L7 with bent edges (pink above and green below of the middle plane). (c) Polycatenation of 4L7 nets with bent edges related to interwoven EDT links. (d) The complete topological representation of crosslinking of monomers as 3D 3,3,4-c net revealed from SCXRD data, NMR, and DLS analysis. Yellow and blue balls represent centers of the TPE core and melamine arms, respectively.

In H_COF-3, we use the same node assignments and simplification method as H_COF-2. From SCXRD data, a partially crosslinked net in the most reactive sites by C_{28}-C_{28} and C_{25}-C_{25} bridges is constructed from the monomer as a 4-c node and two 2-c linking dithioethers as edges. The resulting topology is 1D uninodal 4-c net 3^6(1,2) (a *ladder of triangles* 1-periodic sphere packing by Koch&Fisher[14]). The ladders run along the *a*-axis (Figure S52). The 1D network is packed with other equivalent nets orthogonally to the *a*-axis. Moreover, due to the bent shape of PDT links, they are interwoven along the *c*-axis producing 1D→2D parallel polycatenation with IS=1 and DOC=2. Polycatenation for 3^6(1,2)

networks was observed before in six coordination polymers[15] (CCDC RefCodes ESADEJ, GOVWUL, OTAREH, RESWUJ, SIQDIH, VEGZAK). However, the pattern of catenation in H_COF-3 is unique and described by a 2D extended ring net (ERN) of 6L39 type, which is different from 2D 6-c **hxl** (ESADEJ, RESWUJ, VEGZAK) and 2D 3,5-c **sdd** (GOVWUL, OTAREH, SIQDIH).

Taking into account the C'_{31}-C'_{31} bridges revealed from NMR and DLS analysis enables us to identify the complete crosslinking topology of H_COF-3: 2D 2-nodal 3,4-c net with stoichiometry $(3\text{-c})_2(4\text{-c})$ and point symbol $(7.8^2)_2(7^3.8^3)$ (TD10=447).

It is obvious that the topology of H_COF-3 / **P6** is distinct from the topology of H_COF-2 / **P5** due to the different crosslinking among alkene sites and different weaving patterns of linking dithioethers.

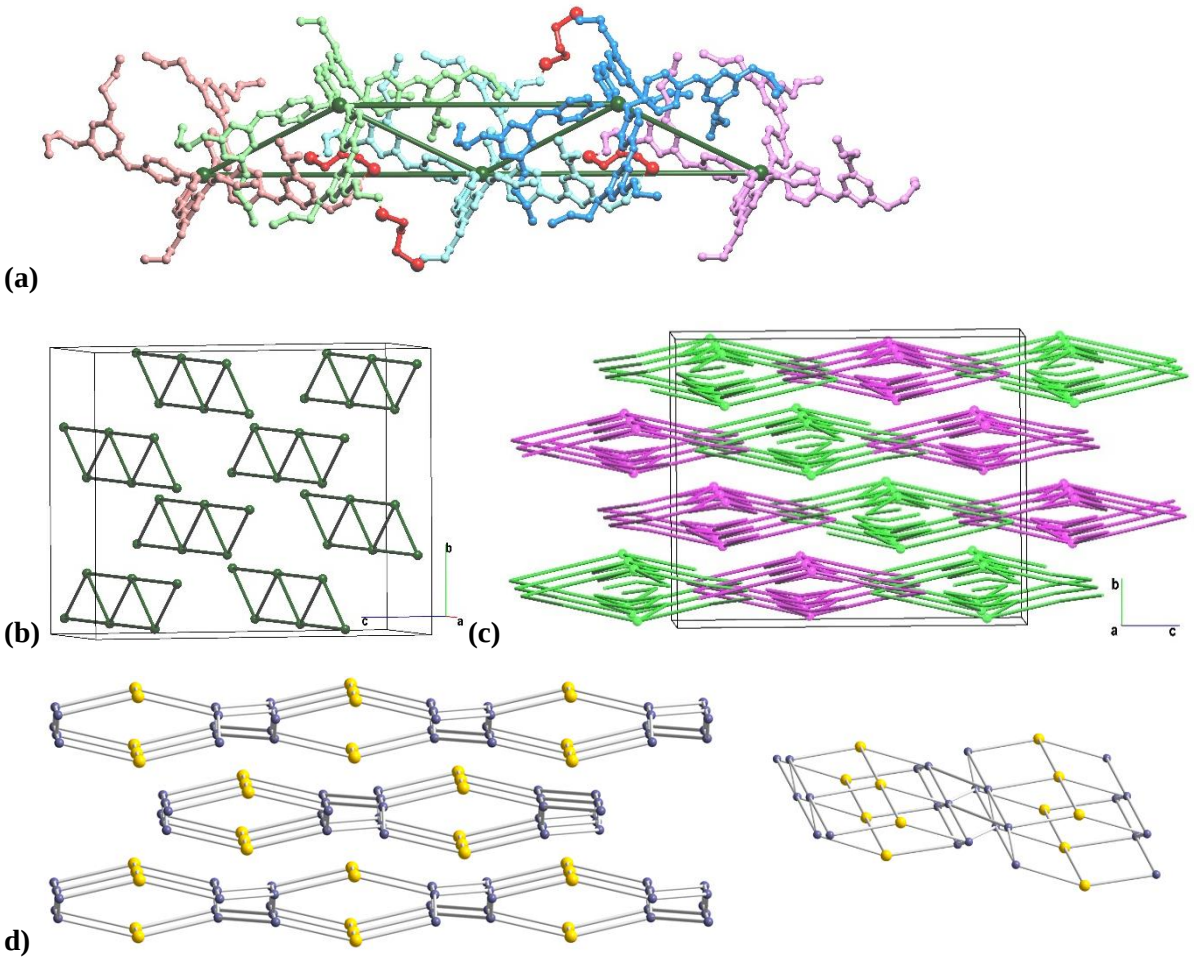

Figure S52. (a) Topological representation of crosslinking in H_COF-3 determined from SCXRD data. (b) The 4-*c* TPE core (dark green balls) are connected by PDT links (dark green cylinders) along the *a*-axis into a uninodal 1D chain of topology $3^6(1,2)$. (c) The $3^6(1,2)$ nets with bent edges are polycatenated along the *c*-axis. (d**)** The complete topological representation revealed from SCXRD, NMR, and DLS analysis results in the crosslinking of the polycatenated ladders into a 2D 3,4-connected net with stoichiometry $(3\text{-}c)_2(4\text{-}c)$ and point symboll $(7.8^2)_2(7^3.8^3)$. Yellow and blue balls represent the centers of the TPE core and melamine arms, respectively.

S7. Iodine sorption investigations

Iodine adsorption measurements. To quantify the I_2 uptake capacity of H_COFs in an aqueous environment, H_COF crystal samples (e.g. H_COF-2: 23.3mg, H_COF-3: 18.4 mg and H_COF-4: 26.6 mg) were soaked in a 1 mL KI_3 concentrated aqueous solution (0.17 g KI and 0.22 g I_2) for 24 h, and then the vial was re-charged with 1 mL KI_3 solution twice more, after 24 and 48 h, respectively. The crystal samples were kept in the KI_3 solution until the measured mass reached a constant value. The dark crystal samples were collected by filtration, washed with an excess of water until the filtrate become colorless, and dried in open air to yield I_2⊂H_COFs-2-4 (e.g. I_2⊂H_COF-2: 98.0 mg, I_2⊂H_COF-3: 75.6 mg and I_2⊂H_COF-4: 122.5 mg). This experiment has been repeated more than 3 times by two individuals and the averaged iodine uptake capacities of H_COFs are listed in Table S9. The obtained crystal samples were also analyzed by elemental analysis and thermogravimetric analysis to cross verify the iodine uptake capacities of H_COFs-2-4.

Table S9. Iodine uptake capacities of H_COFs measured by gravimetric, elemental and thermogravimetric analyses.

	Iodine adsorption (gram of iodine per gram of H_COF)		
	gravimetric	elemental analysis	TGA
H_COF-2	3.23 ± 0.18 g/g (repeated 4 times)	3.42 g/g	3.17 g/g
H_COF-3	3.00 ± 0.09 g/g (repeated 4 times)	3.15 g/g	2.95 g/g
H_COF-4	3.57 ± 0.10 g/g (repeated 6 times)	3.73 g/g	3.46 g/g

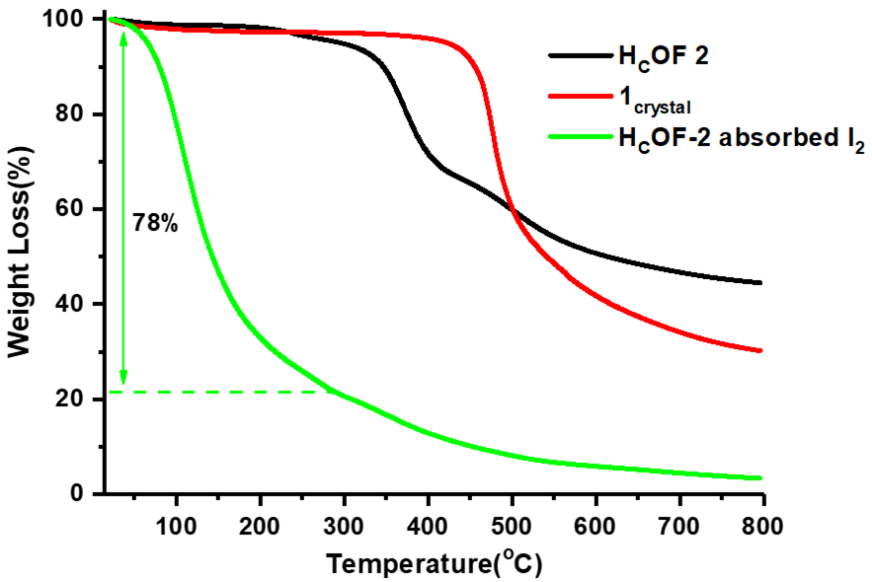

Figure S53. TGA profiles of $\mathbf{1}_{crystal}$ (red), H_COF-2 (black) and I_2⊂ H_COF-2 (green) obtained under N_2 atmosphere with a heating rate of 5 $^oC \cdot min^{-1}$.

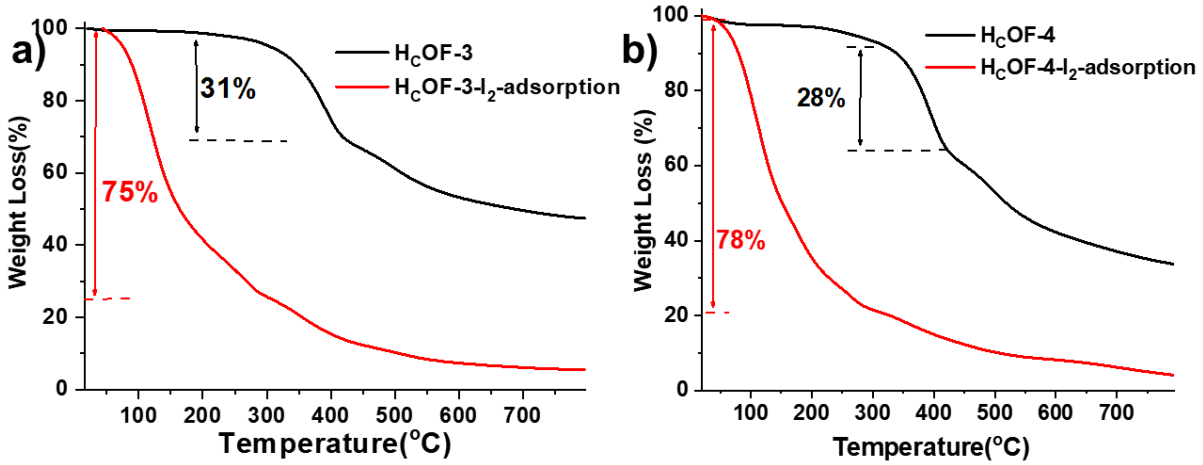

Figure S54. TGA profiles of (a) H_COF-3 (black) and I_2⊂H_COF-3 (red), and (b) H_COF-4 (black) and I_2⊂H_COF-4 (red) obtained under N_2 atmosphere with a heating rate of 5 °C·min^{-1}.

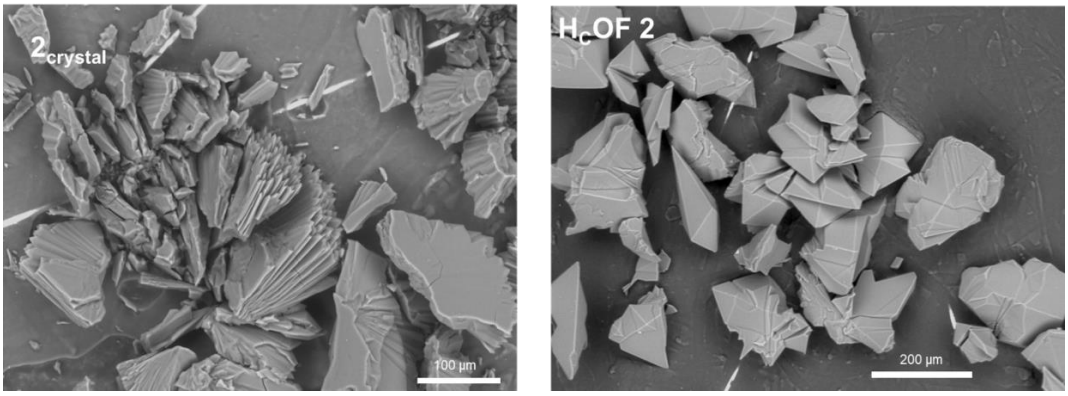

Figure S55. SEM images of $\mathbf{1}_{crystal}$ (*left*) and H_COF-2 (*right*)

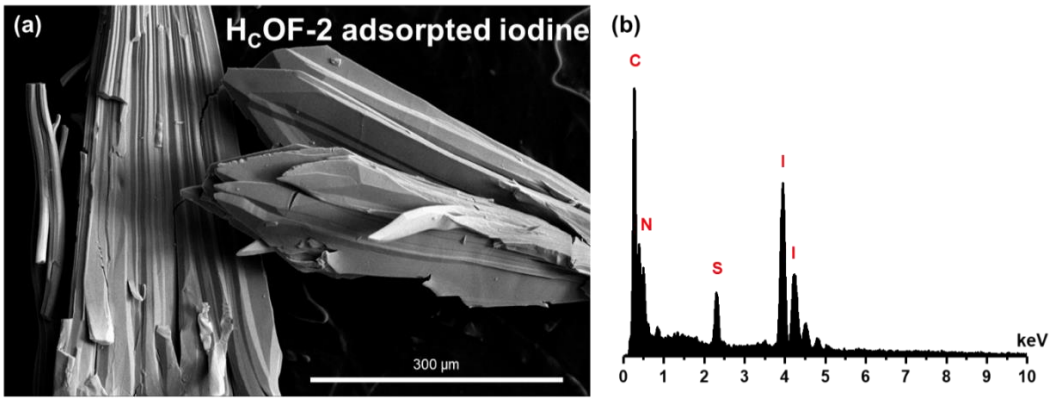

Figure S56. SEM image of I_2⊂H_COF-2 at 300 μm scale (a) and its EDS profile (b).

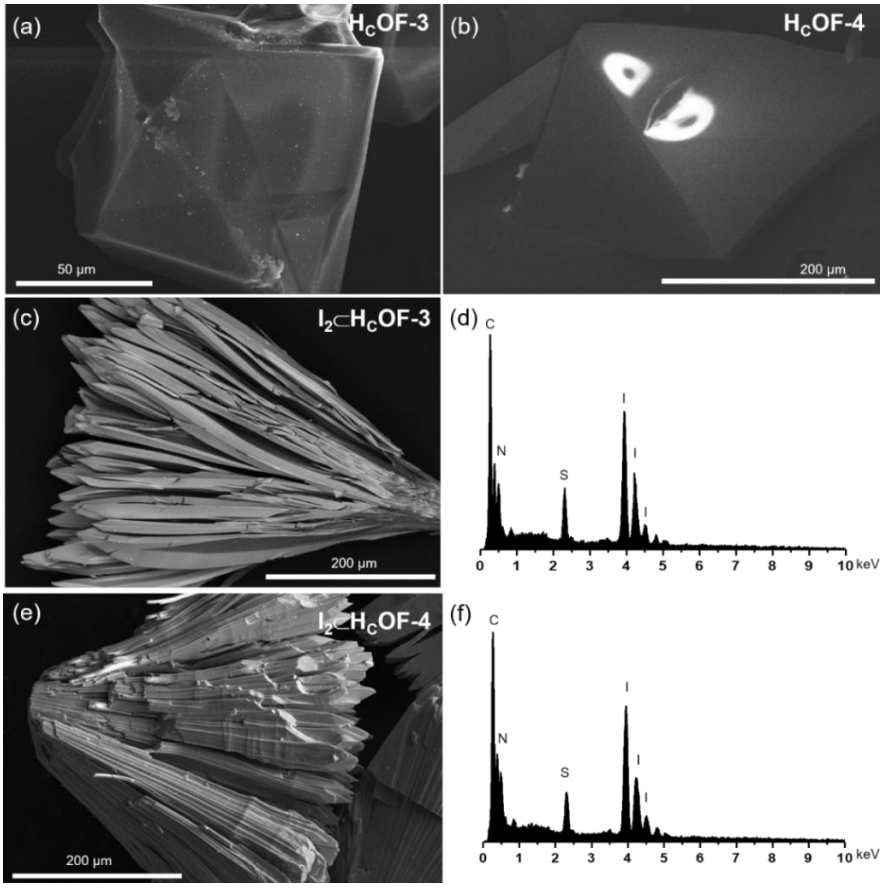

Figure S57. SEM images of (a) H_COF-3, (b) H_COF-4, (c) I_2⊂H_COF-3, (e) I_2⊂H_COF-4 and EDS spectra of (d) I_2⊂H_COF-3, (f) I_2⊂H_COF-4

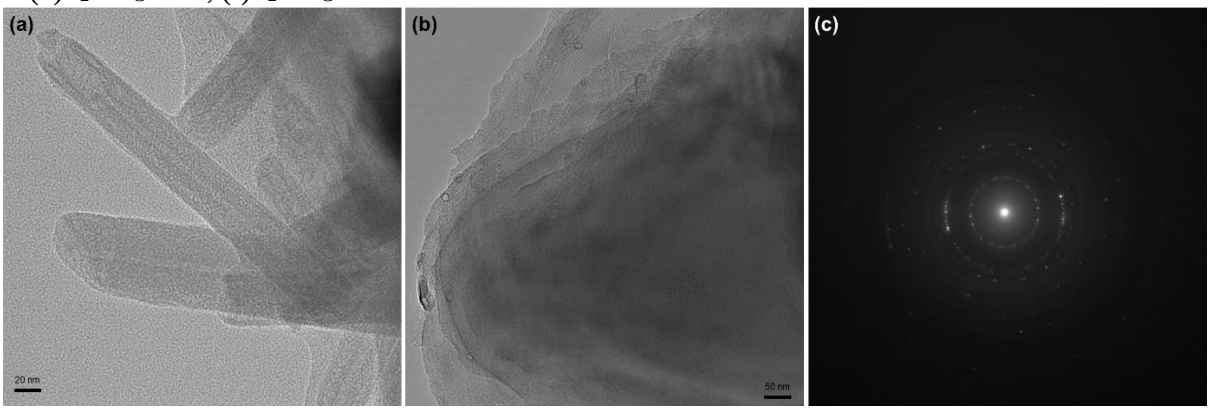

Figure S58. TEM images of H_COF-2 (a-b) and its electron diffraction pattern (c).

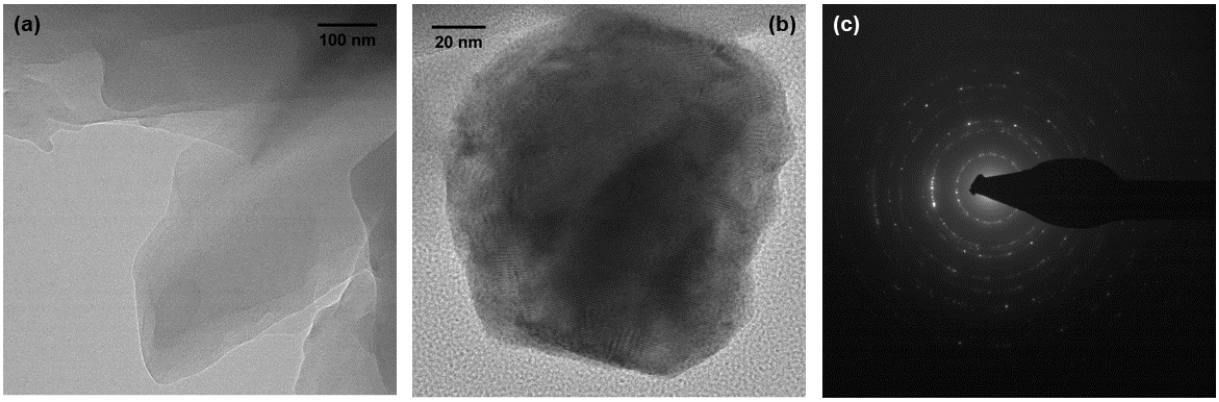

Figure S59. TEM images of H_COF-3 (a-b) and its electron diffraction pattern (c)

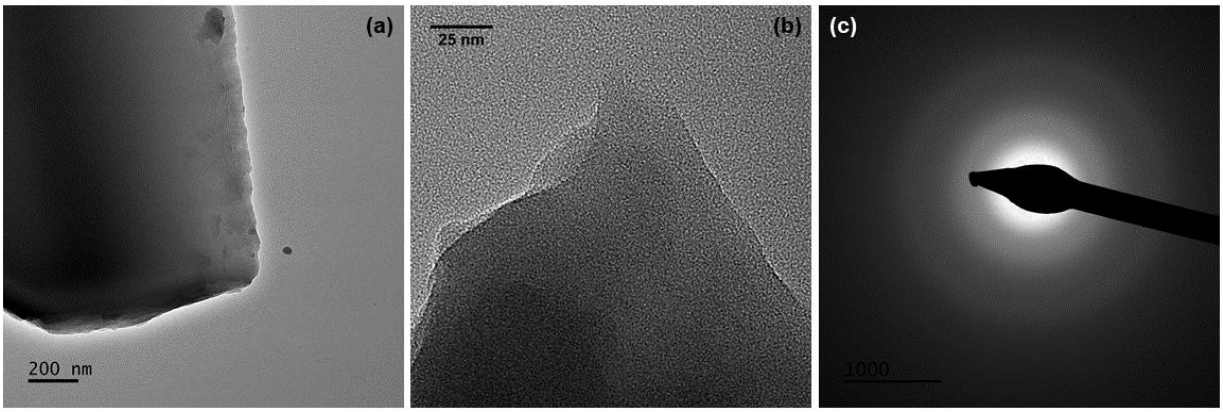

Figure S60. TEM images of $I_2 \subset H_C$OF-3 (a-b) and its electron diffraction pattern (c)

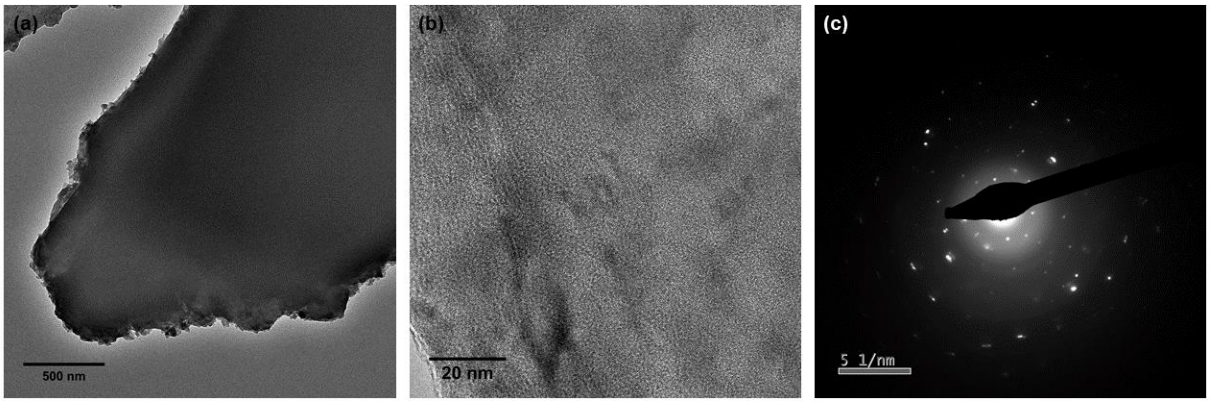

Figure S61. TEM images of H_COF-3 after I_2 desorption (a-b) and its electron diffraction pattern (c).

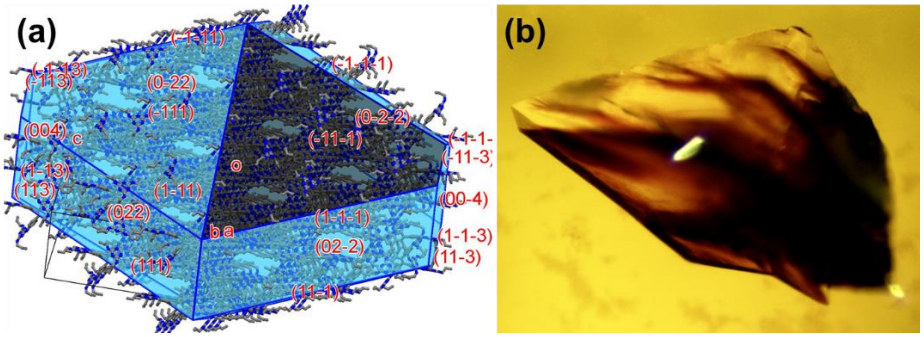

Figure S62. (a) The simulated morphology of a single crystal of H_COF-2 with the pore along $[\bar{1}1\bar{1}]$ direction. (b) A photo image of an H_COF-2 single crystal upon I_2 adsorption. The I_2 diffusion pathway is consistent with the pore direction in the simulated structure.

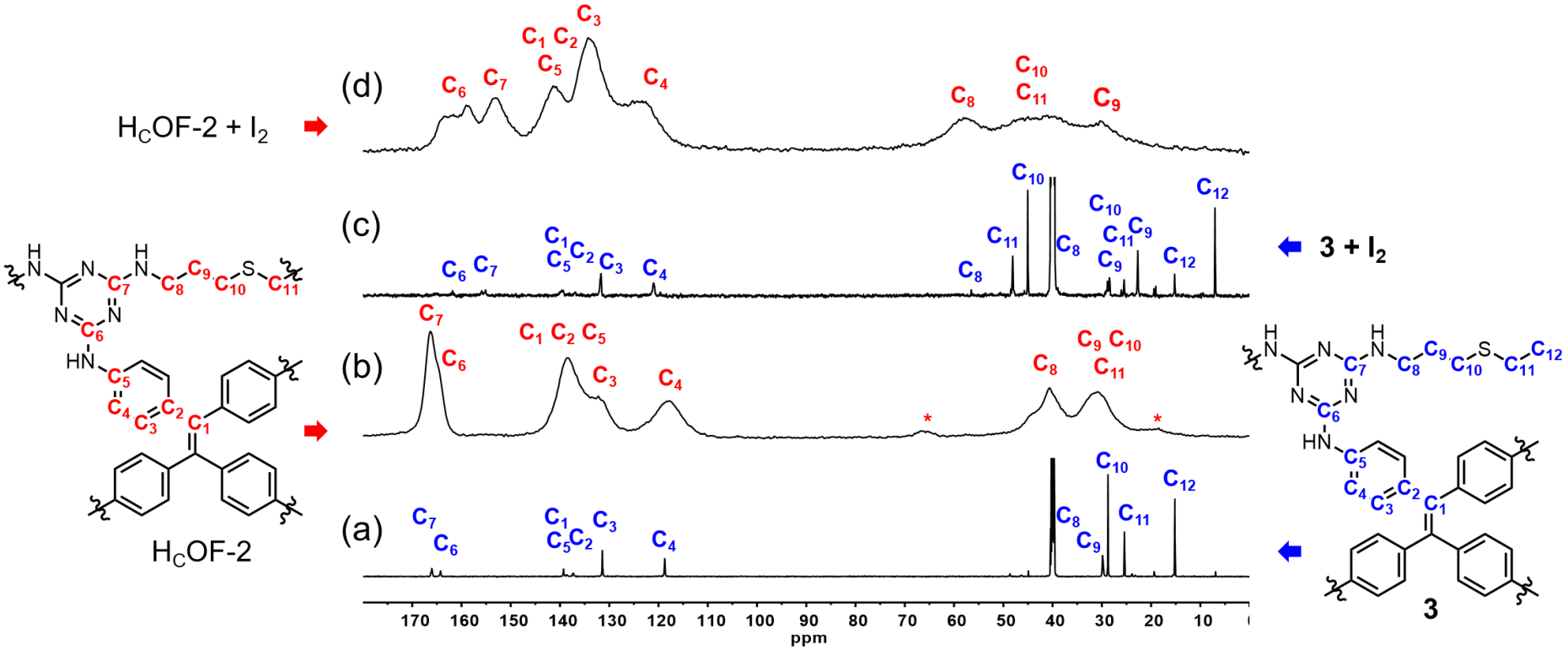

Figure S63. (a, c) ^{13}C NMR spectra (125 MHz, 298K) of **3** and I_2⊂**3** in DMSO-d_6. (b, d) Solid-state ^{13}C CPMAS NMR (100 MHz, 298K, 10000 rpm) spectra of (b) H_COF-2, and (d) I_2⊂H_COF-2 (side bands are noted as *).

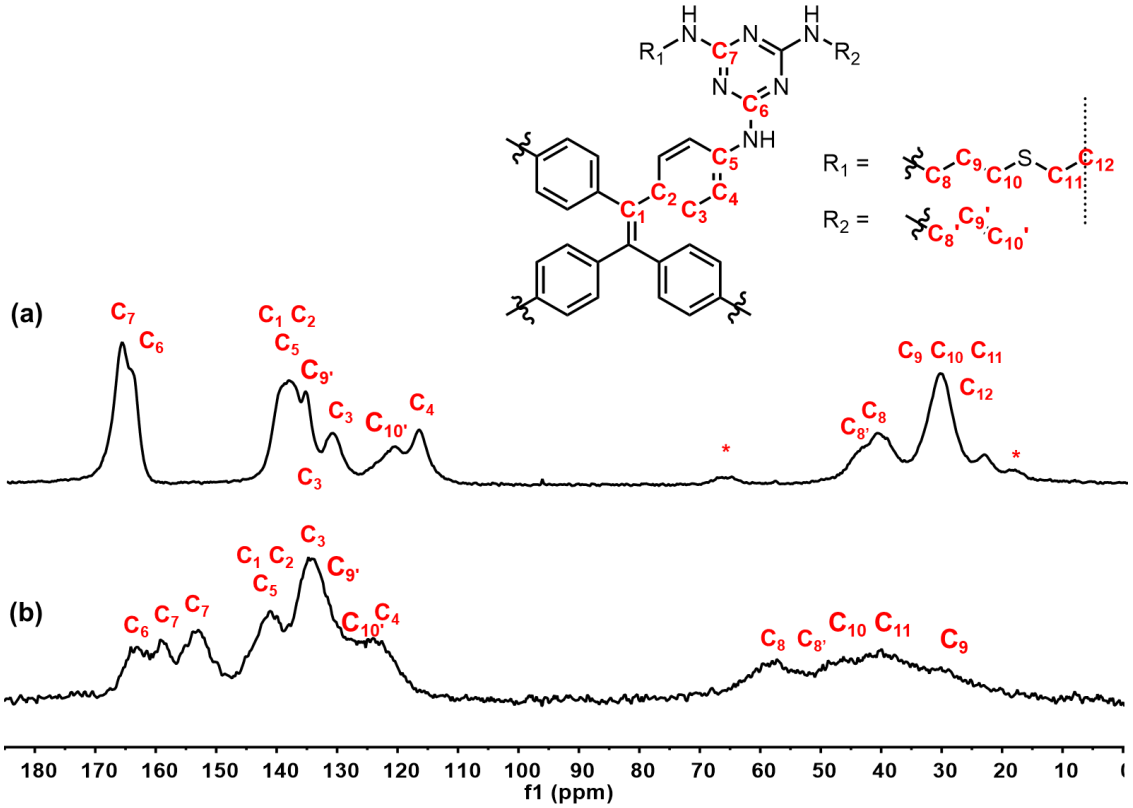

Figure S64. ^{13}C CPMAS NMR (100 MHz, 298K, 10000 rpm) spectra of (a) H_COF-3, and (b) $I_2 \subset H_C$OF-3 (side bands are noted as *).

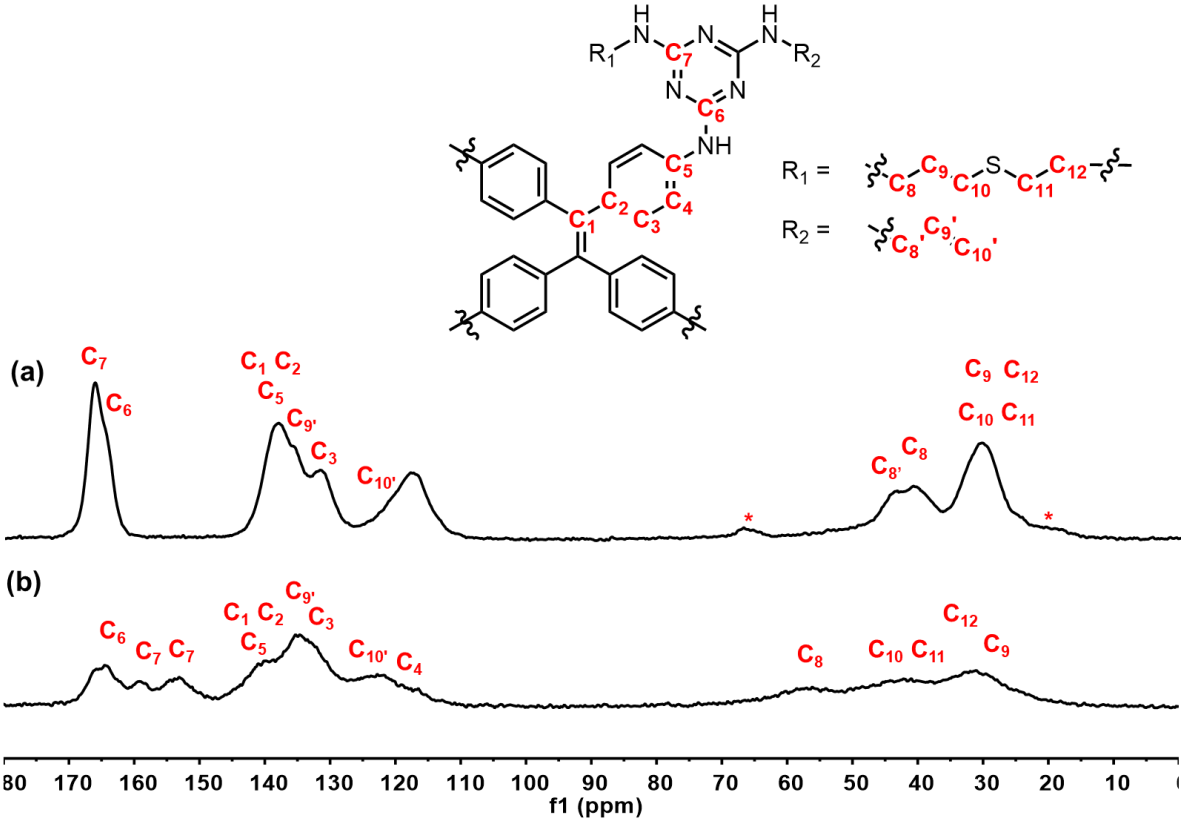

Figure S65. ^{13}C CPMAS NMR (100 MHz, 298K, 10000 rpm) spectra of (a) H_COF-4, and (b) $I_2 \subset H_C$OF-4 (side bands are noted as *).

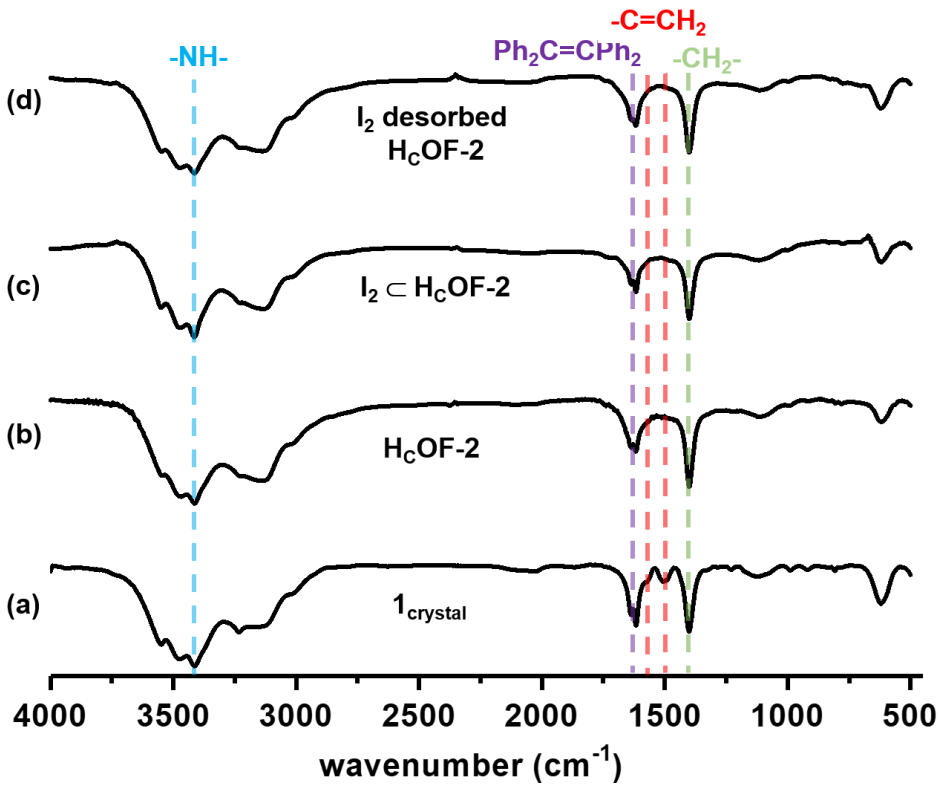

Figure S66. FT-IR spectra of (a) $\mathbf{1}_{\mathbf{crystal}}$, (b) H_COF-2, (c) $I_2 \subset H_C$OF-2 and (d) recovered H_COF-2 after iodine desorption, respectively. The signals at 1500 cm^{-1} assigned to vibration of the C=C bond of allyl groups were diminished after the thiol-ene crosslinking.

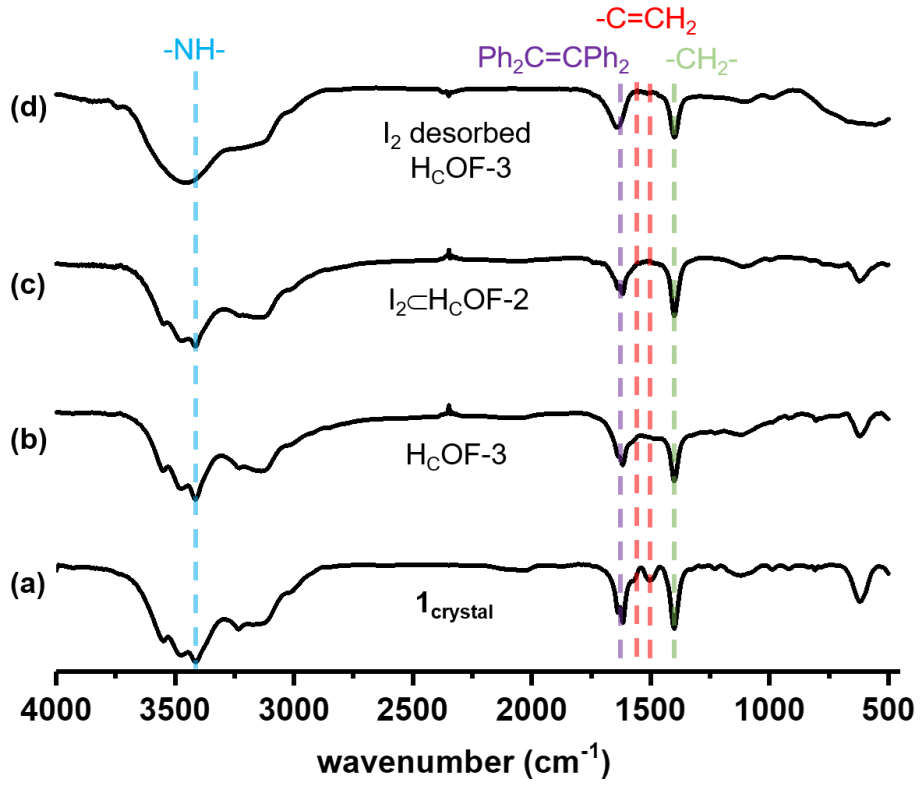

Figure S67. FT-IR spectra of (a) $\mathbf{1}_{\mathbf{crystal}}$, (b) H_COF-3, (c) $I_2 \subset H_C$OF-3 and (d) recovered H_COF-3 after iodine desorption, respectively. The signals at 1500 cm^{-1} assigned to vibration of the C=C bond of allyl groups were largely diminished after the thiol-ene crosslinking.

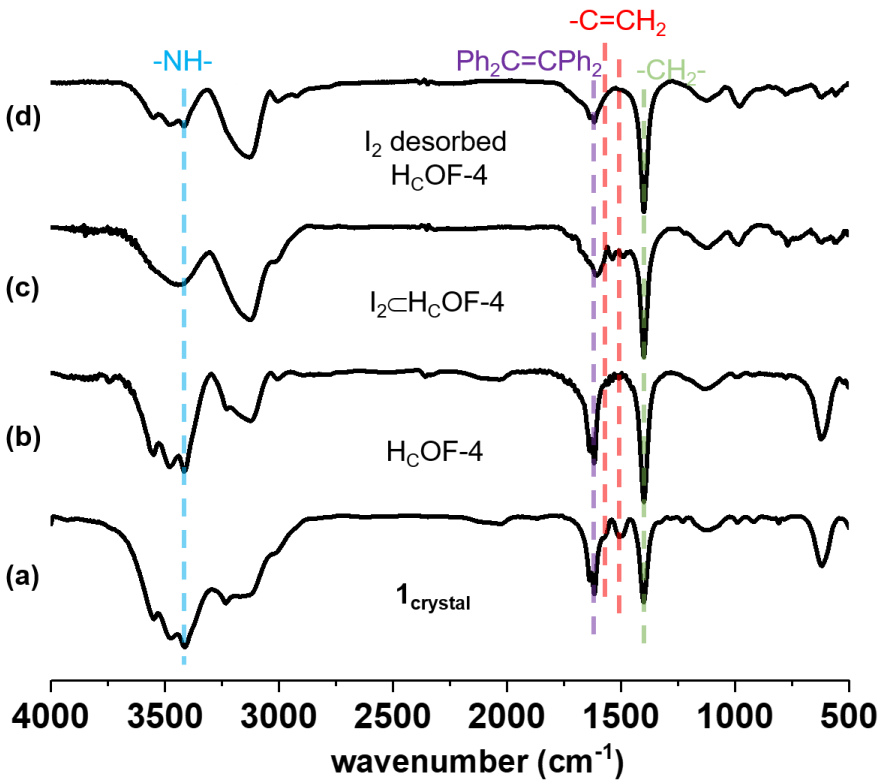

Figure S68. FT-IR spectra of $\mathbf{1}_{crystal}$, H_COF-4, $I_2\subset H_C$OF-4 and recovered H_COF-4 after iodine desorption. The signals at 1500 cm^{-1} assigned to vibration of the C=C bond of allyl groups were largely diminished after the thiol-ene cross-linking.

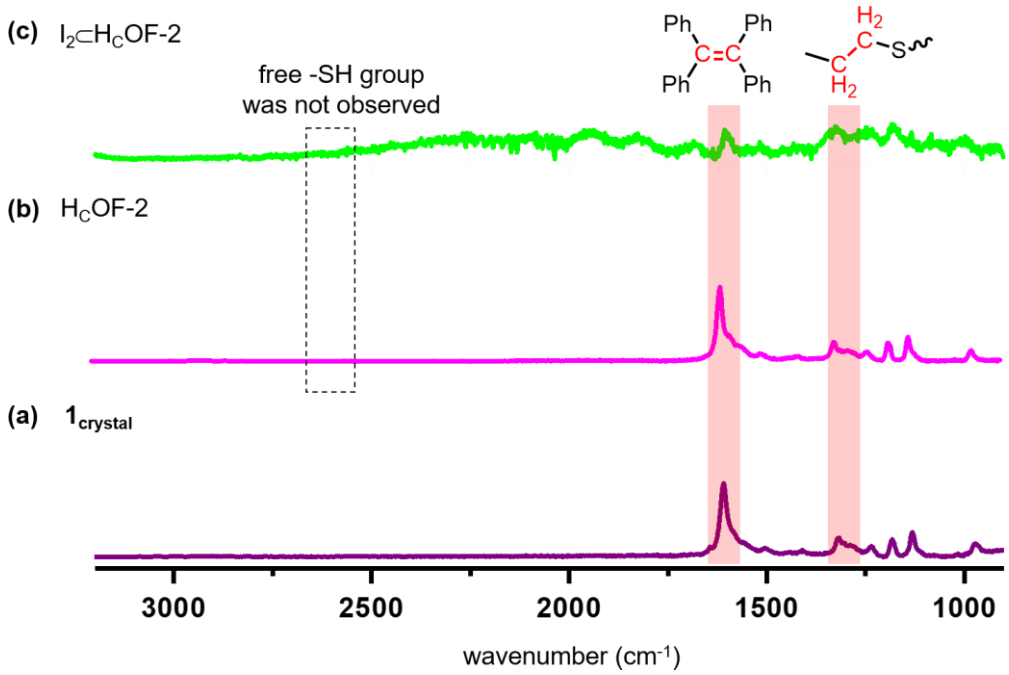

Figure S69. Raman spectra of crystalline samples of (a) $\mathbf{1}_{crystal}$, (b) H_COF-2 and (c) $I_2\subset H_C$OF-2 at 298K (λ = 580 nm), respectively.

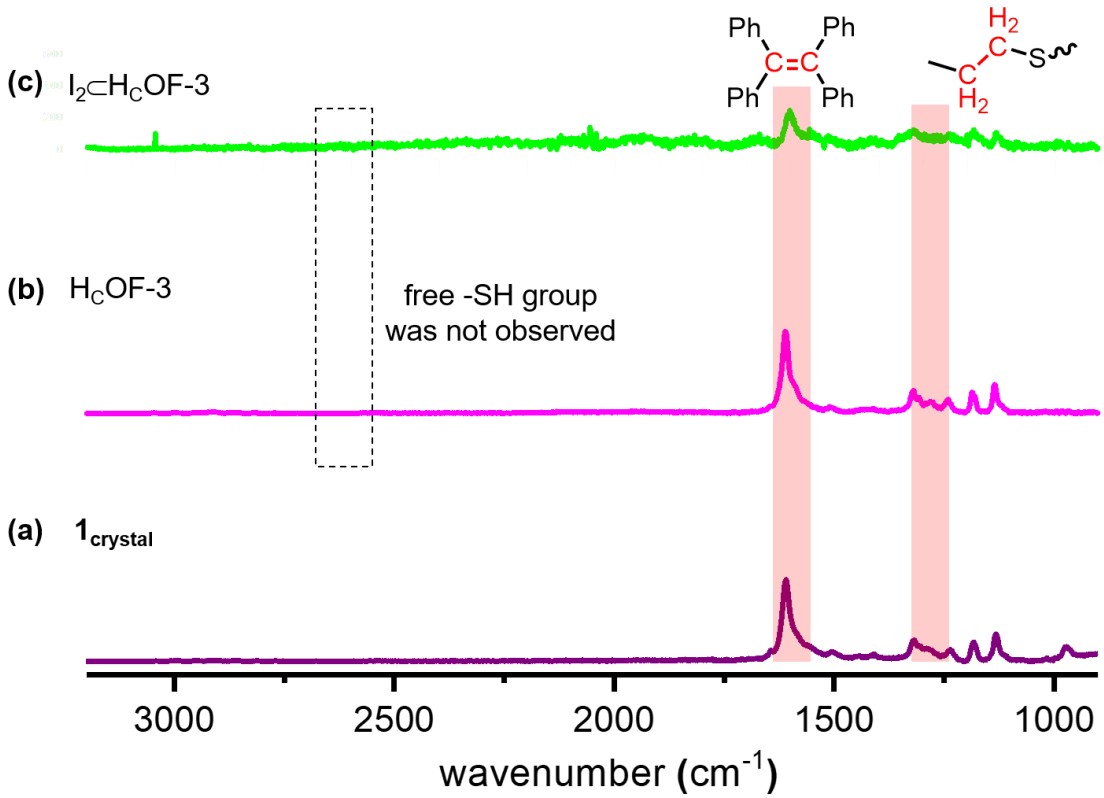

Figure S70. Raman spectra of crystalline samples of (a) $\mathbf{1}_{crystal}$, (b) H_COF-3 and (c) $I_2\subset H_C$OF-3 at 298K (λ = 580 nm), respectively.

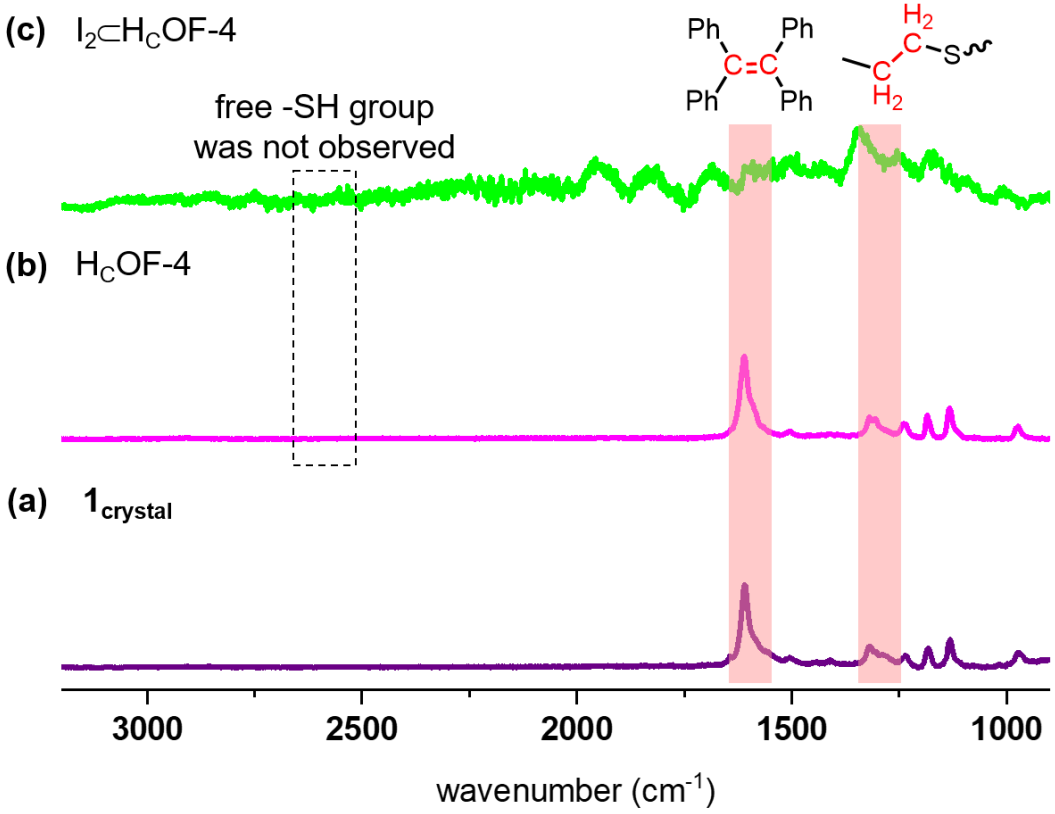

Figure S71. Raman spectra of crystalline samples of (a) $\mathbf{1}_{crystal}$, (b) H_COF-4 and (c) $I_2\subset H_C$OF-4 at 298K (λ = 580 nm), respectively.

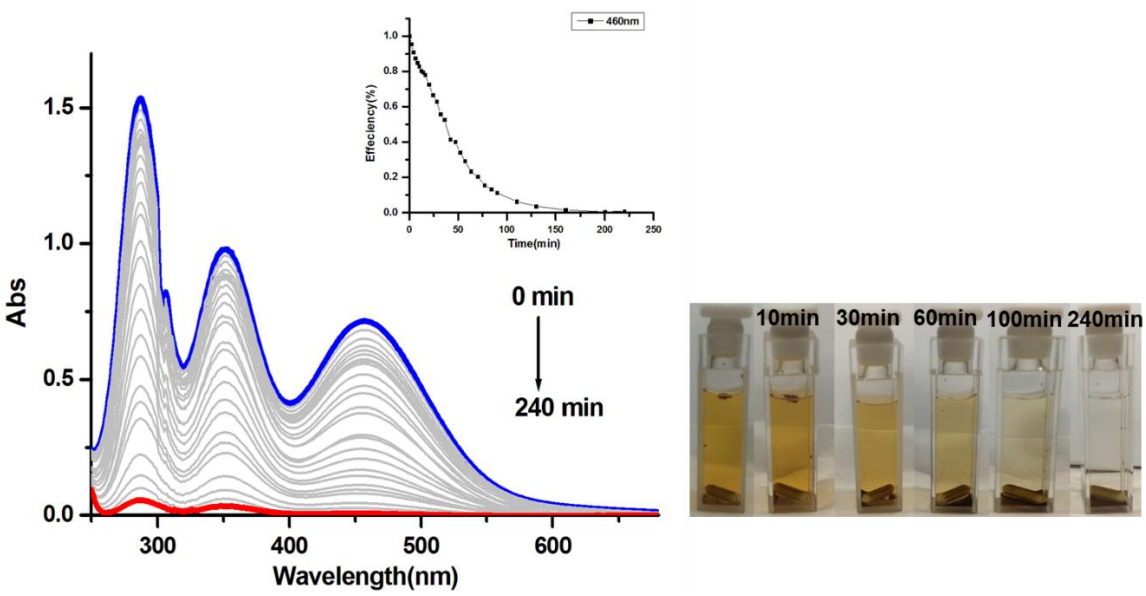

Figure S72. Time-dependent UV-Vis spectra of a saturated iodine aqueous solution (11.4 mM, 2 mL) recorded after adding H_COF-2 (10.0 mg) crystal samples. Blue: iodine saturated aqueous solution, t = 0, red: *end of the experiment*. Insert: time-dependent iodine adsorption efficiency.

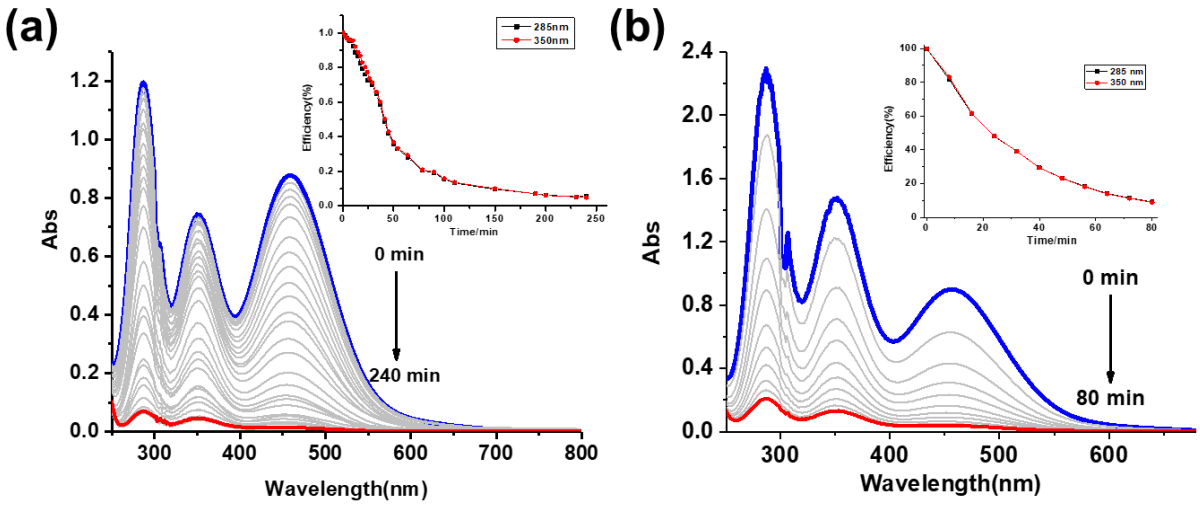

Figure S73. Time-dependent UV-Vis spectra of a saturated iodine aqueous solution (11.4 mM, 2 mL) recorded after adding H_COF-3 (a, 10.0 mg) and H_COF-4 (b, 10.0 mg) crystal samples. Blue: iodine saturated aqueous solution, t = 0, red: *end of the experiment*. Insert: time-dependent iodine adsorption efficiency.

General procedure for iodine desorption: Crystal samples of I_2⊂H_COFs (20 mg) were soaked in methanol, then, the I_2 methanolic solution was decanted and replaced with a volume of fresh methanol. This process was repeated until the crystal samples recovered their original light-yellow color and the methanol became colorless. Other solvents including KI aqueous solution, DMSO, KI methanolic solution, and $Na_2S_2O_3$ aqueous solutions have also been used for effective I_2 desorption.

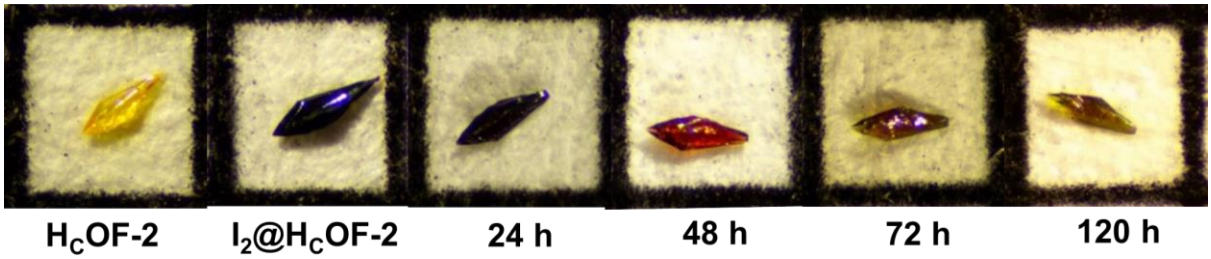

Figure S74. Images of a selected crystal of H_COF-2 (*left*), after I_2 adsorption (*second left*), and I_2 desorption process after immersing in methanol at different times (*left* to *right*). The crystal was placed on paper with 1 × 1 mm box for size comparison.

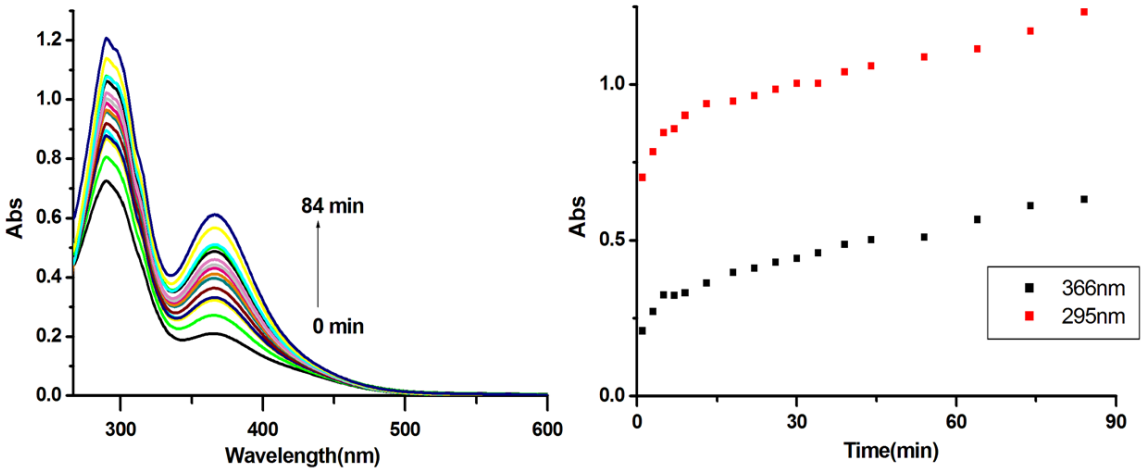

Figure S75. Time-dependent UV-Vis spectra of the I_2 desorbed from I_2⊂H_COF-2 in DMSO. Right: absorbance of the solution at 366 nm in DMSO.

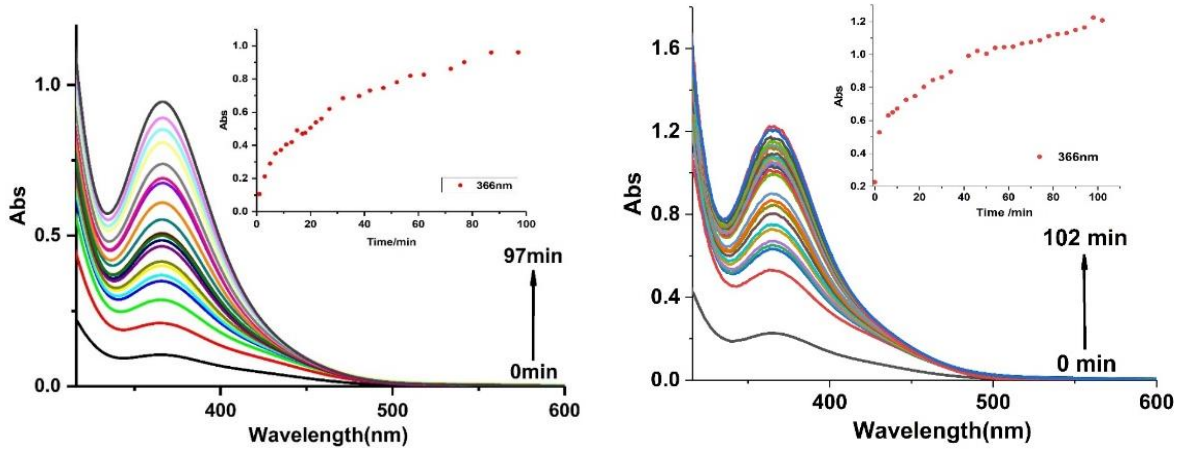

Figure S76. Time-dependent UV-Vis spectra of the I_2 desorbed from I_2⊂H_COF-3 (*left*) and I_2⊂H_COF-4 (*right*) in DMSO. Insert: absorbance of the solution at 366 nm in DMSO.

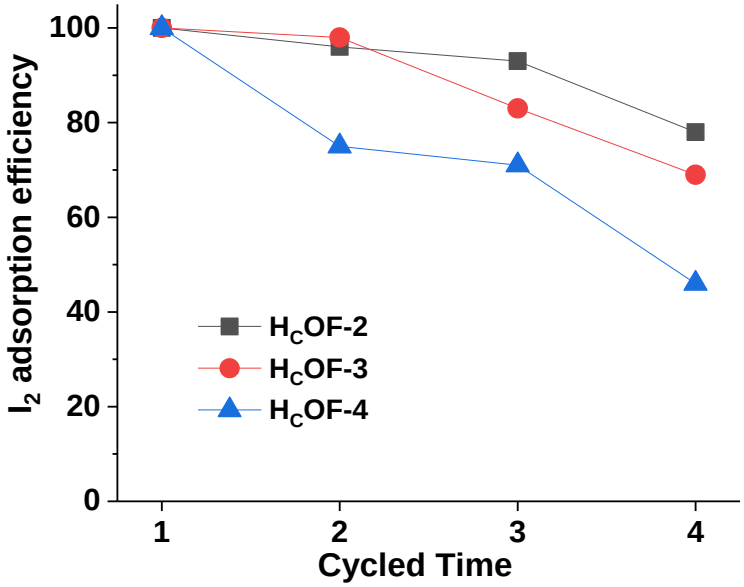

Figure S77. Cycled I_2 adsorption efficiency using H_COFs-2-4 performed in KI/I_2 aqueous solution (1.7 g KI and 2.2 g I_2 in 10 mL H_2O). I_2⊂H_COFs-2-4 in cycle 1 were marked as 100% efficiency.

S8. Computational and NMR investigations of the binding behavior between the model compounds 4 and 5 and iodine

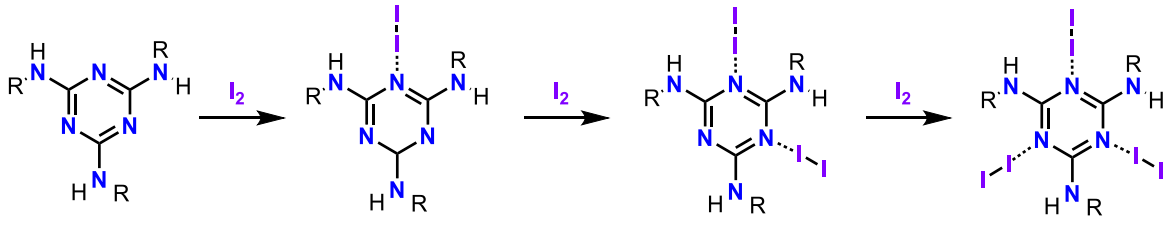

		ΔH_1 (kcal/mol)	ΔH_2 (kcal/mol)	ΔH_3 (kcal/mol)
4	R = -$(CH_2)_3$-S-CH_2CH_3	-12.5	-11.1	-12.1
5	-CH_2CH_3	-11.7	-12.0	-10.1

Scheme S9. DFT calculations of the stepwise iodine binding events with model compounds **4** and **5** were done using the B3LYP functional with the Grimme D3 dispersion correction, and the LACV3P**$^{++}$ basis set, as implemented in the Jaguar suite of programs. The bonding enthalpy (ΔH) listed here refers to each N—I interaction.

The iodine molecules do not bind in the plane of the substituted triazene ring. There is a very soft energy surface for bonding in the plane or out, so the non-planar binding is probably due to steric effects. The I—I distance in free iodine (calculated using the same method and basis set) is 2.869 Å. Binding

increases the I—I distance, consistent with donation from N into the I—I σ* orbital (see below). The shorter the N—I distance, the longer the I—I distance; adding more I_2 molecules results in overall longer N—I and shorter I—I distances.

The detailed nature of the interaction between the **5** and I_2 molecules was evaluated using an Energy Decomposition Analysis (EDA) using the ADF program suite. EDA allows partitioning of the overall attractive interaction (E_{int}) between two (or more) fragments into attractive and repulsive components. The fragment wavefunctions are evaluated independently in the geometries present in the molecule, which may be different from those in the free fragment; this difference in energy between the fragment in its ground state and that in the complex is defined as E_{prep} and is positive. The energy of the two fragments consists of an overall (for neutral fragments) repulsive interaction E_{steric}, which is a combination of Pauli repulsion (E_{Pauli}) between valence electrons occupying overlapping regions of space and subject to the exclusion principle, attenuated by attractive electrostatic interactions (E_{estat}) between the charge distributions in the two fragments. Finally, relaxation of the wavefunction by allowing orbital mixing between fragments gives a net stabilization (E_{orb}) due to electron sharing from this overlap together with polarization of electrons in the resultant molecular orbitals; this is taken to reflect the covalent contribution to the overall bonding. An additional attractive interaction due to dispersive forces (E_{disp}) completes the partition components, so that: $E_{int} = E_{Pauli} + E_{estat} + E_{orb} + E_{disp}$ (= $E_{steric} + E_{orb} + E_{disp}$). The molecular orbital and EDA analysis is consistent with an s-hole picture of N—I bonding, with significant electrostatic, covalent, and dispersive components to the interaction.

Table S10. Energy Decomposition components of each N—I interaction of iodine/**5** complex in kcal/mol.

	E_{Pauli}	E_{Estat}	E_{orb}	E_{Disp}	E_{int}
5 + $1I_2$	36.2	-25.8	-19.9	-5.2	-14.6
5 + $2I_2$	64.5	-46.7	-34.0	-11.9	-28.1
5 + $3I_2$	79.2	-58.2	-41.0	-17.1	-37.1

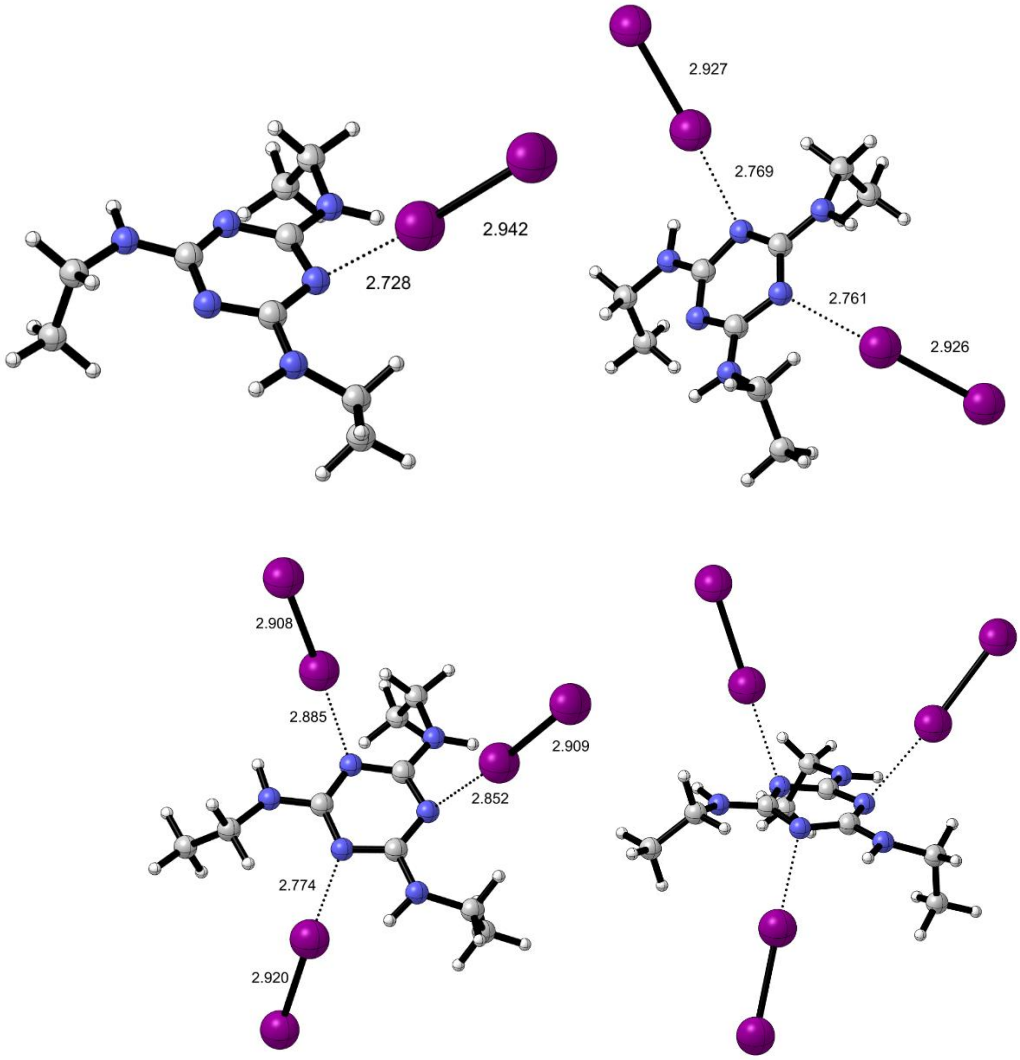

Figure S78. Calculated structures of mono-, di-, and tri-iodine adducts of **5** (distances are in Å).

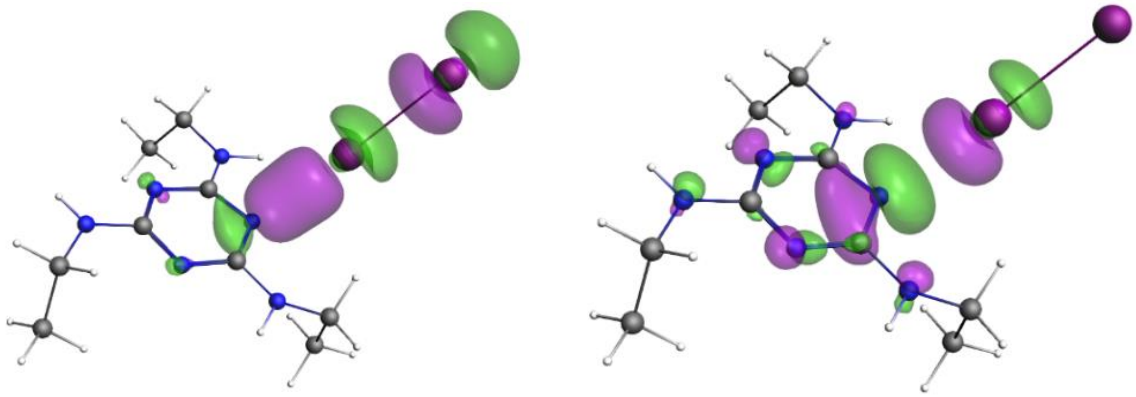

Figure S79. Calculated N—I bonding and antibonding orbitals of an iodine/**5** complex.

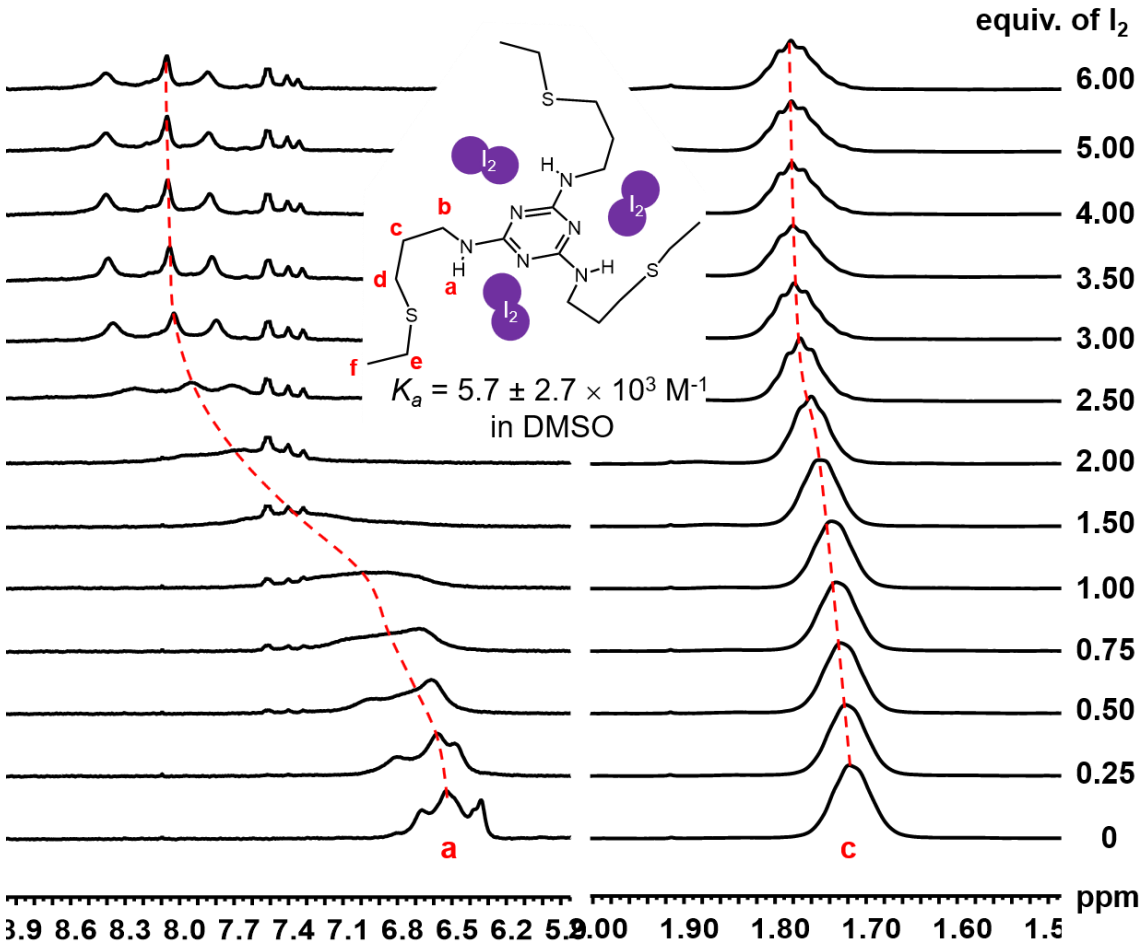

Figure S80. ^{1}H NMR spectra (500 MHz, DMSO-d_6) of compound **4** (3.70 mM, 0.5 mL DMSO-d_6) titrated with a DMSO-d_6 solution of iodine (0.326 M). From bottom to top: **4** only, **4** + 6.0 equivalents of iodine.

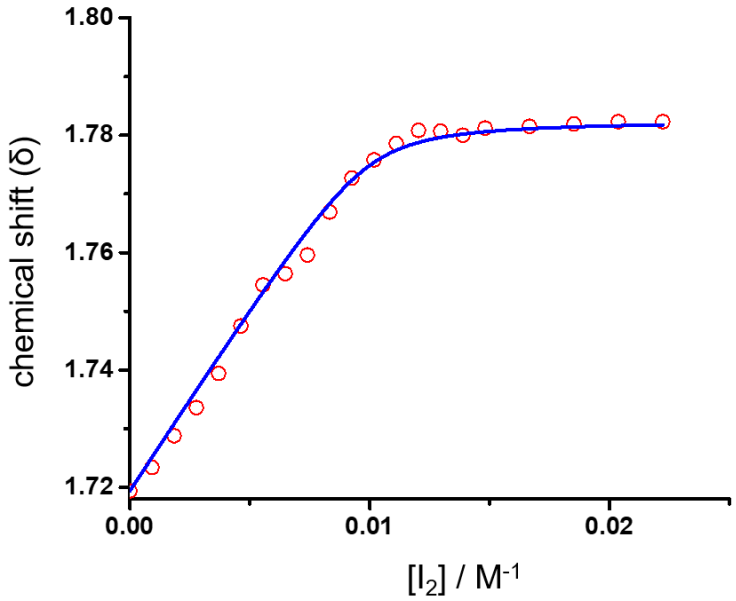

Figure S81. Experimental (red) and calculated (blue) chemical shift of proton resonance H_c in the ^{1}H NMR titration above.

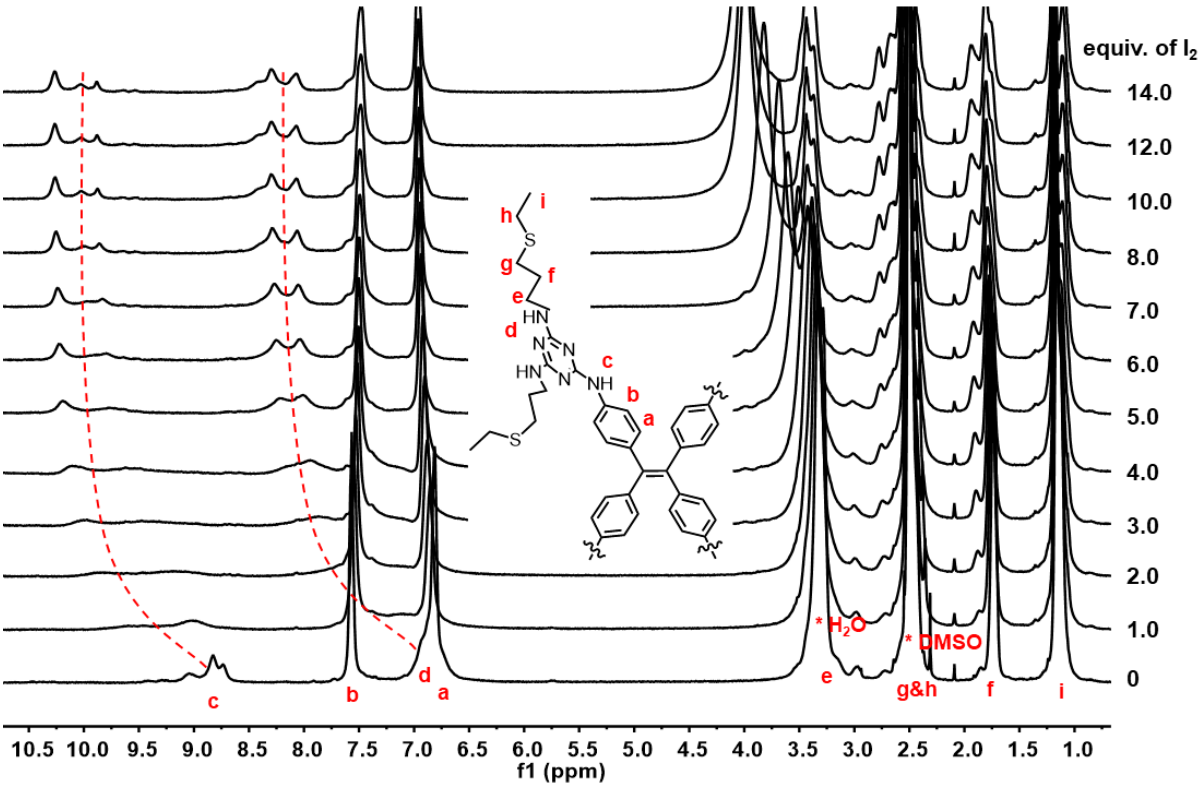

Figure S82. ^{1}H NMR spectra (500 MHz, DMSO-d_6) of compound **3** (6.53 mM, 0.5 mL DMSO-d_6) titrated with a DMSO-d_6 solution of iodine (0.326 M). From bottom to top: **3** only, **3** + 14.0 equivalents of iodine.

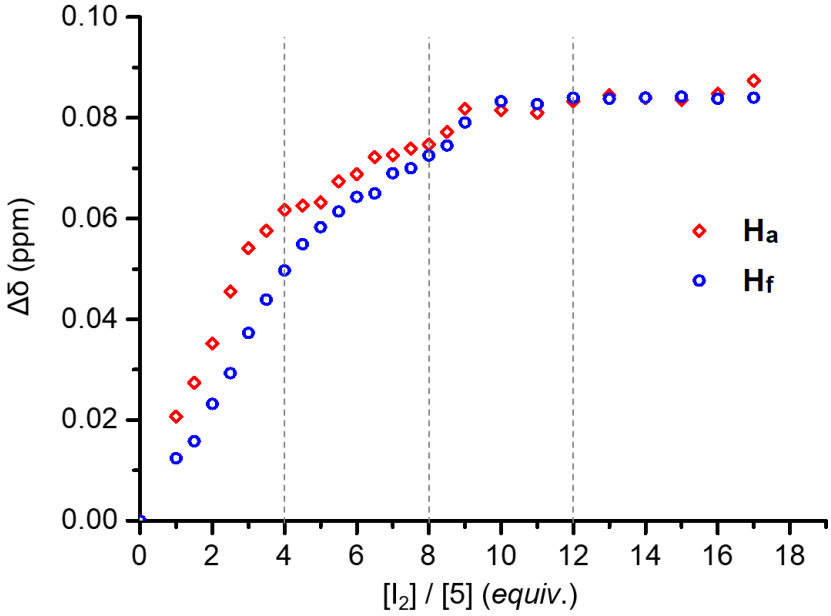

Figure S83. Chemical shifts of proton resonances H_a and H_f upon the addition of I_2 in the ^{1}H NMR titration above.

S9. Crystal size expansion in DMSO

Similar to the iodine adsorption-induced crystal size expansion, the crystal samples of H_COFs-2-4 expand upon soaking in hot DMSO over a period of time. Typically, a high-quality crystal was picked and soaked in DMSO (3 mL) and heated to a desired temperature for 24-72 h to monitor the macroscopic size expansion.

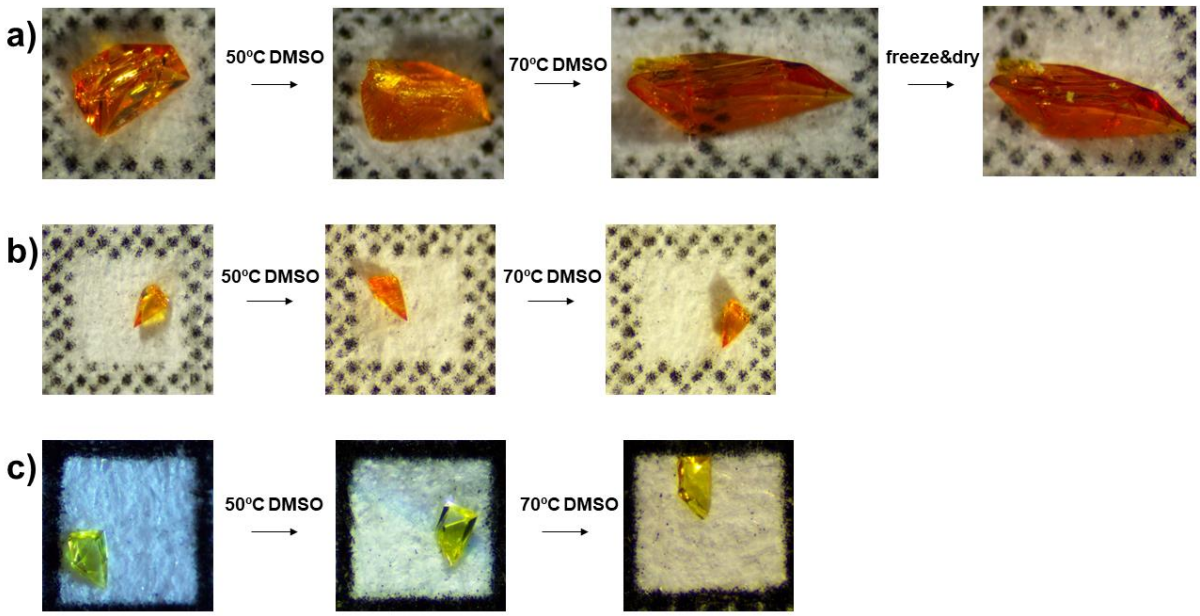

Figure S84. Visible elastic size expansion of crystal sample of (a) H_COF-2, (b) H_COF-3, and (c) H_COF-4 upon soaking in DMSO at different temperatures.

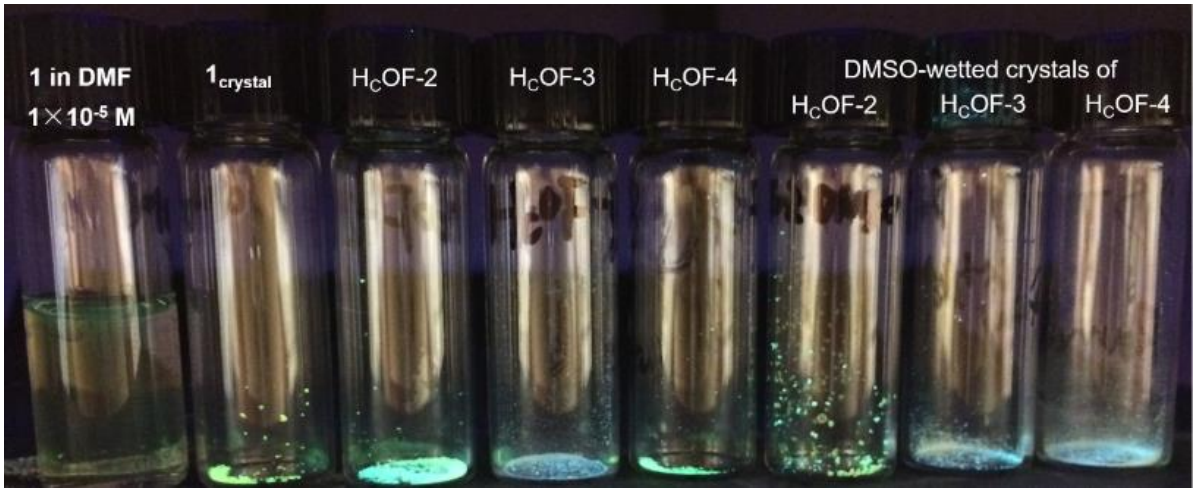

Figure S85. Photo images (*from left to right*) of a DMF solution of **1** (1×10^{-5} M^{-1}), activated crystal samples of $\mathbf{1}_{crystal}$, H_COF-2, H_COF-3, H_COF-4 and DMSO-wetted crystal samples of H_COF-2, H_COF-3, H_COF-4 recorded under the UV light (λ = 365 nm), respectively.

S10. Powder X-ray diffraction (PXRD) investigations

PXRD measurements were performed to study the crystallinity of H_COFs. Crystal samples of monomers $\mathbf{1}_{crystal}$ and $\mathbf{2}_{crystal}$, and H_COFs-2-4 were washed with MeCN before measurement. The data was collected with 0.02 deg step and 2 deg/min scan speed. The crystal samples of **P5-8** were also measured under same conditions.

In order to control the amount of the I_2 adsorbed in H_COFs for PXRD measurements, a 10 mg crystal sample of the selected H_COF was soaked in 2 mL methanolic I_2 solution (5 mg/mL) until the measured I_2 uptake reached 0.2 g/g. Next, the samples were immersed in a 3mL aqueous KI_3 solution (0.66 g I_2 and 0.54 g KI) to reach the maximum I_2 adsorption. The I_2 saturated H_COF crystal samples were washed with an excess of methanol and air-dried for PXRD experiments.

The elastic expansion of H_COFs in DMSO was investigated by PXRD. Firstly, the PXRD of the selected H_COF crystal sample was measured at ambient temperature. Then, it was soaked in DMSO and heated to 50 or 70 °C for 24 -72 h. The crystal sample was collected by filtration and the DMSO-wetted sample was directly subjected to X-ray irradiation. After being stored in the open air for 24 h, PXRD data was collected again.

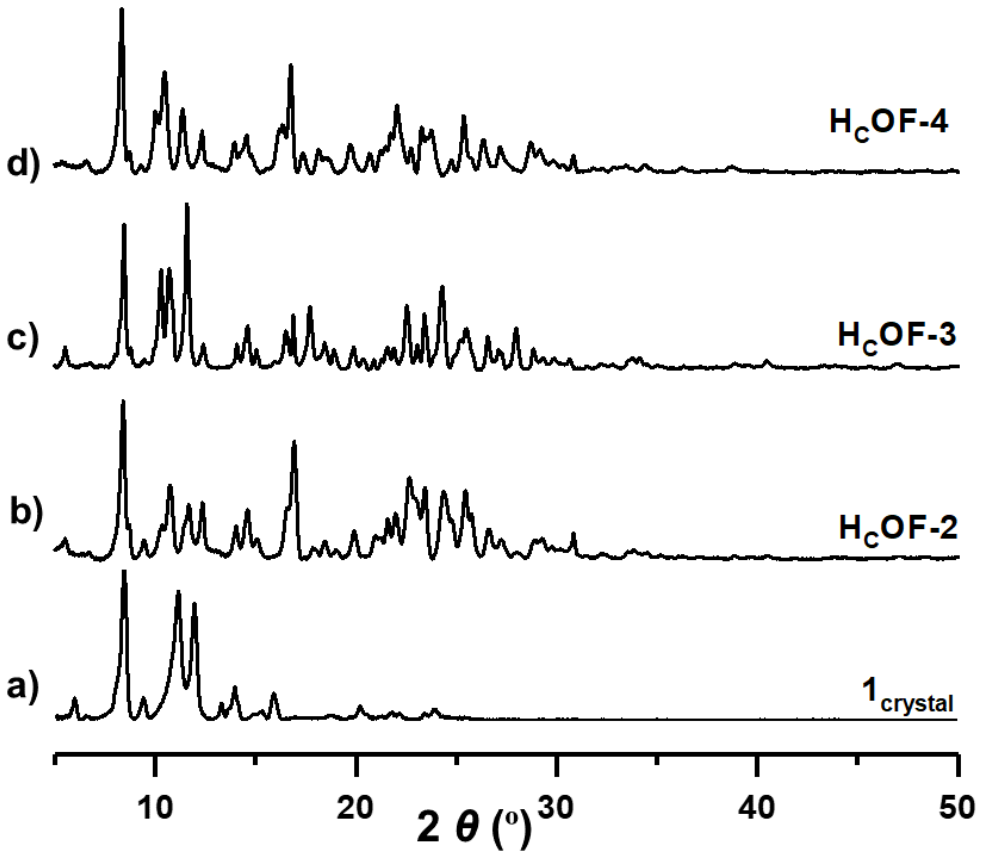

Figure S86. PXRD of profiles of (a) $\mathbf{1}_{crystal}$, (b) H_COF-2, (c) H_COF-3, and (d) H_COF-4, respectively.

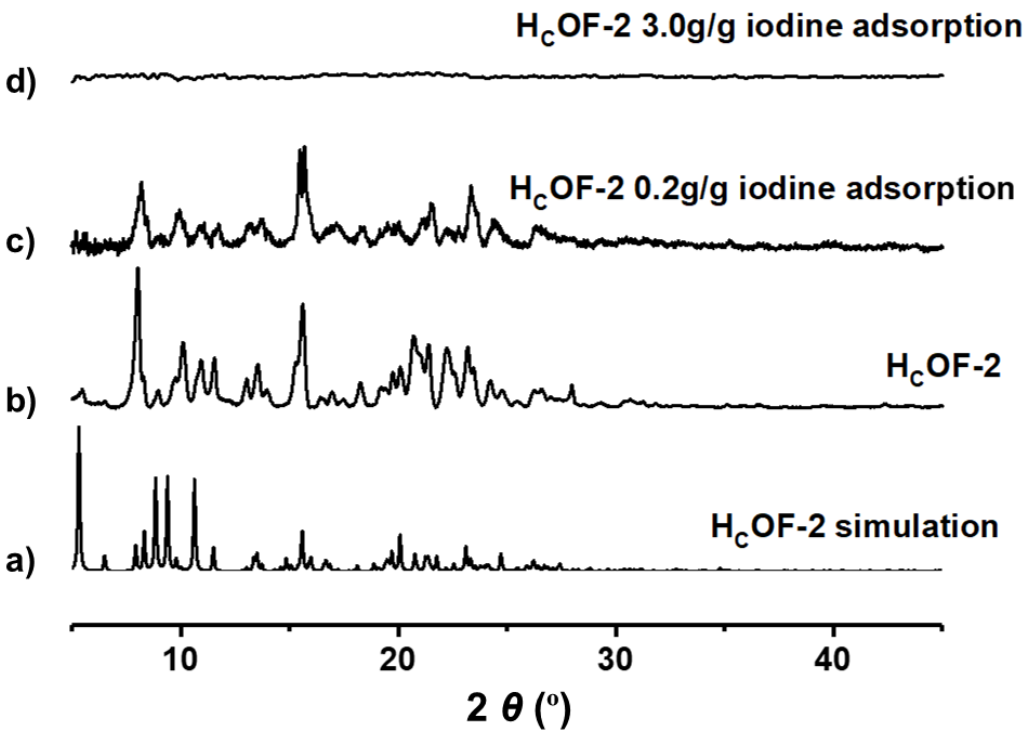

Figure S87. PXRD profiles of (a) simulated data of H_COF-2, (b) experimental data of H_COF-2, and (c-d) I_2⊂H_COF-2 crystal samples with different I_2 adsorption amount.

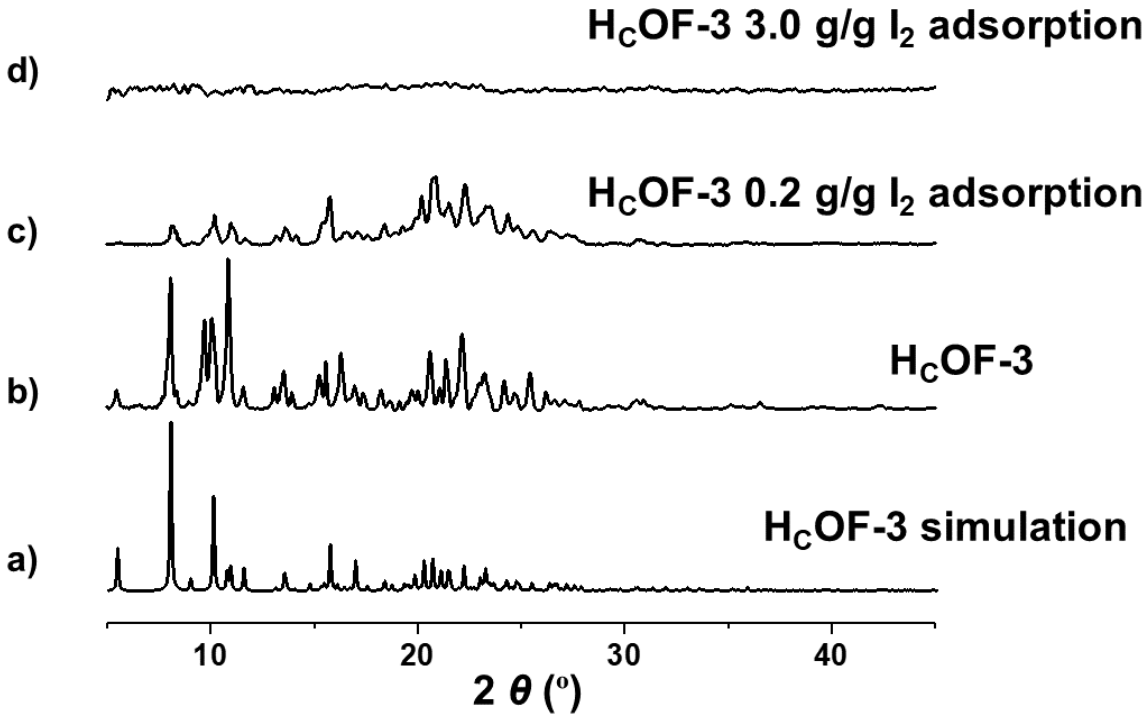

Figure S88. Powder X-ray diffraction profiles of (a) simulated data of H_COF-3, (b) experimental data of H_COF-3, (c-d) I_2⊂HCOF-3 crystal samples with different I_2 adsorption amount.

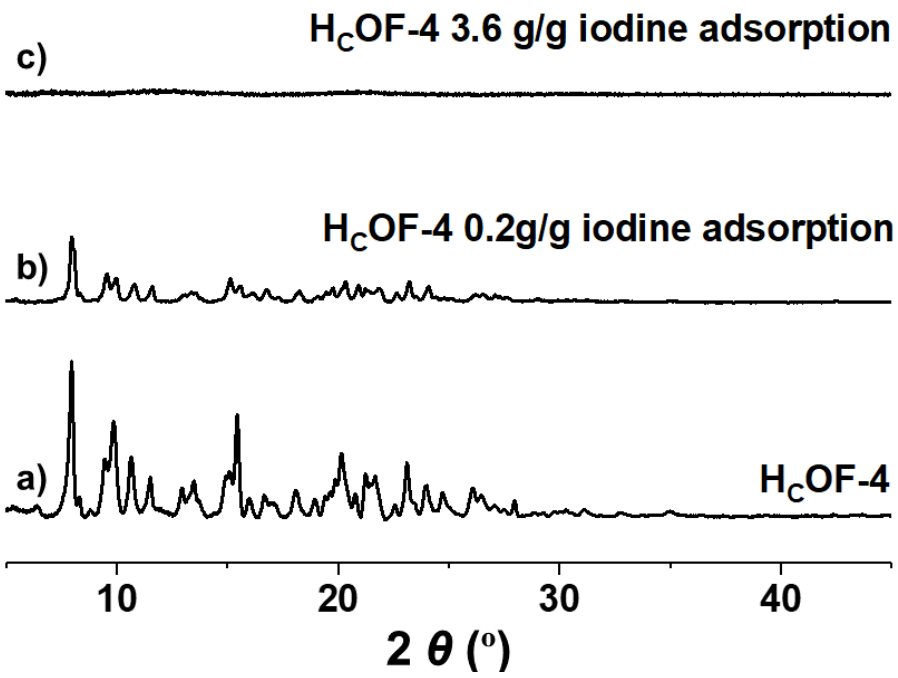

Figure S89. PXRD profiles of (a) H_COF-4, and (b-c) I_2⊂HCOF-4 crystal samples with different I_2 adsorption amount.

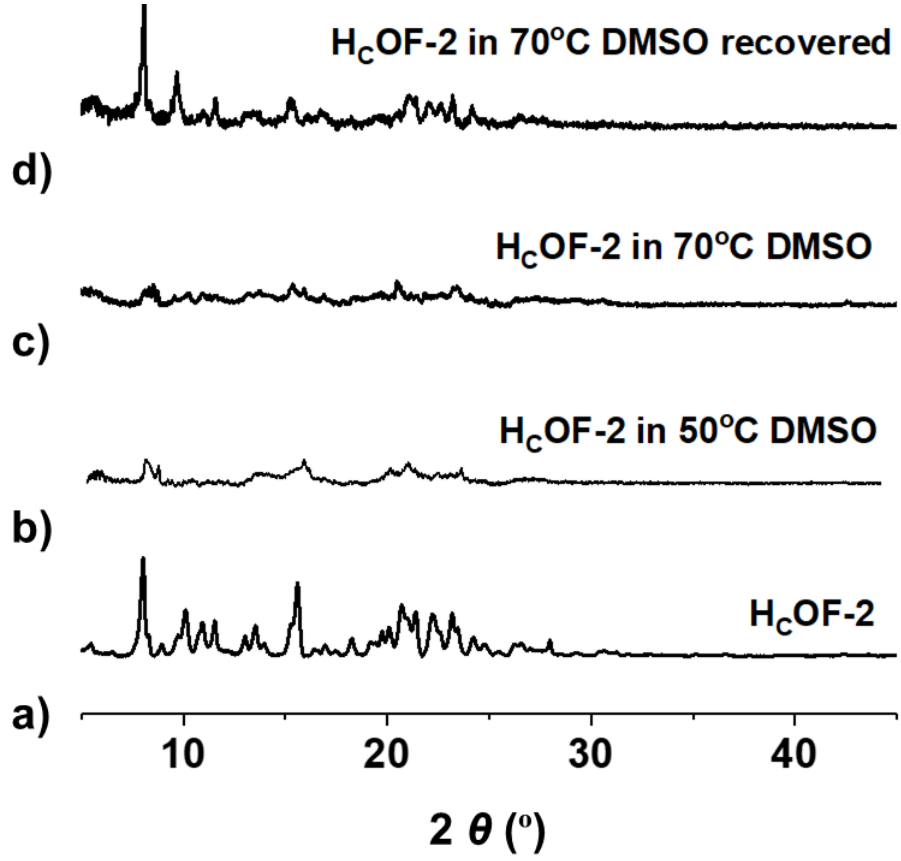

Figure S90. PXRD profiles of (a) pristine crystals of H_COF-2; (b) sample (a) directly subjected to data collection after being soaked in hot DMSO (50 °C, 24 h); (c) sample (a) directly subjected to data collection after being soaked in hot DMSO (70 °C, 48 h); (d) sample after treatment (c) kept in the open air for 72 h. All data were collected at room temperature with 2 deg/min scan speed.

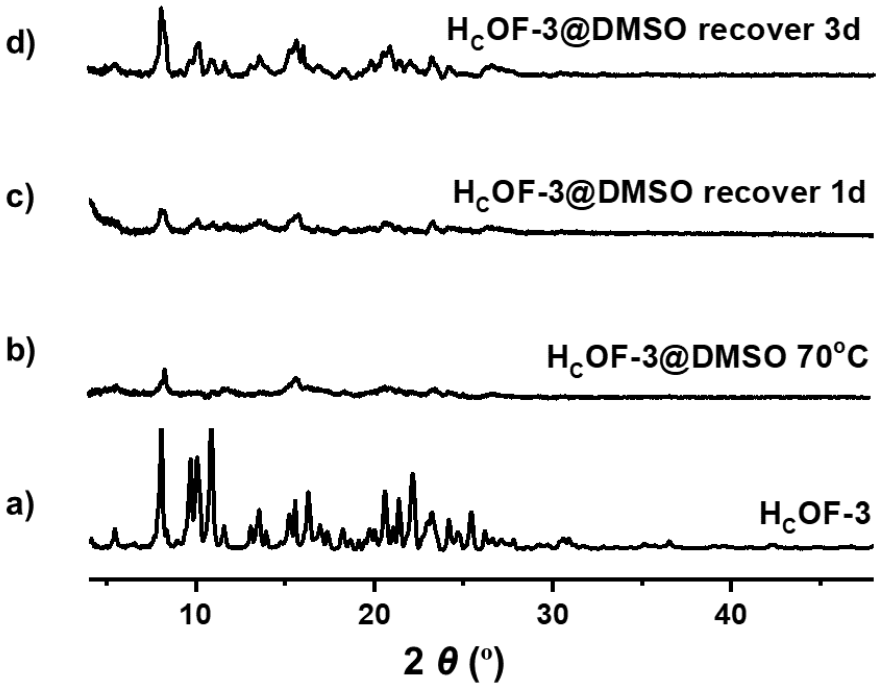

Figure S91. PXRD X-ray diffraction profiles of (a) pristine crystals of H_COF-3; (b) sample (a) directly subjected to data collection after being soaked in hot DMSO (70 °C, 72 h), (c-d) same sample after being (b) kept in the open air for 1 d (c) and 3 d (d). All data were collected at room temperature with 2 deg/min scan speed.

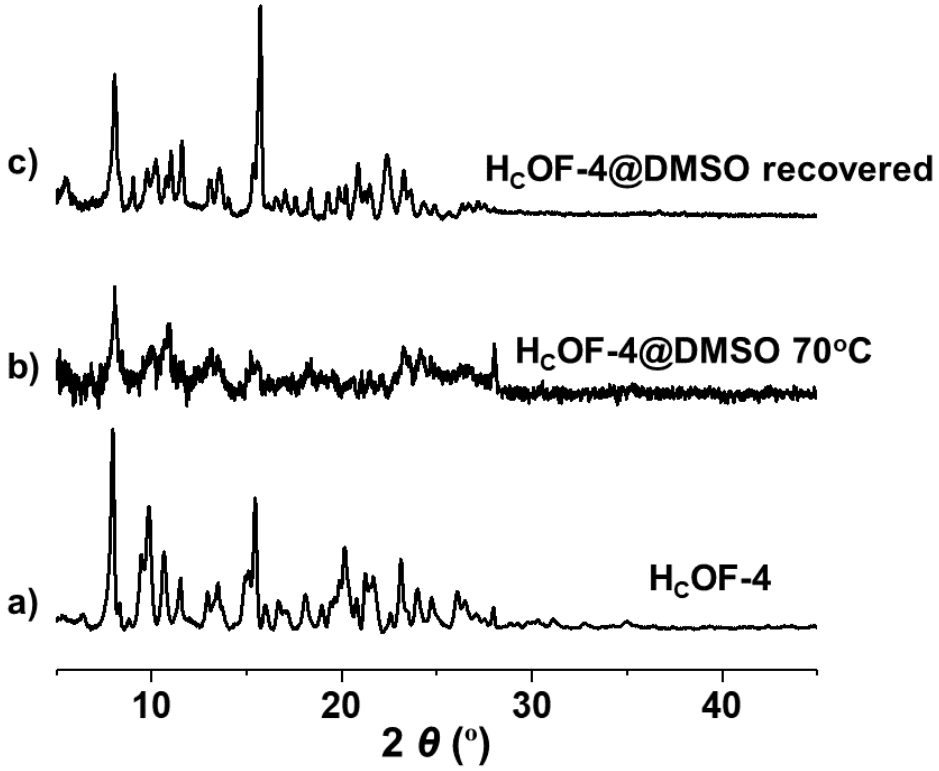

Figure S92. PXRD profiles of (a) pristine crystals of H_COF-4, (b) sample (a) directly subjected to data collection after being soaked in hot DMSO (70 °C, 48 h), (c) same sample after treatment (b) kept in the open air for 72 h. All data were collected at room temperature with 2 deg/min scan speed.

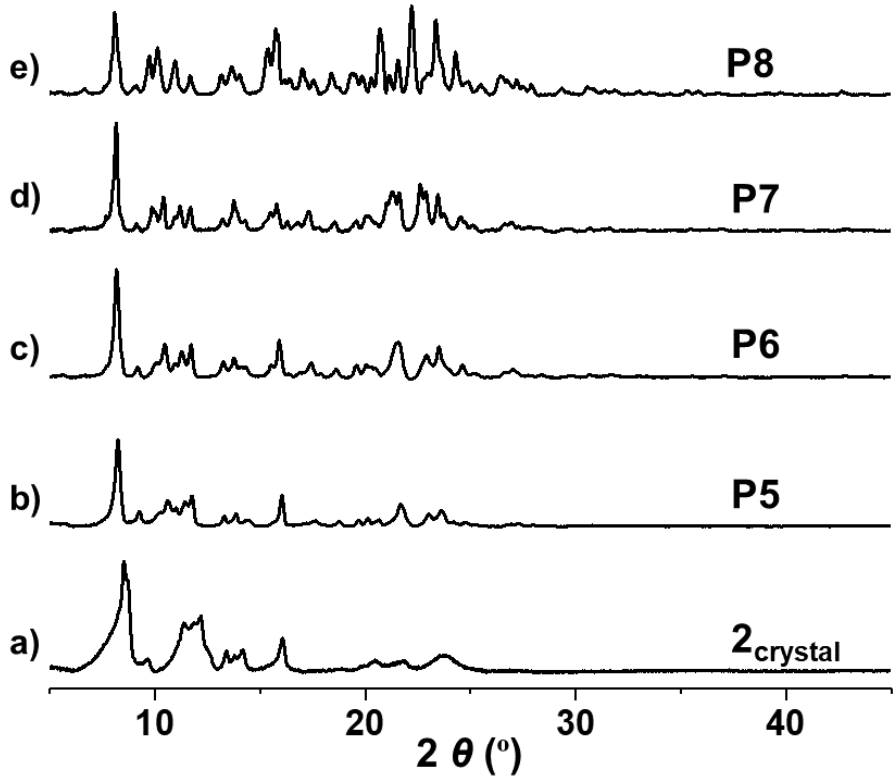

Figure S93. PXRD profiles of (a) $\mathbf{2}_{crystal}$, (b) **P5**, (c) **P6**, (d) **P7** and (e) **P8**, respectively

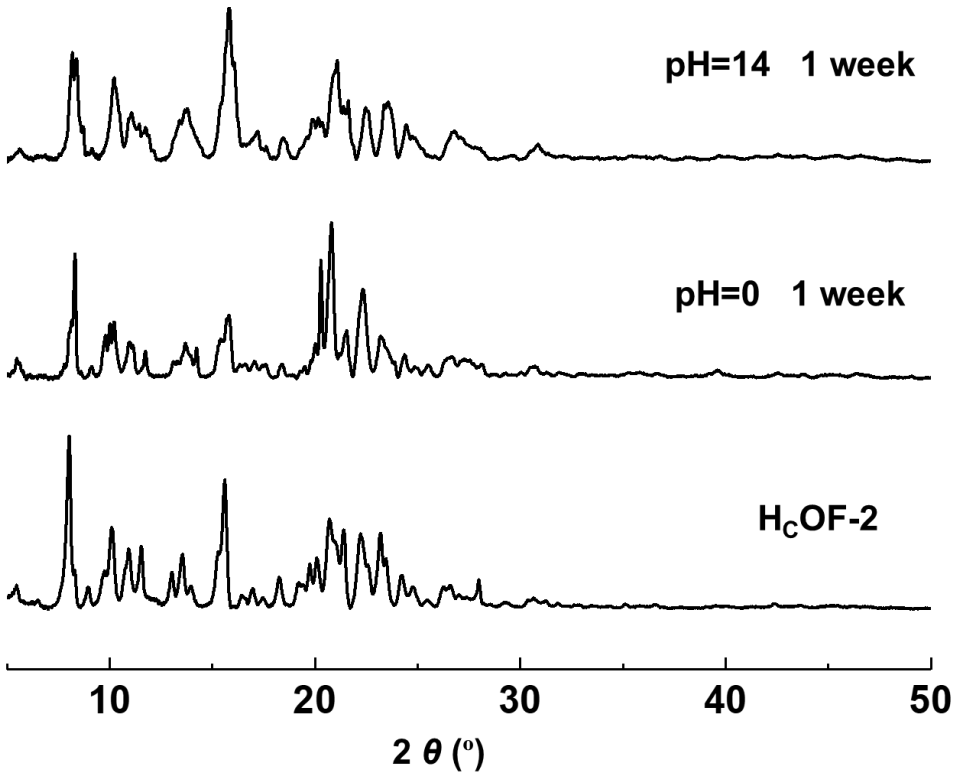

Figure S94. PXRD profiles of H_COF-2 after being soaked in pH = 14 and pH = 0 aqueous solutions for 1 week.

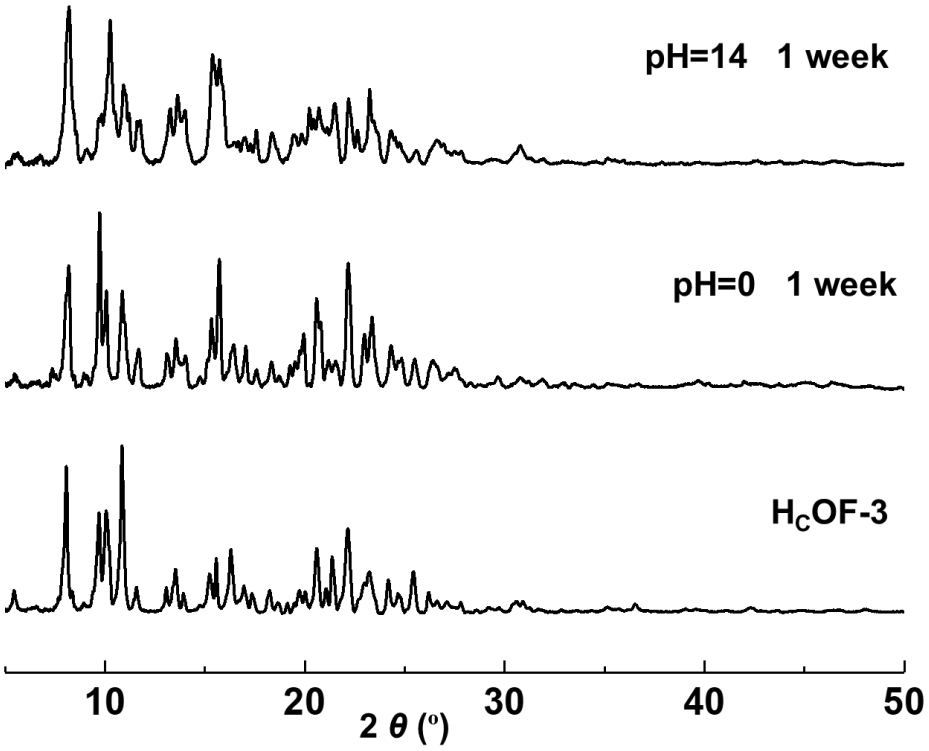

Figure S95. PXRD profiles of H_COF-3 after being soaked in pH = 14 and pH = 0 aqueous solutions for 1 week.

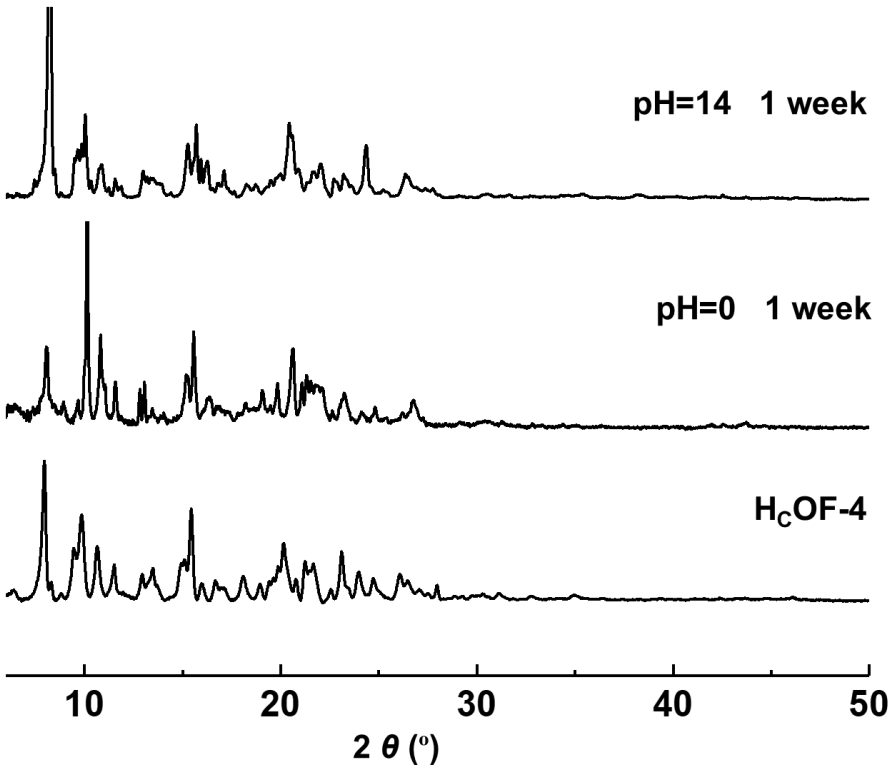

Figure S96. PXRD profiles of H_COF-4 after being soaked in pH = 14 and pH = 0 aqueous solutions for 1 week.

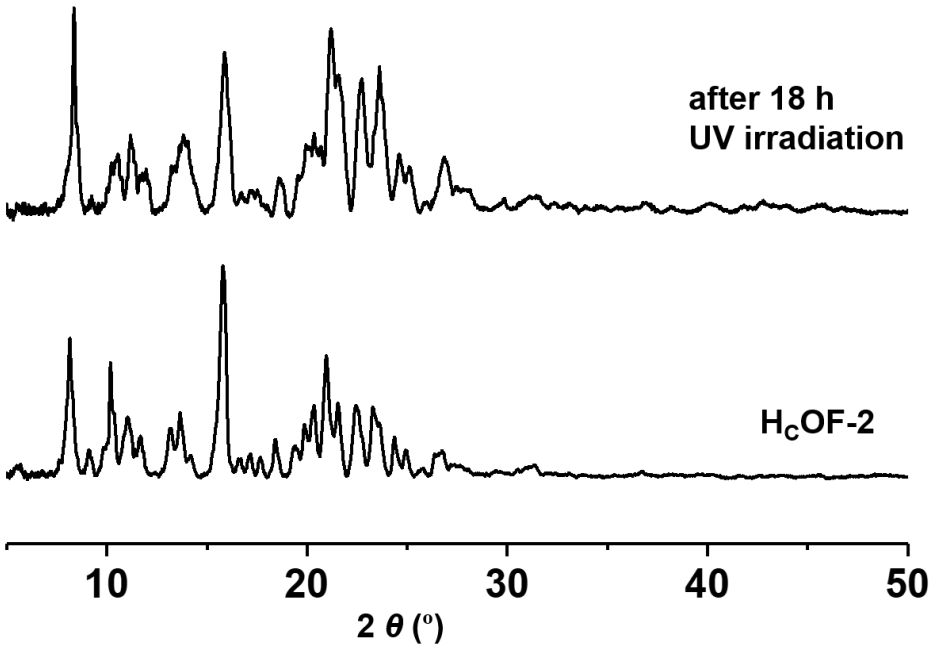

Figure S97. PXRD profiles of activated H_COF-2 crystals before and after exposing to UV irradiation for 18 h (λ = 365 nm, working distance of 82 mm) using a wavelength-controlled UV irradiation system. The irradiation spot diameter is 15 mm with an output light intensity of ~260 mW/cm^2.

S11. Porosity Measurements

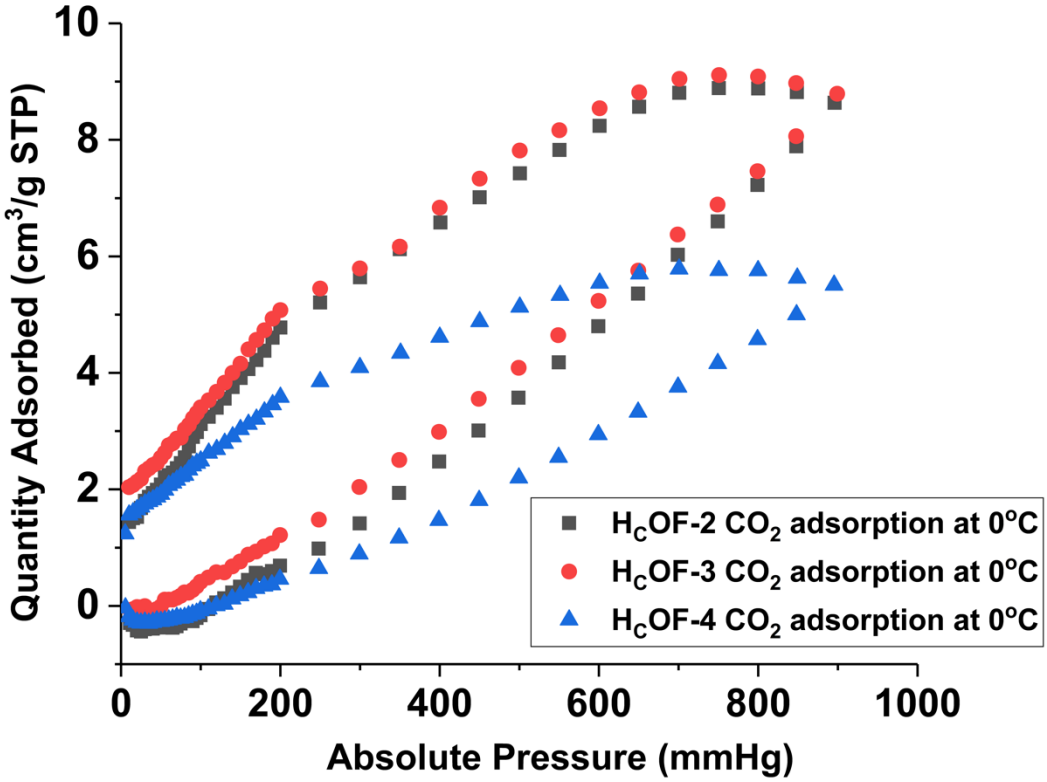

Figure S98. CO_2 sorption isotherms of H_COF-2 (black), H_COF-3 (red), and H_COF-4 (blue) recorded at 273 K.

Table S11. Summary of the iodine adsorption capacity, releasing efficiency and recyclability of porous materials. n. r. stands for not reported.

	Material name	Temp (°C)	Solvent or I_2 vapor	Capacity (g/g)	Release solvent	Release efficiency	Recyclability	Reference
Zeolites	Ca-zeolite A	25	I_2 vapor	0.04	water	4.9%	n. r.	*ACS Appl. Mater. Interfaces*, **2009**, *1*, 1579
	Ag^+-MOR	75	I_2 vapor	0.16	n. r.	n. r.	n. r.	*Ind. Eng. Chem. Res.* **2017**, *56*, 2331
Activated charcoals	AC1, AC2	75	I_2 vapor	1.05-1.17	n. r.	n. r.	n. r.	*Ind. Eng. Chem. Res.* **2017**, *56*, 2331
Ionic liquids	DESs	25	cyclohexane	0.48-0.99	n. r.	n. r.	n. r.	*Green Chem.*, **2016**, *18*, 2522
	[Bmim][Br]	25	cyclohexane	2.1	n. r.	n. r.	n. r.	*Phys. Chem. Chem. Phys.*, **2014**, *16*, 5071
Silver-based Adsorbents	AC-6120-silver impregnated silica gel	130	I_2 vapor	0.135	n. r.	n. r.	n. r.	*Methods of Gas Phase Capture of Iodine from Fuel Reprocessing Off-Gas: A Literature Survey*, INL/EXT-07-12299, Idaho National Laboratory: Idaho Falls, ID, 2007.
	AgA-silver impregnated alumina	150	I_2 vapor	0.10-0.24	n. r.	n. r.	n. r.	
	AgZ-silver exchanged mordenite	150	I_2 vapor	0.17	n. r.	n. r.	n. r.	
Resins	Amberlite XAD series	<50	I_2 vapor	0.2-1.0	n. r.	n. r.	n. r.	
MOFs	MIL series, CAU-1	25	cyclohexane	up to 0.31	ethanol	40%-70%	n. r.	*Chem. Commun.*, **2013**, *49*, 10320
	$Zn_9(btc)_4(atz)_{12}$	25	cyclohexane	0.40	ethanol	n. r.	n. r.	*Inorg. Chem.* **2016**, *55*, 13035

	Complex 1′	25	cyclohexane	1.01	ethanol	100%	n. r.	*J. Am. Chem. Soc.* **2010**, *132*, 2561
	CdL_2	25	cyclohexane / I_2 vapor	0.18 / 0.46	ethanol	98%	n. r.	*Chem. Commun.*, **2011**, *47*, 7185
	MFM-300(Sc)	80	I_2 vapor	1.54			n. r.	*J. Am. Chem. Soc.* **2017**, *139*, 16289
	$\{[(ZnI_2)_3(TPT)_2]\cdot 5.5(C_6H_5NO_2)\}_n$	25	I_2 vapor	1.73	irreversible capture		no	*Chem. Sci.*, **2017**, *8*, 3171
	ZIF-8	70	I_2 vapor	1.87 ± 0.18 g	laser light irradiation	87%	6 cycles	*Cryst. Growth Des.* **2018**, *18*, 356
		25	aqueous	1.31 ± 0.02 g	ethanol	70%	6 cycles	
	Zr–stilbene MOF	25	I_2 vapor	2.79	Physi- and chemisorption		n. r.	*Chem. Eur. J.* **2016**, *22*, 4870
	Cu-BTC	75	I_2 vapor	1.75	n. r.	n. r.	n. r.	*Chem. Mater.* **2013**, *25*, 2591
	$[Zn_2(tptc)(apy)_{2-x}(H_2O)_x]\cdot H_2O$	75	I_2 vapor	2.16	ethanol	n. r.	n. r.	*Inorg. Chem.* **2016**, *55*, 9270
	ZIF-8	77	I_2 vapor	1.25	n. r.	n. r.	n. r.	*J. Am. Chem. Soc.* **2011**, *133*, 12398
	$\{[Cu_6(pybz)_8(OH)_2]I^{5-}I^{7-}\}_n$		Co-crystallization	0.76	methanol	n. r.	n. r.	*J. Am. Chem. Soc.* **2012**, *134*, 4857
Porous polymer	CC3	20	I_2 vapor	0.558	ethanol	n. r.	n. r.	*J. Am. Chem. Soc.* **2011**, *133*, 14920
	CMPN	70	I_2 vapor	0.97-2.08	ethanol	n. r.	n. r.	*J. Mater. Chem. A*, **2015**, *3*, 87
	PAF-23-25	75	I_2 vapor	up to 2.76	ethanol	n. r.	n. r.	*Angew. Chem. Int. Ed.* **2015**, *54*, 2733

	BDP-CPP-1	75	I_2 vapor	2.83			n. r.	*J. Mater. Chem. A,* **2017**, *5*, 6622
	NiP-CMP	77	I_2 vapor	2.02	ethanol	96%	5 cycles	*Chem. Commun.*, **2014**, *50*, 8495
	Azo-Trip	77	I_2 vapor	2.33	ethanol	96.4%	n. r.	*Polym. Chem.*, **2016**, *7*, 643
	AzoPPN	77	I_2 vapor	2.90	hexane	~99%	n. r.	*Chem. Eur. J.* **2016**, *22*, 11863.
	SCMP-I and SCMP-II	80	I_2 vapor cyclohexane	3.45/ 3.24	Physi- and chemisorption		n. r.	*Chem. Commun.*, **2016**, *52*, 9797
					hexane	~ 60%		
	HCMPs	85	I_2 vapor	3.16	heating	98.8%	3 cycles	*Macromolecules*, **2016**, *49*, 6322
	Pillar[6]arene Crystal	85	I_2 vapor	0.26	chloroform	98%	5 cycles	*J. Am. Chem. Soc.* **2017**, *139*, 15320.
		25	hexane	0.26	cyclohexane	98%	5 cycles	
	TTPB	77	I_2 vapor	4.43	heating	86.79%	5 cycles	*J. Mater. Chem. A,* 2017, **5**, 7612–7617
	PSIF-1a	75	I_2 vapor	4.85	heating	80%	n. r.	*DOI:10.1021/acsami.8b03023*
Covalent organic frameworks	SIOC-COF-7	75	I_2 vapor	4.81	heating	96%	5 cycles	*Chem. Commun.*, **2017**, *53*, 7266.
	COF-DL229	75	I_2 vapor	4.7	methanol	80%	4 cycles	*Chem.Eur.J.* **2018**, *24*,585.
	TPT-DHBD$_x$ COF	75	I_2 vapor	5.43	heating	80%	3 cycles	*Chem. Mater.* 2018, **30**, 2299−2308
	TPB-DMTP and TTA-TTB	77	I_2 vapor	6.26 / 4.95	methanol	97% / 95%	5 cycles	*Adv. Mater.* 2018, 1801991

References

[1] Lin, Y.; Jiang, X.; Kim, S. T.; Alahakoon, S. B.; Hou, X.; Zhang, Z.; Thompson, C. M.; Smaldone, R. A.; Ke, C. An Elastic Hydrogen-Bonded Cross-Linked Organic Framework for Effective Iodine Capture in Water. *J. Am. Chem. Soc.* **2017**, *139*, 7172−7175.

[2] Dhainaut, A.; Regnier, G.; Atassi, G.; Pierre, A.; Leonce, S.; Kraus-Berthier, L.; Prost, J. F. New Triazine Derivatives as Potent Modulators of Multidrug Resistance. *J. Med. Chem.* **1992**, *35*, 2481-2496.

[3] Sheldrick, G. M. SHELXT-Integrated Space-Group and Crystal-Structure Determination. *Acta Cryst. A* **2015**, *A71*, 3-8.

[4] Sheldrick, G. M. Crystal Structure Refinement with SHELXL. *Acta Cryst. C* **2015**, *C71*, 3-8.

[5] Spek, A. L. Structure Validation in Chemical Crystallography. *Acta Cryst. D* **2009**, *D65*, 148-155.

[6] Blatov, V. A.; Shevchenko, A. P.; Proserpio, D. M. Applied Topological Analysis of Crystal Structures with the Program Package ToposPro. *Cryst. Growth Des*. **2014**, *14*, 3576−3586.

[7] Baburin, I. A.; Blatov, V. A.; Carlucci, L.; Ciani, G.; Proserpio, D. M. Interpenetrated Three-Dimensional Networks of Hydrogen-Bonded Organic Species: A Systematic Analysis of the Cambridge Structural Database. *Cryst. Growth Des.* **2008**, *8*, 519-539.

[8] Soares, S. M.; Lemos, S. S.; Sales, M. J. A.; Back, D. F.; Lang, E. S. Synthesis and Structural Characterization of Cadmium(II) Complexes with Chelating Keto-Hydroxy Compounds: The X-ray Molecular Structure of $[Cd_2(nq)_4(H_2O)_4]\cdot 3H_2O$ (nqH = 2-hydroxynaphthoquinone). *Polyhedron* **2009**, *28*, 3811-3815; He, C.; Shreeve, J. M. Energetic Materials with Promising Properties: Synthesis and Characterization of 4,4′-Bis(5-nitro-1,2,3-2H-triazole) Derivatives. *Angew. Chem. Int. Ed*. **2015**, *54*, 6260-6264; Schoedel, A.; Wojtas, L.; Kelley, S. P.; Rogers, R. D.; Eddaoudi, M.; Zaworotko, M. J. Network Diversity through Decoration of Trigonal-Prismatic Nodes: Two-Step Crystal Engineering of Cationic Metal–Organic Materials. *Angew. Chem. Int. Ed*. **2011**, *50*, 11421-11424.

[9] Alexandrov, E. V.; Shevchenko, A. P.; Blatov, V. A. Topological Databases: Why Do We Need Them for Design of Coordination Polymers? *Cryst. Growth Des.* **2019**, 19, 2604-2614.

[10] Blatov, V. A.; Golov, A. A.; Yang, C.; Zeng, Q.; Kabanov, A. A. Network Topological Model of Reconstructive Solid-State Transformations. *Sci. Rep*. **2019**, *9*, 6007.

[11] Liu, Y.; O'Keeffe, M.; Treacy, M. M. J.; Yaghi, O. M. The Geometry of Periodic Knots, Polycatenanes and Weaving from a Chemical Perspective: A Library for Reticular Chemistry. *Chem. Soc. Rev.* **2018**, *47*, 4642-4664.

[12] Zhang, J. P.; Qi, X. L.; He, C. T.; Wang, Y.; Chen, X. M. Interweaving Isomerism and Isomerization of Molecular Chains. *Chem. Commun*. **2011**, *47*, 4156–4158; Rajput, L.; Sarkar, M.; Biradha, K. Assembling One-Dimensional Coordination Polymers into Three-Dimensional Architectures via Hydrogen Bonds. *J. Chem. Sci.* **2010**, *122*, 707-720.

[13] Alexandrov, E. V.; Blatov, V. A.; Proserpio, D. M. A Topological Method for Classification of Entanglements in Crystal Networks. *Acta Cryst. A* **2012**, *68*, 484-493; Alexandrov, E. V.; Blatov, V. A.; Proserpio, D. M. How 2-Periodic Coordination Networks are Interweaved: Entanglement Isomerism and Polymorphism. *CrystEngComm* **2017**, *19*, 1993-2006.

[14] Koch, E.; Fischer, W. Types of Sphere Packings for Crystallographic Point Groups, Rod Groups and Layer Groups. *Zeitschr. Kristallogr.* **1978**, *148*, 107-152.

[15] Lo, Y. C.; Chang, Y. J.; Chhetri, P. M.; Huang, W. J.; Chen, J. D. Construction of Coordination Polymers Based on Bis-pyridyl-bis-amide and Dicarboxylate Ligands. *Polyhedron* **2016**, *117*, 777-787; Wu, T. T.; Hsu, W.; Yang, X. K.; He, H. Y.; Chen, J. D. Entanglement in Co(II) Coordination Networks: Polycatenation from

Single Net to 2-Fold and 3-Fold Interpenetrated Nets. *CrystEngComm* **2015**, *17*, 916 -924; Ji, C. C.; Qin, L.; Li, Y. Z.; Guo, Z. J.; Zheng, H. G. Effect of Different Imidazole Ancillary Ligands on Supramolecular Architectures of a Series of Zn(II) and Cd(II) Complexes with a Bent Dicarboxylate Ligand. *Cryst. Growth Des.* **2011**, *11*, 480-487; Liao, Y. H.; Hsu, W.; Yang, C. C.; Wu, C. Y.; Chen, J. D.; Wang, J. C. Structural Diversity of Ni(II) Coordination Polymers Containing Dipyridyl Amide and Angular Dicarboxylate Ligands: Synthesis, Structures and Magnetism. *CrystEngComm* **2013**, *15*, 3974-3983; Sie, M. J.; Chang, Y. J.; Cheng, P. W.; Kuo, P. T.; Yeh, C. W.; Cheng, C. F.; Chen, J. D.; Wang, J. C. Interpenetrated and Polycatenated Nets of Cd(II) Coordination Networks From Mixed N,N′-dipyridyladipoamide and Dicarboxylate Ligands. *CrystEngComm* **2012**, *14*, 5505-5516.